Scalable Ab Initio Quantum Many-Body Methods for Crystalline Materials

Thesis by
Junjie Yang

In Partial Fulfillment of the Requirements for the
Degree of
Doctor of Philosophy

CALIFORNIA INSTITUTE OF TECHNOLOGY
Pasadena, California

2026
Defended Feb 9, 2026

Junjie Yang
ORCID: 0000-0002-6726-6538

Acknowledgements

My foremost thanks go to my advisor, Prof. Garnet Chan, who has fundamentally shaped my identity as a scientist. Through his guidance, I have learned to think both critically and creatively while navigating the challenges of research with resilience and efficiency. Most importantly, he taught me that technical progress must always serve broader scientific goals. His consistent encouragement throughout my Ph.D. has been essential to my growth and has inspired me to explore diverse research directions.

I also thank Prof. Austin Minnich, Prof. Scott Cushing, and Prof. Sandeep Sharma for serving on my thesis committee and providing valuable guidance on my exams and dissertation. I remain grateful to my former advisors, Prof. Chungen Liu and Prof. Yihan Shao, for introducing me to the field of quantum chemistry and nurturing my early development as a researcher.

Beyond my advisors, I have been fortunate to learn from excellent mentors during my Ph.D. I am particularly grateful to Zhi-Hao Cui, with whom I collaborated on multiple projects. His guidance and expertise enabled me to navigate the most challenging aspects of my work. Huanchen Zhai, Chenghan Li, and Xing Zhang also provided invaluable mentorship on various projects and taught me essential practical research skills.

Equally important to my development were collaborations with many talented researchers. I thank Ankit Mahajan, Tim Berkelbach, Ke Liao, Henrik Lars-

son, Seunghoon Lee, Lin Lin, Linqing Peng, Gunhee Park, Ruojing Peng, Raehyun Kim, David Reichman, Chong Sun, Shunyue Yuan, Johannes Tölle, Shuoxue Li, Hong-Zhou Ye, Qiming Sun, Rui Li, and Tianyu Zhu. Their contributions proved essential to this work.

The research presented here has also benefited greatly from the open-source scientific computing ecosystem. I thank the developers and maintainers of NumPy, SciPy, JAX, and PyTorch for essential numerical infrastructure, and the communities surrounding PySCF, Block2, and LibDMET for valuable discussions, bug reports, and code contributions that have shaped these packages into reliable research tools.

The Caltech community has provided a welcoming home for my research. The Division of Chemistry and Chemical Engineering maintains a rich tradition in theoretical chemistry, and I am proud to have contributed to this legacy. The Resnick High Performance Computing Center at Caltech and the National Energy Research Scientific Computing Center have provided essential computational resources that made this work possible.

The Chan group has been a constant source of support and inspiration. Beyond my direct collaborators, I thank Matt O'Rourke, Johnnie Gray, Zuxin Jin, Wenyuan Liu, Yuhang Ai, Tomislav Begusic, Petra Shih, Verena Neufeld, Eirik Kjønstad, Jielun Chen, Sijing Du, Jiace Sun, Runze Chi, and all other group members for generously sharing their expertise. My roommates and friends, Yao Luo, Ruilin Qian, Ziyang Qin, Sihe Chen, and Qinghan Hou, have provided companionship and support that made my time at Caltech enjoyable.

Finally, I express my deepest love and gratitude to my parents and family. Their unconditional support gave me the freedom and courage to pursue my intellectual interests wherever they led.

Abstract

Achieving materials-specific predictions for large, realistic molecules and solids with strong electron correlations remains a long-standing challenge in quantum chemistry. This dissertation develops scalable ab initio quantum many-body methods for crystalline materials, demonstrating that rigorous optimization of theoretical approximations and numerical algorithms enables predictive computation even in strongly correlated systems. The work tackles three interconnected challenges, namely describing material-specific properties of strongly correlated superconductors, achieving linear scaling with k-points for large-scale periodic calculations, and establishing reliable methods for electron-phonon interactions. The following chapters address each challenge in turn.

Chapter 2 demonstrates that ab initio density matrix embedding theory, combined with symmetry-breaking strategies for superconducting order parameters, reproduces experimental trends in cuprate superconductivity, including pressure and layer effects on transition temperatures. By directly solving the electronic Schrödinger equation from material structures, these calculations capture multi-orbital covalency effects that simplified model Hamiltonians neglect, revealing their essential role in the spin fluctuations driving pairing. This predictive capability establishes a foundation for efficient computational screening of superconducting materials. Extending these calculations to larger k-point meshes and broader phase diagram explorations, however, demands

more efficient computational algorithms.

To overcome this computational bottleneck, Chapter 3 introduces interpolative separable density fitting framework. This development enables thermodynamic limit calculations with up to 1000 k-points, as validated on diamond, carbon dioxide, nickel monoxide, and cuprate systems. Integration with density matrix embedding theory and local natural orbital methods further yields converged ground-state energies from accurate correlated wavefunction methods such as CCSD(T) for crystalline materials in the thermodynamic limit. With computational efficiency established, the remaining challenge lies in extending the theoretical framework beyond purely electronic degrees of freedom.

Chapter 4 addresses this need by establishing exponential ansatz wavefunctions as competitive approaches for electron-phonon systems. Unlike previous treatments based on perturbation theory, systematic benchmarking of coupled cluster theory and variational Lang-Firsov methods on the Holstein model demonstrates, for the first time, that these approaches accurately describe polaron formation across coupling regimes when combined with appropriate reference state optimization. These results provide a foundation for incorporating phonon effects into ab initio studies of superconducting materials.

In addition to these methodological advances, GPU acceleration and MPI parallelization enhance computational throughput, enabling efficient large-scale calculations. Together, these developments constitute a computational framework for predictive ab initio quantum many-body calculations in crystalline materials, opening new avenues for understanding and designing strongly correlated quantum materials.

Published Content and Contributions

[1] **Yang, Junjie**, N. Zhang, S. Yuan, J. Yu, H.-Z. Ye, and G. Chan, "Ab Initio Many Body Quantum Embedding and Local Correlation in Crystalline Materials using Interpolative Separable Density Fitting", 10.48550/ARXIV.2601.16379 (2026),

JY participated in designing the study, performing the calculations, and writing of the manuscript. Pre-published.

[2] Z.-H. Cui, **Yang, Junjie**, J. Tölle, H.-Z. Ye, S. Yuan, H. Zhai, G. Park, R. Kim, X. Zhang, L. Lin, T. C. Berkelbach, and G. K.-L. Chan, "Ab initio quantum many-body description of superconducting trends in the cuprates", Nat Commun **16**, 1845 (2025),

JY participated in designing the study, performing the calculations, and writing of the manuscript.

[3] **Yang, Junjie**, Z.-H. Cui, A. Mahajan, H. Zhai, D. R. Reichman, and G. K.-L. Chan, "Benchmarking the exponential ansatz for the Holstein model", The Journal of Chemical Physics **161**, 104105 (2024),

JY participated in designing the study, performing the calculations, and writing of the manuscript.

[4] C. Li, **Yang, Junjie**, X. Zhang, and G. Kin-Lic Chan, "Multi-site reaction dynamics through multi-fragment density matrix embedding", The Journal of Chemical Physics **158**, 134105 (2023),

JY participated in designing the study and writing of the manuscript.

[5] H. Zhai, H. R. Larsson, S. Lee, Z.-H. Cui, T. Zhu, C. Sun, L. Peng, R. Peng, K. Liao, J. Tölle, **Yang, Junjie**, S. Li, and G. K.-L. Chan, "Block2 : A comprehensive open source framework to develop and apply state-of-the-art DMRG algorithms in electronic structure and be-

yond", The Journal of Chemical Physics **159**, 234801 (2023),

JY supported the software development and contributed to the method validation and the manuscript editing.

TABLE OF CONTENTS

LIST OF ILLUSTRATIONS

Number *Page*

LIST OF TABLES

Number *Page*

Chapter 1

Introduction

The accurate simulation of strongly correlated crystalline materials from first principles remains one of the grand challenges in quantum chemistry. While transistor density grew exponentially for decades, as captured by Moore's law [1], hardware advances alone cannot overcome the fundamental intractability of the quantum many-body problem. As transistor dimensions approach the nanometer scale, quantum tunneling induces substantial leakage currents, establishing physical limits on transistor scaling. Power dissipation constraints have imposed a ceiling on clock frequencies, and the widening disparity between processor throughput and memory bandwidth [2] has compelled a paradigm shift toward massive parallelism. Yet this strategy encounters its own barriers. Scaling beyond thousands of cores yields diminishing returns because the serial fraction of any algorithm bounds overall speedup [3], a limitation further compounded by communication overhead in distributed environments. The path forward, therefore, lies not only in exploiting modern hardware through GPU acceleration and efficient parallelization, but more fundamentally in the systematic optimization of theoretical approximations and numerical algorithms. This dissertation pursues both directions, with primary emphasis on the latter.

1.1 Quantum Many-Body Problems

The quantum mechanical behavior of electrons interacting within nuclear electrostatic potentials determines the electronic, optical, and thermodynamic properties of molecules and materials [4]. Predicting these properties requires solving the time-independent Schrödinger equation for the system Hamiltonian:

$$\hat{H}|\Psi_{\text{tot}}\rangle = E_{\text{tot}}|\Psi_{\text{tot}}\rangle \tag{1.1}$$

In nonrelativistic quantum mechanics, the Hamiltonian comprises five terms expressed in electron and nuclear momenta and positions:

$$\begin{aligned}\hat{H} = &\sum_i \frac{\hat{\boldsymbol{p}}_i^2}{2m_i} + \sum_A \frac{\hat{\boldsymbol{P}}_A^2}{2M_A} - \frac{e^2}{4\pi\epsilon_0}\sum_{i,A}\frac{Z_A}{|\hat{\boldsymbol{r}}_i - \hat{\boldsymbol{R}}_A|} \\ &+ \frac{e^2}{4\pi\epsilon_0}\sum_{i<j}\frac{1}{|\hat{\boldsymbol{r}}_i - \hat{\boldsymbol{r}}_j|} + \frac{e^2}{4\pi\epsilon_0}\sum_{A<B}\frac{Z_A Z_B}{|\hat{\boldsymbol{R}}_A - \hat{\boldsymbol{R}}_B|}.\end{aligned} \tag{1.2}$$

Here, m_i and M_A denote the masses, $\hat{\boldsymbol{r}}_i$ and $\hat{\boldsymbol{R}}_A$ the position operators, and $\hat{\boldsymbol{p}}_i$ and $\hat{\boldsymbol{P}}_A$ the momentum operators of electron i and nucleus A, respectively. The nuclear charge is Z_A, while $\hbar$, e, and ϵ_0 represent the reduced Planck constant, elementary charge, and vacuum permittivity.

The Born-Oppenheimer approximation decouples electronic and nuclear degrees of freedom by exploiting the large mass ratio between nuclei and electrons, which typically exceeds three orders of magnitude [5]. This mass difference ensures that nuclei move much more slowly than electrons, thereby permitting expansion of the full quantum state in a direct product basis,

$$|\Psi_{\text{tot}}\rangle = \sum_I \sum_{\boldsymbol{R}} \Psi_I(\boldsymbol{R})|\Psi_I(\boldsymbol{R})\rangle \otimes |\boldsymbol{R}\rangle \tag{1.3}$$

Within this representation, the nuclear coordinates $\hat{\boldsymbol{R}} = \{\hat{\boldsymbol{R}}_A\}$ transform from quantum mechanical operators into classical parameters upon which the electronic state depends, while the nuclear momentum operator $\hat{\boldsymbol{P}} = \{\hat{\boldsymbol{P}}_A\}$ acts

as a derivative with respect to these parametric coordinates. This separation consequently yields two coupled problems, namely the determination of the nuclear wavefunction propagating on electronic potential energy surfaces and the solution of the electronic structure at fixed nuclear geometry. Under the Born-Oppenheimer approximation, the electronic Schrödinger equation is therefore obtained as,

$$\hat{H}_{\mathrm{BO}}(\boldsymbol{R})|\Psi_I(\boldsymbol{R})\rangle = E_I(\boldsymbol{R})|\Psi_I(\boldsymbol{R})\rangle \tag{1.4}$$

where $E_I(\boldsymbol{R})$ denotes the electronic energy of the I-th electronic state at fixed nuclear geometry, was named as potential energy surface (PES) in quantum chemistry. The Born-Oppenheimer Hamiltonian takes the form:

$$\begin{aligned}\hat{H}_{\mathrm{BO}}(\boldsymbol{R}) = &\sum_i \frac{\hat{\boldsymbol{p}}_i^2}{2m_i} - \sum_{i,A} \frac{Z_A e^2}{4\pi\epsilon_0|\hat{\boldsymbol{r}}_i - \boldsymbol{R}_A|} + \sum_{i<j} \frac{e^2}{4\pi\epsilon_0|\hat{\boldsymbol{r}}_i - \hat{\boldsymbol{r}}_j|} \\ &+ \sum_{A<B} \frac{Z_A Z_B e^2}{4\pi\epsilon_0|\boldsymbol{R}_A - \boldsymbol{R}_B|}.\end{aligned} \tag{1.5}$$

The Born-Oppenheimer approximation substantially reduces computational complexity and applies broadly across molecular and condensed matter systems [6]. The approximation becomes unreliable when low-lying electronic states exhibit strong variation with nuclear displacement and approach energetic degeneracy, as occurs near conical intersections and in systems with significant vibronic coupling.

Even within the Born-Oppenheimer framework, exact solution of the electronic many-body Schrödinger equation Eq. (1.4) remains computationally intractable for systems of practical interest. The antisymmetry requirement imposed by the Pauli exclusion principle, combined with electron-electron correlations [7], causes the computational cost of exact solutions to scale exponentially with system size [8]. Consequently, developing physically motivated approximations is essential for obtaining tractable numerical solutions. Each

stage of a many-body simulation demands carefully designed approximations; the following discussion addresses the principal considerations.

Solving the electronic Schrödinger equation first requires discretizing the continuous problem using a finite basis set or grid representation. The most popular basis functions have historically been chosen to simplify the required Hamiltonian matrix elements in the basis. They include atomic basis sets (commonly Gaussian basis sets) and plane wave basis sets. In Gaussian bases, a linear combination of Gaussian functions are centered on each nucleus of the problem, i.e.,

$$\chi(\boldsymbol{r}) = (x - A_x)^{l_x}(y - A_y)^{l_y}(z - A_z)^{l_z} \exp\bigl(-\alpha|\boldsymbol{r} - \boldsymbol{A}|^2\bigr), \tag{1.6}$$

where $\boldsymbol{A}$ is the nucleus position, l_x, l_y, and l_z are integers [9]. hese atomic-centred bases offer precise control over the location and shape of the basis functions but are non-orthogonal, which leads to some numerical complications.

Plane wave bases are constructed by placing the system of interest in a finite box of volume V (say cubic, for simplicity) with periodic boundary conditions. This suggests a natural basis function of the form

$$\chi_{\boldsymbol{G}}(\boldsymbol{r}) = \frac{1}{\sqrt{V}} \exp(-i\boldsymbol{G} \cdot \boldsymbol{r}) \tag{1.7}$$

with the wavevectors $\boldsymbol{G}$ chosen to satisfy the boundary conditions. Here, $G_{\max}$ is the maximum wavevector. Plane waves uniformly resolve space and are orthogonal, which leads to well-conditioned numerical algorithms with systematic convergence, although they are not as compact as atomic bases [10].

Other popular choices include numerical grid methods [11], which discretize space into a grid of points and use the values of the wavefunction at these points to construct the basis functions. The Hamiltonian can then be written

in the second quantized form as combination of the creation and annihilation operators of these one-particle basis functions. Researchers employ two distinct strategies for basis discretization:

1. Systematic basis expansion toward the complete basis set limit, targeting quantitative accuracy with controlled error estimates. This strategy predominates in ab initio quantum chemistry [12] and computational materials science.

2. Minimal model construction that retains only essential physical interactions. This philosophy prevails in condensed matter physics, where sophisticated numerical methods extract mechanistic insights from simplified Hamiltonians [7].

These philosophies represent complementary approaches for balancing computational cost against physical fidelity [13]. Increasing computational power continues to blur the boundary between them, enabling hybrid approaches that combine systematic convergence with physical insight.

Once the basis representation is established, an approximate method is selected to solve the resulting discrete problem. Diverse numerical methods have been developed for approximately solving the quantum many-body problem, including wavefunction-based approaches [14], density functional methods [15], and quantum Monte Carlo techniques [16]. These methods differ in their representational completeness, degree of empiricism, computational scaling, numerical stability, and achievable accuracy. No single method dominates across all physical systems and accuracy requirements. Consequently, three considerations guide method selection:

- Is quantitative accuracy required, or do qualitative trends suffice?

- How strongly correlated is the system?
- What computational resources are available?

Advances in computer hardware and high-performance numerical libraries have expanded the scope of tractable simulations, enabling calculations on consumer hardware that were previously accessible only on supercomputers. Developing robust many-body simulation tools requires simultaneous optimization across theory formulation, numerical implementation, and algorithmic design. The field of quantum many-body methods advances rapidly alongside improvements in computational infrastructure. The remaining sections of this chapter introduce four research directions that exploit emerging opportunities in this evolving landscape.

1.2 Density Functional Theory

In computational materials science, density functional theory (DFT) has established itself as the principal computational framework over the past few decades. This framework maps the many-body problem onto an auxiliary system of non-interacting electrons, where each electron experiences an effective potential determined by exchange-correlation functionals acting on the three-dimensional electron density. The mean-field approximation yields a set of single-particle Kohn-Sham equations that can be solved self-consistently,

$$F_{\mathrm{KS}}[\rho]\psi_p(\boldsymbol{r}) = \epsilon_p\psi_p(\boldsymbol{r}), \quad F_{\mathrm{KS}}[\rho] = -\frac{\hbar^2}{2m}\nabla^2 + V_{\mathrm{eff}}[\rho], \tag{1.8}$$

where $V_{\mathrm{eff}}[\rho]$ denotes the effective potential given by

$$V_{\mathrm{eff}}[\rho](\boldsymbol{r}) = V_{\mathrm{ext}}(\boldsymbol{r}) + \frac{e^2}{4\pi\epsilon_0}\int \mathrm{d}\boldsymbol{r}'\frac{\rho(\boldsymbol{r}')}{|\boldsymbol{r}-\boldsymbol{r}'|} + v_{\mathrm{xc}}[\rho](\boldsymbol{r}). \tag{1.9}$$

Here, V_{ext} represents the external potential, corresponding to the nuclear potential for molecular and crystalline systems, and $v_{\mathrm{xc}}[\rho]$ denotes the exchange-

correlation potential, which is a functional of the electron density $\rho(\boldsymbol{r})$ defined as

$$\rho(\boldsymbol{r}) = \sum_{i \in \mathrm{occ}} |\psi_i(\boldsymbol{r})|^2. \tag{1.10}$$

By reducing the many-body problem to a non-interacting formulation, DFT achieves a substantial reduction in computational cost. However, although the theory is exact in principle, the exchange-correlation functional that encapsulates all many-body effects can only be approximated, and no systematic route exists for its improvement. In practice, development of exchange-correlation functionals has proceeded incrementally, and the resulting approximations often exhibit system-dependent performance. As a consequence, DFT-based materials simulations typically provide qualitative guidance rather than definitive quantitative predictions. These inherent limitations motivate the search for alternative approaches capable of achieving systematic improvability.

Within the density functional framework, considerable effort has been devoted to methods based on low-order time-dependent perturbation theory, including the GW approximation and the Bethe-Salpeter equation. These methods generally yield improved accuracy in weakly to intermediately correlated regimes. Nevertheless, their performance in strongly correlated systems remains inconsistent, and systematic pathways for further improvement have yet to be established. An alternative strategy involves a paradigm shift toward wavefunction-based approaches, which have been widely adopted in the quantum chemistry community. Rather than operating on the electron density, a reduced quantity, quantum chemical methods seek to approximate the full wavefunction through expansion in many-body bases constructed from Slater determinants.

1.3 Wavefunction Methods

Hartree-Fock Theory and Configuration Interaction. At the Hartree-Fock level, the ground-state wavefunction is assumed to consist of a single Slater determinant. Based on the variational principle, the Hartree-Fock-Roothaan equations can be derived, with a structure similar to the Kohn-Sham equations presented in Eq. (1.8). Within this context, the most straightforward route to systematic improvement is the configuration interaction (CI) ansatz, which represents one of the earliest electron correlation methods in quantum chemistry [14]. In CI, the ground state is expressed as a linear combination of Slater determinants. For truncated CI methods, this expansion is conveniently written in terms of excitation operators acting on a reference determinant,

$$|\Psi_{\mathrm{CI}}\rangle = \left(1 + \sum_{k=1}^{n} \hat{C}_k\right) |\Phi_0\rangle, \tag{1.11}$$

where $\hat{C}_k$ generates all k-fold excited determinants with variationally optimized coefficients and n specifies the truncation level. Common truncation schemes include CIS ($n = 1$), CISD ($n = 2$), and CISDT ($n = 3$). When all excitations up to the number of electrons are included, the method becomes full configuration interaction (FCI),

$$|\Psi_{\mathrm{FCI}}\rangle = \sum_{I} C_I |\Phi_I\rangle, \tag{1.12}$$

which yields the exact solution within a given one-particle basis and is equivalently termed exact diagonalization in condensed matter physics. The coefficients C_I are obtained by diagonalizing the Hamiltonian matrix in the space spanned by the included determinants. However, the exponentially increasing number of configurations limits FCI to systems containing approximately 16 electrons in 16 orbitals when no additional symmetry is exploited.

In contemporary applications, FCI is commonly employed to describe strong correlation within valence orbitals, often referred to as an active space encompassing all valence configurations. The method has also experienced renewed interest through selected configuration interaction variants, wherein the determinants $|\Phi_I\rangle$ are chosen in a problem-specific manner to sparsely span the Hilbert space [17, 18]. In such approaches, the number of configurations serves as a convergence parameter that can be systematically increased toward the exact result. However, the lack of size extensivity fundamentally limits the application of configuration interaction methods to relatively small systems.

Many-body Perturbation Theory. A systematic framework for incorporating electron correlation beyond the mean-field level is provided by many-body perturbation theory (MBPT) [13]. The approach originates from Rayleigh-Schrödinger perturbation theory and was first applied to many-electron systems by Møller and Plesset using the Hartree-Fock solution as the zeroth-order reference [19]. In quantum chemistry, this formulation is commonly denoted MPn, where n indicates the perturbation order, while in condensed matter physics the term MBPT is more prevalent.

Within this framework, the exact Hamiltonian is partitioned as $\hat{H} = \hat{F} + \lambda\hat{W}$, where $\hat{F}$ denotes the Fock operator, $\hat{W} = \hat{H} - \hat{F}$ represents the fluctuation potential capturing electron correlation, and λ serves as a formal perturbation parameter. The ground-state energy and wavefunction are subsequently expanded as power series in λ, with the physical solution recovered at $\lambda = 1$. To n-th order, the perturbed wavefunction takes the form

$$|\Psi^{(n)}_{\mathrm{MBPT}}\rangle = |\Phi_0\rangle + \mathcal{L}\left[\sum_{k=1}^{n}\left(\frac{\hat{W}\hat{Q}}{E_0 - \hat{F}}\right)^k |\Phi_0\rangle\right], \tag{1.13}$$

where $\hat{Q} = 1 - |\Phi_0\rangle\langle\Phi_0|$ projects onto the space orthogonal to the reference de-

terminant, and $\mathcal{L}$ denotes the linked-diagram operator that eliminates disconnected contributions. This linked-diagram formulation guarantees size extensivity, a critical requirement for meaningful calculations on extended systems. The n-th order energy correction is given by

$$E_0^{(n)} = \langle \Phi_0 | \hat{H} | \Psi_{\mathrm{MBPT}}^{(n-1)} \rangle. \tag{1.14}$$

Within this formulation, the sum of zeroth and first-order contributions recovers the Hartree-Fock energy, rendering the second-order correction (MP2) the lowest non-trivial estimate of the correlation energy. MP2 provides a computationally efficient and often qualitatively accurate correction to Hartree-Fock results, particularly for systems exhibiting a large energy gap between occupied and virtual orbitals, as is typical in small molecules [20].

Extending perturbation theory to higher orders rapidly becomes computationally demanding and does not necessarily improve accuracy, as the perturbation series frequently diverges [21]. To circumvent these limitations, various resummation techniques have been developed that selectively sum certain classes of connected diagrams to infinite order, thereby capturing partial contributions from each perturbative order while avoiding explicit evaluation of high-order terms [22].

Coupled Cluster Theory. Among wavefunction-based approaches, coupled cluster (CC) methods stand as one of the most successful frameworks for treating electron correlation. Similar to MBPT, CC is size extensive but does not satisfy the variational principle. The theoretical foundation can be understood through systematic application of the resummation techniques introduced in the preceding paragraph.

Originally developed by Coester in the 1950s for nuclear structure calculations [23], the method was later reformulated by Čížek for ground-state problems of atomic and molecular systems [24]. Since then, CC theory has achieved remarkable success in quantum chemistry. For weakly correlated systems, these methods provide the most accurate single-reference treatment and are widely regarded as a benchmark standard against which other approximate methods are validated. The framework has also been extended to compute molecular properties including ionization potentials, electron affinities, and electronic excited states [25].

The central ansatz of coupled cluster theory expresses the exact ground-state wavefunction as an exponential acting on the Hartree-Fock reference determinant $|\Phi_0\rangle$,

$$|\Psi_{\mathrm{CC}}\rangle = e^{\hat{T}}|\Phi_0\rangle = e^{\hat{T}_1+\hat{T}_2+\cdots+\hat{T}_N}|\Phi_0\rangle, \tag{1.15}$$

where $\hat{T}$ denotes the cluster operator and $\hat{T}_n$ generates all n-fold excitations from the reference.

In practical calculations, the cluster operator must be truncated at a finite excitation level. Common truncation schemes include CCD ($\hat{T} \approx \hat{T}_2$), CCSD ($\hat{T} \approx \hat{T}_1 + \hat{T}_2$), and CCSDT ($\hat{T} \approx \hat{T}_1 + \hat{T}_2 + \hat{T}_3$). Comparing Eq. (1.15) with the truncated CI ansatz in Eq. (1.11) reveals a key distinction. Although both methods at the same excitation level contain identical numbers of independent parameters, the exponential structure of CC incorporates contributions from higher excitations through products of lower-order cluster amplitudes,

$$\begin{aligned} e^{\hat{T}}|\Phi_0\rangle &= \left[1 + \hat{T} + \frac{1}{2}\hat{T}^2 + \frac{1}{3!}\hat{T}^3 + \cdots\right]|\Phi_0\rangle \\ &= \left[1 + \hat{T}_1 + \left(\frac{1}{2}\hat{T}_1^2 + \hat{T}_2\right) + \cdots\right]|\Phi_0\rangle. \end{aligned} \tag{1.16}$$

These higher-order contributions are not independently optimized but are determined by the lower-order amplitudes, which ensures size extensivity even

under truncation.

The cluster amplitudes can in principle be determined variationally by minimizing the energy expectation value. However, because the cluster operator is not Hermitian, such variational coupled cluster formulations are computationally demanding. The standard approach instead projects the similarity-transformed Schrödinger equation onto the reference and excited determinants. Left-multiplying the Schrödinger equation by $e^{-\hat{T}}$ yields

$$e^{-\hat{T}}\hat{H}e^{\hat{T}}|\Phi_0\rangle = E_0|\Phi_0\rangle. \tag{1.17}$$

Projection onto the reference determinant recovers the energy expression

$$E_0 = \langle\Phi_0|e^{-\hat{T}}\hat{H}e^{\hat{T}}|\Phi_0\rangle, \tag{1.18}$$

while projection onto excited determinants $|\Phi_{ij\cdots}^{ab\cdots}\rangle$ provides the amplitude equations

$$\langle\Phi_{ij\cdots}^{ab\cdots}|e^{-\hat{T}}\hat{H}e^{\hat{T}}|\Phi_0\rangle = 0. \tag{1.19}$$

The number of such equations matches the number of unknown amplitudes, forming a polynomial system that must be solved iteratively.

A key computational advantage of this projection formulation arises from the Baker-Campbell-Hausdorff (BCH) expansion of the similarity-transformed Hamiltonian. Because the Hamiltonian contains at most two-body interactions, this expansion terminates at finite order, enabling efficient evaluation despite the complexity of the resulting expressions.

The computational cost of coupled cluster methods increases steeply with the truncation level. Currently, the most widely employed variant is CCSD(T), which determines single and double excitation amplitudes self-consistently while treating triple excitations perturbatively. This approach reduces the computational scaling by an order of magnitude relative to full CCSDT while

retaining sufficient accuracy to achieve chemical precision for typical closed-shell systems. CCSD(T) is therefore widely adopted as the benchmark standard in quantum chemical calculations.

Other Wavefunction Methods. Beyond the methods discussed above, several other wavefunction-based approaches provide valuable alternatives for treating electron correlation. These include multi-configurational self-consistent field (MCSCF) theory and multi-reference dynamical correlation methods built upon it, matrix product states (MPS) [26, 27], density matrix renormalization group (DMRG) [28–30], tensor network (TN) methods [31], and quantum Monte Carlo (QMC) [32]. Although each method offers distinct advantages for specific chemical problems, all face the challenge of balancing accuracy against computational tractability in extended systems.

To address the intractability of quantum many-body problems, one well-established strategy exploits the locality and decay of correlations [33, 34]. This principle of nearsightedness underlies various quantum embedding and local correlation frameworks. Numerous implementations of these concepts have been developed [35–68], yet they share a common structural feature. Specifically, these methods partition the system into fragments that are subsequently treated either independently or with simplified inter-fragment coupling. In quantum embedding methods, this coupling is typically mediated through self-consistency of a single-particle quantity [68], whereas local correlation methods often employ simplified treatments of spatially separated electron pairs. Consequently, these locality-based frameworks offer a promising route toward accurate and computationally feasible simulations of crystalline materials.

Building on this foundation, the present work focuses on three representative methods to illustrate these complementary strategies, the local natural orbital

coupled cluster method with singles and doubles (LNO-CCSD) [38, 69] for local correlation, and density matrix embedding theory (DMET) [70, 71] along with dynamical mean-field theory (DMFT) [72, 73] for quantum embedding. All three approaches have demonstrated robust performance in crystalline materials across diverse applications [64–66, 69, 74–77].

1.4 Local Natural Orbital Coupled Cluster Method

The LNO-CCSD method approximates the canonical CCSD correlation energy through a divide-and-conquer strategy [37, 38, 78]. The canonical occupied orbitals are first localized via the Pipek-Mezey scheme [79], yielding a set of localized occupied orbitals $\phi_\alpha = \sum_i U_{\alpha i}\psi_i$. For each localized occupied orbital ϕ_α, a local active space $\mathcal{A}_\alpha$ is constructed by diagonalizing the occupied and virtual blocks of the second-order Møller-Plesset (MP2) density matrix. Specifically,

$$D^\alpha_{ij} = \sum_{ab} t_{ia,\alpha b}(2t_{ja,\alpha b} - t_{\alpha a,jb}), \tag{1.20}$$

$$D^\alpha_{ab} = \sum_{ij} t_{\alpha a,jc}(2t_{\alpha b,jc} - t_{jb,\alpha c}), \tag{1.21}$$

where $t_{\alpha a,jb} = (\alpha a|jb)/(f_{\alpha\alpha} + \epsilon_j - \epsilon_a - \epsilon_b)$ is an approximate MP2 amplitude. Diagonalizing the virtual block,

$$D^\alpha_{ab} = \sum_c \xi^\alpha_c X^\alpha_{ac} X^\alpha_{bc}, \tag{1.22}$$

yields a set of localized virtual orbitals $\psi^\alpha_a = \sum_c X^\alpha_{ac}\psi_c$ corresponding to eigenvalues ξ^α_c exceeding a threshold λ_v. Similarly, diagonalizing the projected occupied block,

$$\tilde{D}^\alpha_{ij} = \sum_{kl} Q^\alpha_{ik} Q^\alpha_{jl} D^\alpha_{kl} = \sum_k \xi^\alpha_k Y^\alpha_{ik} Y^\alpha_{jk}, \tag{1.23}$$

where $Q^\alpha_{ij} = \delta_{ij} - \sum_\alpha U_{i\alpha}U_{j\alpha}$ projects out ϕ_α to prevent mixing with other occupied orbitals, yields localized occupied orbitals $\psi^\alpha_i = \sum_k Y^\alpha_{ik}\psi_k$ corresponding to eigenvalues $2 - \xi^\alpha_k$ exceeding a threshold λ_o. Together with ϕ_α,

these orbitals form the local active space $\mathcal{A}_\alpha$. For gapped systems such as the surface models studied in this work, the size of the local active space is much smaller than the total number of orbitals and remains constant with increasing system size at a given accuracy level.

Within each local active space, an effective Hamiltonian $\hat{H}_\alpha$ is constructed by projecting the full Hamiltonian onto the local active space, and the CCSD equations are solved to obtain amplitudes t_{ia} and t_{ijab} as well as the pair correlation energies $\mathcal{E}_{kl}^{\alpha}$. The total correlation energy is evaluated as a sum of fragment contributions,

$$E_{\mathrm{c}} = \sum_{\alpha} E_{\mathrm{c}}^{\alpha} = \sum_{\alpha} \sum_{kl \in \mathcal{A}_\alpha} U_{k\alpha} U_{l\alpha} \mathcal{E}_{kl}^{\alpha} \quad \text{with} \quad \mathcal{E}_{kl}^{\alpha} = \mathcal{E}_{kl}^{\alpha,\mathrm{SD}} + \mathcal{E}_{kl}^{\alpha,(\mathrm{T})}. \tag{1.24}$$

The singles-and-doubles contribution $\mathcal{E}_{kl}^{\alpha,\mathrm{SD}}$ and perturbative triples contribution $\mathcal{E}_{kl}^{\alpha,(\mathrm{T})}$ are computed from the CCSD amplitudes within $\mathcal{A}_\alpha$,

$$\mathcal{E}_{kl}^{\alpha,\mathrm{SD}} = \sum_{iab \in \mathcal{A}_\alpha} (t_{iakb} + t_{ia} t_{kb})(2V_{ialb} - V_{ibla}), \tag{1.25}$$

$$\mathcal{E}_{kl}^{\alpha,(\mathrm{T})} = -\frac{1}{3} \sum_{ij \in \mathcal{A}_\alpha} \sum_{abc \in \mathcal{A}_\alpha} (4w_{kij}^{abc} + w_{kij}^{bca} + w_{kij}^{cab})(v_{lij}^{abc} - v_{lij}^{cba}), \tag{1.26}$$

where

$$w_{kij}^{abc} = \mathcal{P}_{kij}^{abc} \left(\sum_{d} V_{bdak} t_{jcid} - \sum_{l} V_{ckjl} t_{ialb} \right) / \sqrt{-\Delta_{kij}^{abc}}, \tag{1.27}$$

$$v_{kij}^{abc} = w_{kij}^{abc} + \frac{1}{2} \mathcal{P}_{kij}^{abc} V_{aibj} t_{kc} / \sqrt{-\Delta_{kij}^{abc}}. \tag{1.28}$$

Here Δ_{kij}^{abc} denotes the energy gap between the occupied and virtual orbitals, and $\mathcal{P}_{kij}^{abc}$ generates the permutations for three-particle-three-hole tensors.

To further improve accuracy, the calculation is repeated for a series of truncation thresholds. The resulting LNO-CCSD(T) correlation energies are then extrapolated to the full system using the global MP2 correlation energy as a reference.

The computational cost of an LNO calculation comprises three parts:

1. Full-system MP2, required for the LNO construction, scaling as $\mathcal{O}(N^5)$.

2. N_o independent integral transformations for the local Hamiltonian construction, each scaling as $\mathcal{O}(N^5)$ but embarrassingly parallel in N_o.

3. N_o independent correlated calculations of all local Hamiltonians. Since the size of each local active space remains constant for gapped systems, this step scales linearly with system size.

In practice, the $\mathcal{O}(N^5)$ steps often dominate the computational cost for large systems. However, many numerical techniques, such as local domain-based approximations and Laplace transform methods, have been developed to achieve linear scaling for molecular LNO-CCSD(T) calculations. These advances can readily be extended to the periodic LNO-CCSD(T) method described here.

1.5 Dynamical mean-field theory

Over the past three decades, dynamical mean-field theory (DMFT) has established itself as an essential framework for treating strongly correlated crystalline systems, where density functional theory and low-order Green's function methods frequently underestimate or misrepresent correlation-driven phenomena [22]. Metzner and Vollhardt [80] laid the theoretical foundation by demonstrating that the self-energy becomes purely local in the limit of infinite spatial dimensions while retaining its full frequency dependence. Building on this insight, Georges and Kotliar [81] formulated the modern DMFT framework by establishing a self-consistent mapping between the lattice model and an auxiliary quantum impurity problem. This mapping preserves local dynamical correlations that are essential for describing phenomena such as the Mott metal-insulator transition [72].

Central to this mapping is the adoption of the Green's function as the fundamental variable connecting the lattice and impurity problems. The formalism operates within two spatial domains, namely the full lattice and a chosen impurity region that typically comprises a cluster of sites in model systems or a single unit cell in full-cell DMFT. The lattice Green's function $\mathbf{G}_{\mathrm{lat}}(\omega)$ characterizes the full periodic system, where the underlying one-body Hamiltonian $\mathbf{F}_{\mathrm{lat}}$ is obtained from a mean-field calculation such as Hartree-Fock or DFT. Within the impurity region, two Green's functions serve distinct purposes. The low-level Green's function $\mathbf{G}^{\mathrm{LL}}_{\mathrm{imp}}(\omega)$ is extracted as the submatrix of $\mathbf{G}_{\mathrm{lat}}(\omega)$ corresponding to the impurity region. In contrast, the high-level Green's function $\mathbf{G}^{\mathrm{HL}}_{\mathrm{imp}}(\omega)$ is obtained by applying a correlated solver such as FCI or CCSD to an auxiliary (embedding) Hamiltonian constructed from the impurity region. Although both $\mathbf{G}^{\mathrm{LL}}_{\mathrm{imp}}(\omega)$ and $\mathbf{G}^{\mathrm{HL}}_{\mathrm{imp}}(\omega)$ are defined on the same impurity space, they generally differ because they originate from different levels of theory. The central self-consistency condition of DMFT therefore requires that these two quantities match at convergence. To achieve this matching, one introduces a frequency-dependent hybridization function $\mathbf{\Delta}(\omega)$ that encodes the coupling between the impurity and its environment. In the first iteration, the hybridization is initialized as

$$\mathbf{\Delta}(\omega) = \omega\mathbf{1} - \mathbf{F}_{\mathrm{imp}} - [\mathbf{G}^{0}_{\mathrm{imp}}(\omega)]^{-1}, \tag{1.29}$$

where $\mathbf{G}^{0}_{\mathrm{imp}}(\omega)$ denotes the impurity submatrix of the non-interacting lattice Green's function $\mathbf{G}^{0}_{\mathrm{lat}}(\omega) = [\omega\mathbf{1} - \mathbf{F}_{\mathrm{lat}}]^{-1}$.

Given the hybridization function, the impurity problem is formulated through a set of noninteracting bath orbitals designed to reproduce $\mathbf{\Delta}(\omega)$. In bath-based DMFT, the hybridization $\mathbf{\Delta}(\omega)$ is represented by a finite set of discrete bath sites and couplings [82–84]. Unlike approaches that fit along the

imaginary frequency axis, the present work approximates $\mathbf{\Delta}(\omega)$ along the real frequency axis, an approach that yields more accurate dynamical quantities such as spectral functions. To construct the bath representation, one first extracts the spectral density $\mathbf{J}(\epsilon)$ from the hybridization function through the relation [85],

$$\mathbf{J}(\epsilon) = -\frac{1}{\pi} \operatorname{Im} \mathbf{\Delta}(\epsilon + \mathrm{i}\eta), \tag{1.30}$$

where η denotes a broadening parameter. The hybridization function and its spectral density are related via the Hilbert transform, which can be approximated by numerical quadrature along the real axis as

$$\Delta_{ij}(\omega) = \int \mathrm{d}\epsilon \frac{J_{ij}(\epsilon)}{\omega - \epsilon} \approx \sum_t \frac{w_t J_{ij}(\epsilon_t)}{\omega - \epsilon_t} = \sum_{ts} \frac{V_{is}^t V_{js}^t}{\omega - \epsilon_t}, \tag{1.31}$$

where V_{is}^t denotes the impurity-bath couplings obtained by decomposing $w_t \mathbf{J}(\epsilon_t)$, and ϵ_t represents the bath orbital energies.

With these bath parameters determined, the embedding Hamiltonian assumes the form

$$\hat{H}_{\mathrm{emb}} = \hat{H}_{\mathrm{imp}} + \hat{H}_{\mathrm{bath}}, \tag{1.32}$$

where $\hat{H}_{\mathrm{imp}}$ contains the one-body and two-body interactions within the impurity region. The bath Hamiltonian is given by

$$\hat{H}_{\mathrm{bath}} = \sum_t \sum_s \epsilon_t \hat{b}_{ts}^\dagger \hat{b}_{ts} + \sum_t \sum_s \sum_i V_{is}^t \left(\hat{a}_i^\dagger \hat{b}_{ts} + \hat{b}_{ts}^\dagger \hat{a}_i \right). \tag{1.33}$$

Here $\hat{a}_i$ and $\hat{a}_i^\dagger$ denote annihilation and creation operators for impurity orbitals, while $\hat{b}_{ts}$ and $\hat{b}_{ts}^\dagger$ denote the corresponding operators for bath orbitals.

Applying a high-level solver to $\hat{H}_{\mathrm{emb}}$ yields $\mathbf{G}_{\mathrm{imp}}^{\mathrm{HL}}(\omega)$, from which the self-energy is extracted via

$$\mathbf{\Sigma}_{\mathrm{imp}}(\omega) = \omega \mathbf{1} - \mathbf{F}_{\mathrm{imp}} - \mathbf{\Delta}(\omega) - [\mathbf{G}_{\mathrm{imp}}^{\mathrm{HL}}(\omega)]^{-1}. \tag{1.34}$$

The central approximation of DMFT posits that the lattice self-energy can be constructed by tiling the impurity self-energy across all equivalent cells as

$$\boldsymbol{\Sigma}_{\mathrm{lat}}(\omega) = \mathrm{diag}[\boldsymbol{\Sigma}_{\mathrm{imp}}(\omega), \boldsymbol{\Sigma}_{\mathrm{imp}}(\omega), \ldots], \tag{1.35}$$

an approximation that neglects intercluster contributions. The lattice Green's function is then updated according to

$$\mathbf{G}_{\mathrm{lat}}(\omega) = [\omega\mathbf{1} - \mathbf{F}_{\mathrm{lat}} - \boldsymbol{\Sigma}_{\mathrm{lat}}(\omega)]^{-1}, \tag{1.36}$$

and $\mathbf{G}^{\mathrm{LL}}_{\mathrm{imp}}(\omega)$ is subsequently extracted as the impurity submatrix. The hybridization function is then updated for the next iteration according to

$$\boldsymbol{\Delta}(\omega) = \omega\mathbf{1} - \mathbf{F}_{\mathrm{imp}} - \boldsymbol{\Sigma}_{\mathrm{imp}}(\omega) - [\mathbf{G}^{\mathrm{LL}}_{\mathrm{imp}}(\omega)]^{-1}. \tag{1.37}$$

This cycle repeats until $\mathbf{G}^{\mathrm{LL}}_{\mathrm{imp}}(\omega)$ and $\mathbf{G}^{\mathrm{HL}}_{\mathrm{imp}}(\omega)$ converge to identical values. Upon satisfying this condition, the correlation effects captured by the high-level solver propagate throughout the entire lattice, yielding a $\mathbf{G}_{\mathrm{lat}}(\omega)$ of high-level quality.

Although the framework presented above employs a supercell representation of $\mathbf{G}_{\mathrm{lat}}(\omega)$, practical implementations typically exploit translational symmetry by working in reciprocal space. Within this formulation, the lattice Green's function becomes $\mathbf{G}(\omega, \boldsymbol{k})$ [59], while the corresponding self-energy takes the form $\boldsymbol{\Sigma}(\omega, \boldsymbol{k}) = \boldsymbol{\Sigma}_{\mathrm{imp}}(\omega)$. This momentum independence of the self-energy is often presented in the literature as the defining approximation of DMFT, and is equivalent to Eq. (1.35).

1.6 Density matrix embedding theory

Whereas DMFT employs the Green's function as the fundamental connector between lattice and impurity problems, density matrix embedding theory

(DMET) adopts the reduced density matrix as its central variable. Knizia and Chan [70] introduced this alternative embedding framework, drawing on the Schmidt decomposition of quantum states [86, 87] to define a set of rotated basis states that possess entanglement with a preselected fragment. This mathematical structure provides a systematic route to construct bath orbitals without requiring explicit frequency dependence.

To illustrate this formalism, consider a Hubbard model with N sites partitioned into two subsystems, namely an impurity region A containing N_A sites and an environment region B containing N_B sites, where $N_A < N_B$. The wavefunction of the entire system can be expanded on the tensor-product basis of subsystems A and B as

$$|\Psi\rangle = \sum_{IJ} \Psi_{IJ} |A_I\rangle \otimes |B_J\rangle, \tag{1.38}$$

where $|A_I\rangle$ and $|B_J\rangle$ denote orthonormal many-body basis states of A and B, respectively. Factorizing the coefficient tensor Ψ_{IJ} via singular value decomposition (SVD) yields

$$\begin{aligned} |\Psi\rangle &= \sum_{\sigma} S_\sigma \left(\sum_I U_{\sigma I} |A_I\rangle \right) \left(\sum_J V^*_{\sigma J} |B_J\rangle \right) \\ &= \sum_{\sigma} S_\sigma |\alpha_\sigma\rangle |\beta_\sigma\rangle, \end{aligned} \tag{1.39}$$

which constitutes the Schmidt decomposition of a general quantum state [86]. The Schmidt basis states $|\beta_\sigma\rangle$ span a subspace in the environment with the same dimension as the impurity, thereby providing a natural definition of the bath states. Consequently, the Hilbert space dimension reduces to 2^{N_A} regardless of the total lattice size. This reduction enables projection of the original lattice Hamiltonian onto the embedding space as

$$\hat{H}_{\text{emb}} = \hat{P}\hat{H}\hat{P} \quad \text{with} \quad \hat{P} = \sum_{\sigma} |\alpha_\sigma\rangle|\beta_\sigma\rangle\langle\alpha_\sigma|\langle\beta_\sigma|. \tag{1.40}$$

One can verify that the embedding Hamiltonian shares the same ground state energy as the original Hamiltonian, since $\langle\Psi|\hat{P}\hat{H}\hat{P}|\Psi\rangle = \langle\Psi|\hat{H}|\Psi\rangle = E_0$. This property establishes the foundation for exact embedding.

In practice, however, the exact wavefunction remains unknown, and approximations become necessary. The key idea is to construct the wavefunction iteratively in a self-improving manner. When the low-level solution takes the form of a mean-field Slater determinant, the bath states reduce to a set of single-particle orbitals whose overlap with the fragment is non-zero [70, 71]. These bath orbitals can be constructed from either the molecular orbital (MO) coefficients or the corresponding one-body reduced density matrix. The occupied block of the MO coefficients can be written in a bipartite form as

$$\mathbf{C}^{\mathrm{occ}} = \begin{bmatrix} \mathbf{C}_A^{\mathrm{occ}} \\ \mathbf{C}_B^{\mathrm{occ}} \end{bmatrix}, \tag{1.41}$$

where $\mathbf{C}_A^{\mathrm{occ}}$ and $\mathbf{C}_B^{\mathrm{occ}}$ have dimensions $N_A \times N_{\mathrm{occ}}$ and $N_B \times N_{\mathrm{occ}}$, respectively. In the following derivation, we assume $N_{\mathrm{occ}} > N_A$.

Performing an SVD on $\mathbf{C}_A^{\mathrm{occ}} = \mathbf{U}_A\mathbf{\Sigma}_A\mathbf{V}_A^\dagger$ identifies the components in $\mathbf{C}_B^{\mathrm{occ}}$ that have nonzero overlap with A. The matrix $\mathbf{V}_A$, with dimensions $N_{\mathrm{occ}} \times N_{\mathrm{occ}}$, defines the rotation that transforms the MOs into embedding orbitals (EOs). Since this rotation operates within the occupied space, it does not alter the mean-field state as

$$\bar{\mathbf{C}}^{\mathrm{occ}} = \mathbf{C}^{\mathrm{occ}}\mathbf{V}_A = \begin{bmatrix} \mathbf{U}_A\ \mathbf{\Sigma}_A \\ \mathbf{C}_B^{\mathrm{occ}}\mathbf{V}_A \end{bmatrix} = \begin{bmatrix} \mathbf{P} & \mathbf{0} \\ \mathbf{Q} & \mathbf{E} \end{bmatrix}. \tag{1.42}$$

In the resulting block structure, $\mathbf{P}$ has dimensions $N_A \times N_A$ and represents the rotated impurity orbitals. The matrix $\mathbf{Q}$ has dimensions $N_B \times N_A$ and represents the environment components having nonzero overlap with A. The matrix $\mathbf{E}$ has dimensions $N_B \times (N_{\mathrm{occ}} - N_A)$ and represents the environment

components with zero overlap, corresponding to the core orbitals that remain doubly occupied. Orthonormalizing $\mathbf{Q}$ yields the bath orbitals $\mathbf{B}$, which, together with the identity matrix for the impurity part, define the transformation matrix $\mathbf{C}^{\mathrm{AO,EO}}$ from atomic orbitals (AOs, or the site basis in a lattice model) to the embedding space as

$$\mathbf{C}^{\mathrm{AO,EO}} = \begin{bmatrix} \mathbf{I} & \mathbf{0} \\ \mathbf{0} & \mathbf{B} \end{bmatrix}. \tag{1.43}$$

Alternatively, the bath orbitals can be obtained by performing an SVD on the off-diagonal block of the one-body reduced density matrix. Regardless of the construction route, the number of bath orbitals equals the number of impurity orbitals, and their spatial distribution exhibits larger weights on sites near the fragment, reflecting the local character of electron correlation.

Once the transformation in Eq. (1.43) is established, the global Hamiltonian can be projected onto the embedding space. In the interacting bath formalism [70, 71], all terms in the lattice Hamiltonian undergo transformation, and two-electron interactions among bath orbitals generally remain non-zero. A simpler alternative is the non-interacting bath formalism [70], where the bath orbitals remain non-interacting and the two-body integrals involving bath indices are effectively replaced by a one-body correlation potential. Within this non-interacting bath formalism, the embedding Hamiltonian closely resembles that employed in DMFT (see Section 1.5).

Several properties of this embedding procedure merit attention. First, the number of electrons in the embedding Hamiltonian exactly equals the number of impurity orbitals, rendering the embedded problem half-filled. This property follows from the structure of $\mathbf{E}$ in Eq. (1.42), since the number of core orbitals is $N_{\mathrm{occ}} - N_A$, leaving exactly N_A electrons in the embedding space.

This integer electron number constitutes a distinctive feature of DMET compared to other embedding schemes, where the embedded electron number may not be an integer. Second, the embedding becomes exact in several limiting cases, including the isolated atom limit where no coupling exists between impurities and thus no bath is required, the noninteracting limit with $V = 0$, and the Hartree-Fock-in-Hartree-Fock embedding where both lattice and impurity problems are solved at the HF level.

The embedding Hamiltonian is solved using a high-level impurity solver, typically one of the many-body quantum methods introduced in Section 1.1, such as full configuration interaction, coupled cluster theory, or density matrix renormalization group. As long as the solver provides the reduced density matrices, expectation values can be evaluated from the solution. For local properties within a single impurity, these can be obtained directly from the solver density matrices. For nonlocal properties across different impurities, however, democratic partitioning can be employed. Specifically,

$$\langle a_i^\dagger a_j \rangle = \frac{1}{2}\left(\langle \Psi^I | a_i^\dagger a_j | \Psi^I \rangle + \langle \Psi^J | a_i^\dagger a_j | \Psi^J \rangle \right), \tag{1.44}$$

where indices i and j denote local orbitals belonging to clusters I and J, respectively, and the result is averaged between the two embedding problems.

Beyond computing expectation values, the high-level solution can also improve the low-level theory through self-consistency. This is typically achieved by introducing a correlation potential $\hat{u}$ that minimizes the density matrix difference between the two levels of theory. Mathematically, this corresponds to a least-squares minimization as

$$\min_{\mathbf{u}} \sum_{ij} \left\| \mathbf{P}(\mathbf{u})^{\mathrm{LL}} - \mathbf{P}^{\mathrm{HL}} \right\|^2, \tag{1.45}$$

where $\mathbf{P}^{\mathrm{HL}}$ is obtained from the impurity solver and held fixed during the minimization, while the fitted density matrix $\mathbf{P}^{\mathrm{LL}}$ is generated from the mod-

ified lattice mean-field Hamiltonian $\hat{F} + \hat{u}$. In practice, the fitting can be performed on a subset of the impurity orbitals to reduce the computational cost and improve numerical stability.

The specific form of $\hat{u}$ determines possible ways of breaking symmetry. A generic form is

$$\hat{u} = \sum_{ij\sigma} u_{ij}^{\sigma} \hat{a}_{i\sigma}^{\dagger} \hat{a}_{j\sigma}, \tag{1.46}$$

where $\mathbf{u}$ contains spin-unrestricted parameters ($\sigma = \alpha$ or β) that can generate spin-symmetry-breaking magnetic orders. Other types of correlation potentials can also be introduced to break particle number symmetry and allow for superconducting pairing orders. The entire DMET self-consistency procedure is then repeated until $\mathbf{P}$ converges.

1.7 Comparison between DMET and DMFT

DMET shares deep conceptual parallels with Dynamical Mean-Field Theory (DMFT) [72, 73]. Fundamentally, both methods map the complex lattice problem onto an embedded impurity model, where a local cluster is coupled to a set of bath orbitals representing the thermodynamic environment. Furthermore, both employ a self-consistency loop to propagate local correlation effects back to the macroscopic lattice. These methods also share specific exact limits; for instance, both recover the non-interacting and atomic limits exactly, and DMFT is notably exact in the limit of infinite spatial dimensions [72].

At a schematic level, the quantities governing the self-consistency conditions play analogous roles in the two theories:

$$\mathbf{P} \leftrightarrow \mathbf{G}_{\mathrm{imp}}(\omega), \quad \mathbf{u} \leftrightarrow \mathbf{\Delta}(\omega). \tag{1.47}$$

Here, the static one-body density matrix $\mathbf{P}$ and the correlation potential $\mathbf{u}$ in DMET act as the static counterparts to the frequency-dependent impurity Green's function $\mathbf{G}_{\mathrm{imp}}(\omega)$ and the hybridization function $\mathbf{\Delta}(\omega)$ in DMFT, respectively.

A fundamental difference is established by the frequency dependence of the Green's function, which renders DMFT intrinsically a theory of excited states. Consequently, the local spectral function can be extracted from the Green's function and subsequently compared directly with experimental measurements, including X ray photoemission spectroscopy and bremsstrahlung isochromat spectroscopy. Conversely, DMET is formulated as a static theory where density matrices are employed as the basic variable. As these are viewed as equal time or frequency integrated Green's functions, DMET is deemed more suitable for problems concerning the ground state. Furthermore, a distinction is observed regarding the number of bath orbitals. In DMET, the number of bath orbitals is restricted to match the number of impurity orbitals, whereas an infinite number is implied in DMFT. Consequently, bath discretization errors are inevitably introduced in the latter. The compact bath representation in DMET typically offers better computational efficiency than DMFT.

Chapter 2

Ab initio quantum many-body description of superconducting trends in the cuprates

This chapter is based on the following publication:

[1] Z.-H. Cui, **Yang, Junjie**, J. Tölle, H.-Z. Ye, S. Yuan, H. Zhai, G. Park, R. Kim, X. Zhang, L. Lin, T. C. Berkelbach, and G. K.-L. Chan, "Ab initio quantum many-body description of superconducting trends in the cuprates", Nat Commun **16**, 1845 (2025),

2.1 Introduction

Since the discovery of high-temperature superconductivity in the cuprates almost 40 years ago, obtaining a microscopic description of the phenomenon has challenged theoretical material science [88, 89]. In particular, the search for new materials with higher transition temperatures has been hindered by the absence of predictive computational links between the material structure/composition and the observed superconducting temperatures. Here, we describe microscopic calculations that reproduce some of the best-known material trends in cuprate superconducting critical temperatures T_c via the direct ab initio computation of the ground-state pairing order, using only the material structure as input. These rely on new methods to solve the quantum

many-body Schrödinger equation in the materials without first simplifying to low-energy models. Analyzing the solutions identifies simple descriptors which correlate with transition temperature and the fluctuations that drive the microscopic process of pairing. Overall, our methodology demonstrates a path towards predictive ab initio computations of high-temperature superconductivity in new materials.

Cuprate superconductors are layered perovskite compounds with two-dimensional copper-oxygen planes separated by buffer layers of atoms, which dope the planes either with electrons or holes. In the parent undoped state, the materials are antiferromagnets, becoming superconducting after doping beyond $\sim$10%. Out of the many efforts to increase T_c through altering the composition and structural parameters, some trends can be identified. Two of the clearest ones are the pressure effect and layer effect. In the pressure effect, T_c increases with pressure applied in the plane, rising, e.g. in Hg-1223 from 135 K at ambient pressure to 164 K at 30 GPa [90, 91]. In the layer effect, T_c increases with the number of stacked copper-oxygen planes (e.g. in the mercury-barium cuprates, T_c is 97, 127, 133 K in the 1-, 2-, 3-layer compounds [92]).

Many theories have been proposed to rationalize cuprate superconductivity, but it has proven difficult to obtain a quantitative microscopic picture, and even harder to reproduce the specifics of different cuprate materials. There are two essential complications. First, the phenomenon arises from quantum many-body physics with strong electron interactions, where there are no analytical solutions and no obvious small parameter [93]. (This is in contrast to conventional superconductors with weak electron interactions, where material specific computations are relatively successful [94, 95]). Within any microscopic framework to describe the electron correlation, the predictions thus carry uncertainty from their approximate nature. The second is that the com-

plex material composition complicates the derivation of low-energy Hamiltonians. While one-band Hubbard models and their relatives have informed much current thinking [96, 97], recent accurate numerical solutions of these models have also highlighted the deviation of the model physics from that of the real materials [98–102]. In addition, although there has been progress in rationalizing material specific effects in terms of parametrized multi-band models [97, 103–105]the uncertainty introduced into the Hamiltonian arising from downfolding, for instance, due to density functional theory double-counting [106], the definition of impurity orbitals [107], or the difficulties of parametrization or uncertainty of the parametrized form [108], appears comparable to the strength of the material trends.

In principle, solving the ab initio many-electron Schrödinger equation for the full cuprate material provides an unambiguous and quantitative route to understanding cuprate superconductivity. Although this is traditionally viewed as intractable, recent advances in numerical many-body algorithms and their computational implementation are opening up the possibility of predictive ab initio computation even in strongly correlated quantum materials. While such calculations are more expensive than their model counterparts and thus more limited in the system size that can be treated, they are complementary to the low-energy model approach as the microscopic Hamiltonian unambiguously reflects the material-specific composition, at the expense of a less detailed description of long-range physics. As one example of the success of such a strategy, we previously captured, and illuminated at the atomic level, systematic trends in the magnetism of the parent state of the cuprates with such an approach [109]. Here, we show how these strategies may be extended to the much more challenging doped phases of the cuprates, and in particular to obtain the superconducting pairing order. Below, we describe the advances

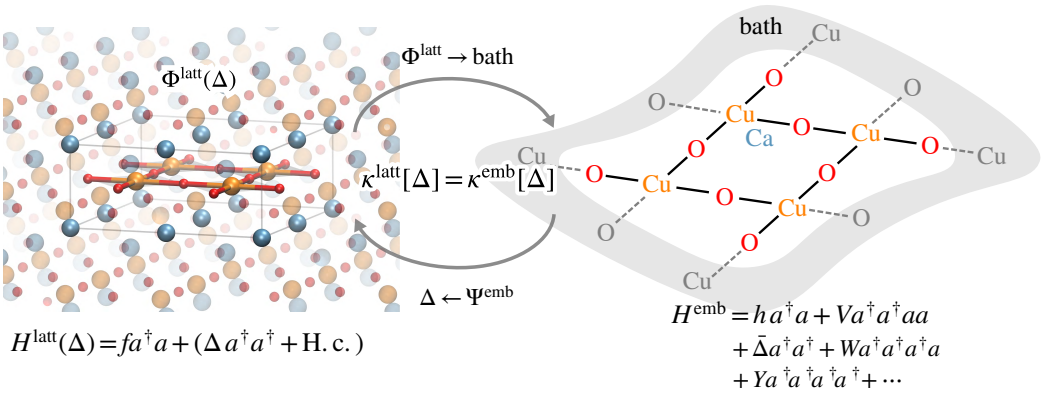

Figure 2.1: The ab initio density matrix embedding theory (DMET) framework. This involves solving two ground-state problems: for an auxiliary mean-field Hamiltonian (left), $H^{\text{latt}} = f + \Delta \to \Phi(\Delta)$, and a quantum impurity + bath Hamiltonian (right), $H^{\text{emb}}(\Delta) \to \Psi^{\text{emb}}(\Delta)$. Δ is modified by self-consistent iteration until the pairing order κ is the same in the impurity and the auxiliary mean-field problem. The non-number-conserving $\bar{\Delta}, W, Y$ terms in H^{emb} arise from the DMET bath construction from $\Phi(\Delta)$. In this work, the bulk problem is represented by 128 cuprate unit cells, and the impurity is a 2×2 supercell, illustrated above for CCO ($CaCuO_2$)

.

that now make this work possible, the cuprate systems we will study for their systematic trends, and the results and insights that derive from this approach.

2.2 Methodology

Atomic modelling of doping

The hole or electron doping of cuprates is usually generated by chemical doping, which involves substituting buffer layer ions or introducing additional ions. For example, La_2CuO_4 is typically doped by replacing some of the La (III) ions with Sr (II) ions; because the entire crystal remains neutral, this means that charge must be taken out of the cuprate plane, effectively doping the plane with holes. Another example particularly relevant to this work is the hole doping of Hg-based cuprates, where oxygen is introduced into the Hg buffer layer, whose charge must then be compensated by other ions, including from the

CuO_2 plane. Note that the effective doping of the CuO_2 plane is not always simple to determine from the dopant atom concentration alone, as charge can be redistributed across many different atoms. Consequently, the best way to simulate chemical doping is to use explicit dopant atoms. Unfortunately, the corresponding supercells become large and thus difficult to treat.

A simple way to dope without using explicit dopants is provided by the **rigid band approximation** (RBA). In this case, one directly removes or adds charge to the system, and assumes that there is a neutralizing background charge. This is similar in spirit to doping in lattice models, which is performed simply by modifying the number of particles.

Another method is the **virtual crystal approximation** (VCA) [110, 111], where the nuclear potential is obtained by mixing different site compositions, e.g. if a lattice site has x probability being occupied by atom A, and $(1-x)$ probability by atom B, the VCA nuclear potential is defined as,

$$\bar{H}^{\mathrm{VCA}}_{\mathrm{nuc}}(\boldsymbol{r}) = xV^{\mathrm{A}}_{\mathrm{nuc}}(\boldsymbol{r}) + (1-x)V^{\mathrm{B}}_{\mathrm{nuc}}(\boldsymbol{r}). \tag{2.1}$$

This approximation is still very crude as one can imagine that the effect of a half-occupied oxygen ($Z = 8$) site is fundamentally different to the potential from a Be atom ($Z = 4$).

Mean-field settings

The single particle mean-field (SCF) calculations (HF, DFT) were carried out using the crystalline Gaussian atomic orbital basis representation in the PySCF package [112, 113]. The results of these calculations were cross-checked against plane wave basis calculations using the VASP package [114–118]. For CCO and the Hg-based cuprates, we used the correlation consistent double-ζ basis GTH-cc-pVDZ defined above, using the GTH pseudopotential

for the core electrons [119, 120]. Gaussian density fitting was used to compute the two-electron integrals. We used a specially-optimized Gaussian basis as the density fitting auxiliary basis for Cu, O and Ca; and used the def2-TZVP-RI basis for the auxiliary basis of Hg and Ba ($n_{\mathrm{aux}} \sim 5n_{\mathrm{AO}}$).

For the plane wave basis calculations, a projector-augmented wave (PAW) [118, 121] representation was used to treat the core electrons and we used a plane wave kinetic energy cutoff of 500 eV.

We sampled the Brillouin zone with a Γ-centered k-mesh: we used $4 \times 4 \times 2$ for the 2×2 supercell of the single layer compounds CCO and Hg-1201; $4 \times 4 \times 1$ for the 2×2 supercell of the double-layer compound Hg-1212.

All mean-field calculations used a Fermi-Dirac smearing of 0.2 eV. All mean-field calculations were converged to an accuracy of better than 10^{-8} a.u. per unit cell.

We used the PBE0 [122] hybrid functional for all doping RBA and VCA concentrations. All calculations were spin-unrestricted so that the AFM order could be stabilized at the DFT level. HF calculations were also performed, but we found that these gave very poor descriptions of the doped states.

In general, it is important to note that the basic features of the charge density are established by the choice of mean-field and the choice of doping representation rather than the DMET self-consistency, as the self-consistency is performed here on the anomalous part of the correlation potential.

DMET settings

All DMET routines, including the bath construction, integral transformation, solver interface, and correlation potential fitting, were implemented in the libDMET package [123, 124]. To remove core orbitals (which make the bath

construction unstable and increases the computational cost) we froze the lowest mean-field bands ($3s3p$ bands for Cu and Ca, $2s$ bands for O, $5s$ bands for Ba); and we also froze the Cu $4f$ and O $3d$ virtuals to further reduce the cost.

We added the correlation potential u to the CuO_2 three-band orbitals and *only* fitted the three-band orbital anomalous blocks of the density matrices, i.e., $\langle a_{i\alpha} a_{j\beta} \rangle$ where $ij \in$ three-band orbitals (the self-consistency of the normal magnetic part is not considered in this work). We also enforced C_{2h} symmetry in u. The initial guess of u was chosen as a d-wave pattern on Cu $3d_{x^2-y^2}$ orbitals with a small amplitude 10^{-3}. The convergence criterion on the DMET self-consistency was chosen such that the maximal change of an element in u was less than 5×10^{-4} a.u..

In the DMET mean-field and correlation fitting, a small smearing of $\beta = 1/k_{\mathrm{B}}T = 1000$ a.u. was added to the lattice.

We used the Newton-Krylov GCCSD methods implemented in MPI4PYSCF [125] as solvers. The CCSD T and Λ equations were converged to a residual of less than 10^{-4} a.u. The largest embedding problem we treated using the GCCSD solver was of size (376o, 188e), with multiple such size fragments solved simultaneously in the multi-fragment embedding formalism.

For TCCSD, we use an active space of 16 spin orbitals, defined from the CCSD natural orbitals. The active space was solved by the exact diagonalization.

Ab initio DMRG in the generalized spin orbital formalism was implemented in BLOCK2 package [126]. A series of active spaces of 16, 32, 48, 64 orbitals (using CCSD natural orbitals in the last DMET iteration) were solved by DMRG with a maximal bond dimension $M = 3000$.

2.3 Results and Discussions

Ab initio impurity solver benchmarks and order parameters

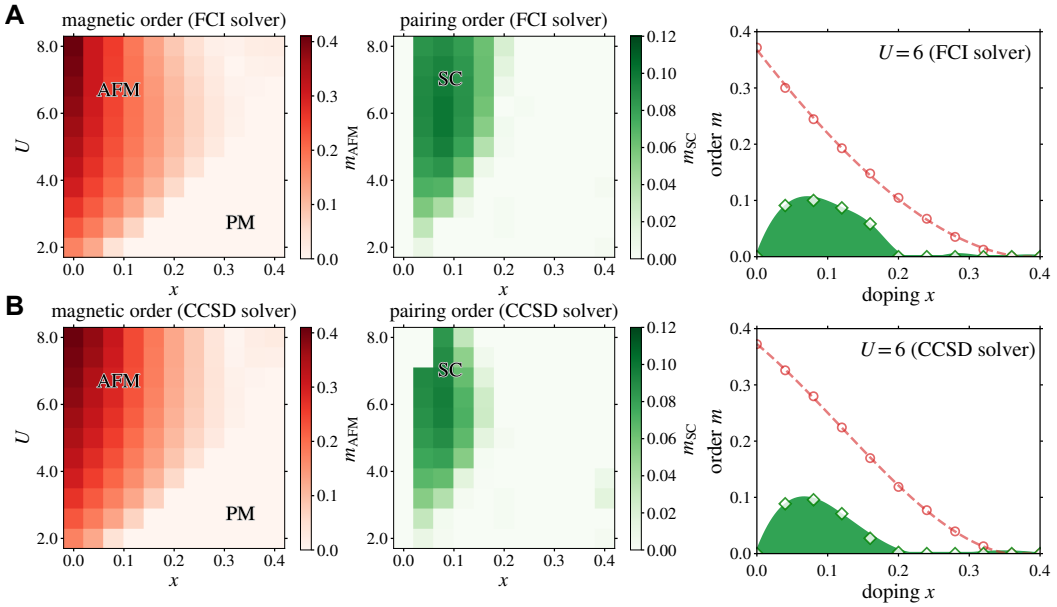

Figure 2.2: **Benchmark of impurity solver on the phase diagram of the one-band Hubbard model.** 2×2 impurity is embedded in 40×40 square lattice. The figure plots the magnetic (AFM, paramagnetic (PM)) and pairing order (d-wave) for different U and doping x from (A) FCI (exact diagonalization) solver and (B) CCSD solver.

Fig. 2.2 shows AFM order and d-wave pairing order computed using a 2×2 plaquette impurity embedded in the 1-band 2D Hubbard model using an exact diagonalization (FCI) solver and the CCSD solver. (Note that this data is intended to test the quality of the CCSD solver, rather than report on the detailed physics of the 2D Hubbard model). As can be seen, the CCSD solver provides a quantitatively accurate impurity solver for the magnetic order at all dopings. The pairing order from the CCSD solver is slightly less accurate, but still shows quite good agreement with the exact diagonalization solver up to $U = 6$. The main discrepancy from ED at $U = 8$ is the width of the SC dome, which is narrower when using the CCSD solver.

The pressure effect

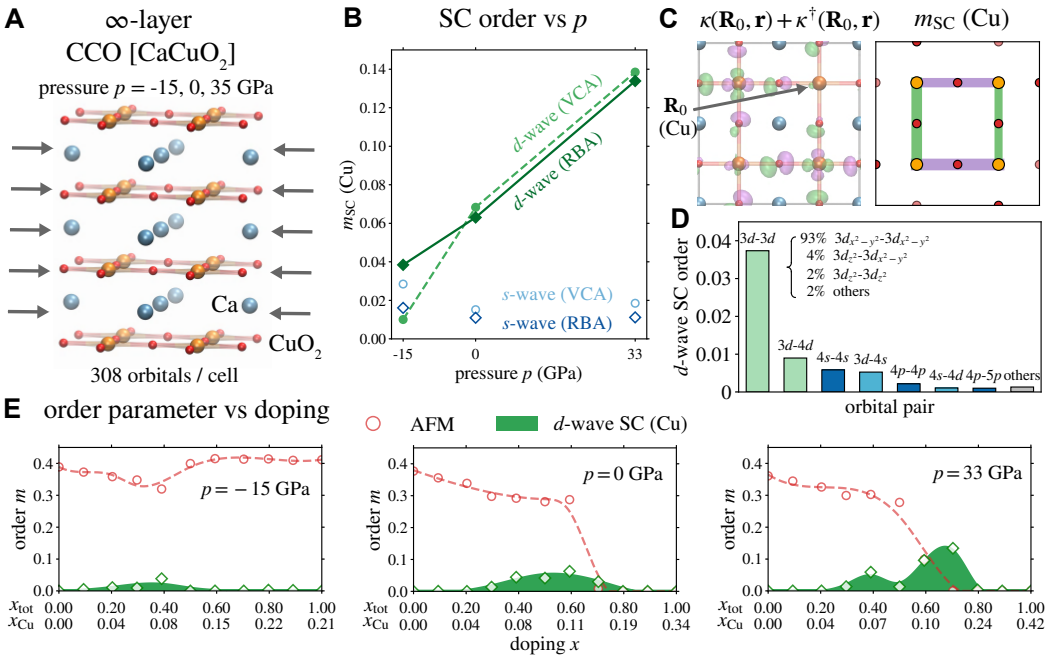

Figure 2.3: **Superconducting order and pressure effect.** (A) Structure of the ∞-layer cuprate CCO ($CaCuO_2$). (B) d-wave and s-wave order as a function of pressure p, using different doping representations (rigid band approximation (RBA) and virtual crystal approximation (VCA)). (C) Anomalous density $\kappa(\boldsymbol{R}_0, \boldsymbol{r}) + \kappa^\dagger(\boldsymbol{R}_0, \boldsymbol{r})$ for CCO at optimal doping and ambient pressure. The reference point $\boldsymbol{R}_0$ is near the Cu atom in the embedded cell. $m_{\rm SC}$ (Cu): pairing order between neighboring Cu atoms showing d-wave symmetry. (D) Orbital-resolved d-wave SC orders between Cu orbital pairs. (E) AFM and SC order as a function of doping using RBA.

We first examine the computed order in CCO at three different in-plane pressures: -15, 0 (ambient), 33 GPa. Without doping, CCO is in an antiferromagnet. At all pressures, under sufficient doping, a superconducting state is formed with predominantly d-wave pairing order, as illustrated by the Cu-Cu pairing order at optimal doping in Fig. 2.3B; the d-wave character increases with increased pressure. There is also a small s-wave piece in the Cu-Cu pairing, and the total order has a small p-wave component necessarily arising from the coexistence of AFM and d-wave superconducting order [101]. The uncertainties of the calculation mean that the absolute numerical values for

the order should be treated with caution. However, if we use $m_{\mathrm{SC}}^{\mathrm{max}} \propto T_{\mathrm{c}}$ and assume $T_{\mathrm{c}} \sim 100$ K at ambient pressure, then $\mathrm{d}T_{\mathrm{c}}/\mathrm{d}P \approx 3$ K/GPa, of the same order as that typically seen in experiments (1-2 K/GPa) [127, 128]. Our calculations thus capture a reasonable pressure effect on the maximum superconducting order.

Fig. 2.3C shows a real-space visualization of the Cu-centered pair amplitude, and the scalar pair amplitude between orbitals on neighboring Cu atoms, for CCO at ambient pressure and optimal doping. The sign of the pairing amplitude illustrates the d-wave symmetry, while the spread (not shown) corresponds to a pair distributed across a linear distance of about 6 unit cells. We show a more detailed orbital resolved analysis of the Cu-Cu d-wave order at optimal doping in Fig. 2.3D.

We find that O-O pairing contributes about 30% to the total d-wave order, with Cu-O pairing contributing mainly to the p-wave order.

We now examine in detail the AFM and SC orders as a function of doping in Fig. 2.3E. We first discuss the x-axis, the doping axis. When holes are added, the charges go primarily to the CuO_2 plane, and reside mainly on oxygen ($2p$), with a fraction (about 20% - 30%) transferred to Cu; about 90% of the charge resides in the three-band orbitals (Cu $3d_{x^2-y^2}$ and O $2p_{x,y}$). Because the uncompensated moment lies almost entirely on Cu, but the holes reside in hybridized Cu-O orbitals (i.e. the band that is doped does not contain all the uncompensated spin density), the holes do not directly quench the local moment, unlike in the 1-band Hubbard model. Therefore, the decay of the local magnetic order with respect to x_{tot} (number of holes per unit cell) is much slower than in the 1-band Hubbard model, although it is similar to that seen in three-band models for some parameter choices [129]. Our method

retains some dependence on the bulk mean-field charge density, so we can obtain unusual behaviour when this charge density is poor. This appears to be the case in the -15 GPa system, where the moment does not decrease even under heaving doping. However, the slow decay of local magnetic order should not be interpreted as a slow decay of global AFM order, as we are missing long-range fluctuations.

In experiments on oxygen doped cuprates, such as yttrium barium copper oxide [130] and the mercury barium cuprates studied later [131], the effective Cu doping is usually not taken from the estimated oxygen content, which (depending on the assumed formal charge of the dopants) could translate to very large copper-oxygen plane dopings. Instead, the effective doping of the copper-oxygen plane is inferred from an empirical formula [130, 131]. Our doped charges only partially reside in the copper-oxygen plane, thus it is interesting to analogously replace the bare doping here with the effective Cu doping computed from the atomic populations, x_{Cu}. We then see that the maximum d-wave order appears at dopings (10%-15%) similar to that seen in one-band treatments [132], as well as in the experimental empirical Cu dopings. The optimal doping is close to the point at which the magnetic order suddenly drops. The SC dome contains a double peak structure; this has been seen before in three-band models [129], and appears to be related to the finite size of the impurity cluster.

The quantitative magnetic and pairing orders depend on details of the doping treatment: for example, the difference in the maximum pairing order between a VCA and RBA treatment is shown in Fig. 2.3B. This highlights the need to investigate more realistic representations of dopants. However, the qualitative pressure trend in the pairing order is reproduced in either case.

The layer effect

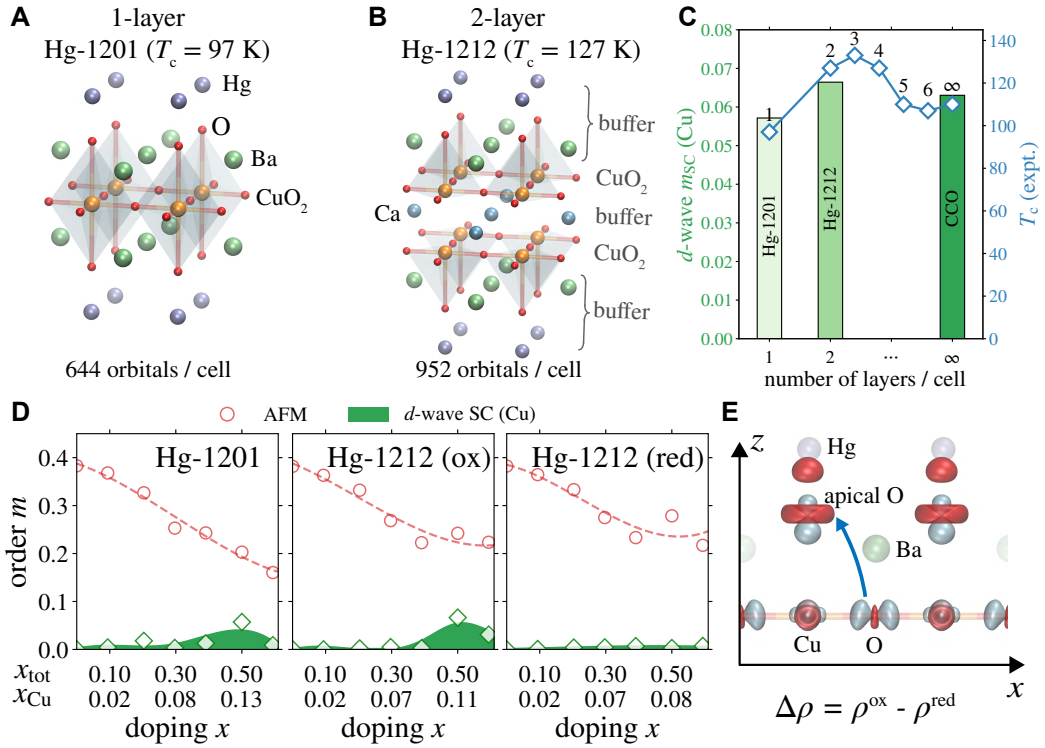

Figure 2.4: **Layer effect.** Structures of (A) single-layer Hg-1201 ($HgBa_2CuO_4$) and (B) double-layer Hg-1212 ($HgBa_2CaCu_2O_6$); (C) Comparison between calculated d-wave SC orders (Hg-1201, Hg-1212, and CCO) and experimental T_c (data from [92, 133]) as a function of the number of layers per cell. (D) AFM and SC orders of different compound structures (Hg-1201, oxidized Hg-1212, and reduced Hg-1212). (E) Electron density difference between oxidized and reduced Hg-1212 at optimal doping (red: increased electron density of oxidized vs. reduced, blue: decreased electron density). Arrow indicates the transfer of charge between reduced and oxidized structures.

We next consider the layer effect in the mercury barium cuprates (1-, 2-layer) and CCO (∞-layer) compounds. The plot of the maximum pairing order as a function of the layer number is shown in Fig. 2.4C. We see a sizable increase in the maximum pairing order moving from Hg-1201 to Hg-1212 (ox), similar to the experimental change in T_c. We thus capture the basic experimental trend in T_c of the layer effect. For more than 3 layers, experimentally it is seen that T_c no longer increases, which has been attributed to the potentially

inhomogeneous doping of the different copper-oxygen planes. In CCO, inhomogeneous doping is not part of our representation, however, the pairing order decreases slightly from Hg-1212 to CCO, similar to the experimental trend between 3-6 layers, although the small magnitude of the change is challenging within the uncertainty of our numerical approach. Our result for CCO is also in good agreement with the T_c for the mixed Sr/CCO compound (assuming that reflects the T_c of CCO).

The pairing and magnetic orders are shown in Fig. 2.4D. The qualitative behavior in the mercury-barium cuprates is similar to that in CCO, although here, the hole density is less localized on the Cu atoms, and some fraction goes to buffer atoms (e.g. apical oxygen orbitals). There are other important microscopic differences between the mercury-barium compounds and CCO. For example, in CCO, the magnetic order at half-filling decreases between ambient and 33 GPa pressure, and this is reflected in the more rapid decrease of the local moment close to optimal doping. However, even though the local moment in Hg-1212 decays more slowly than in Hg-1201, the optimal pairing order is larger.

The argon-reduced Hg-1212 structure is similar to the oxygenated structure but has a larger apical Cu-O distance (by about 0.04 Å). Although the experimental sample corresponds to very low oxygen doping where it is not expected to superconduct, it is still observed to have a $T_c \sim 92$ K [134], leading to speculation about complex charge-transfer behaviour in mercury barium cuprates. We find that the undoped magnetic behaviour (e.g. exchange couplings and charge distribution) is almost identical in the Hg-1212 (ox) and Hg-1212 (red) structures (see Table S4). Nevertheless, as we dope the reduced structure, we find that holes distribute differently in the reduced and oxidized form, especially near optimal doping ($x_{tot} \sim 0.5$) where the effective Cu doping is smaller

in the reduced structure than the oxidized structure, along with a reduction in pairing order (as in the experiment, but much larger in magnitude). The difference in the Hg-1212 (ox) and Hg-1212 (red) electron densities is shown in Fig. 2.4E: the main difference corresponds to a transfer of charge from the in-plane O $2p$ orbitals in the (red) structure, to the apical O and Hg orbitals in the (ox) structure, leaving the Hg-1212 (ox) with a larger in-plane doping. The sensitivity of pairing order to the charge distribution highlights the need to further investigate the treatment of doping and the charge density. Overall, the complicated behaviour confirms the importance of atomic scale crystal structure in the development of the pairing order in these multicomponent, multilayer cuprates.

2.4 Conclusions

In this work, we have demonstrated a fully ab initio many-body simulation strategy that, starting from the material structure, directly approximates the solution of the electronic Schrödinger equation to obtain the superconducting pairing order across a range of geometries and compositions of cuprate materials. We note what is not yet contained within our current treatment: there are no phonons, or long-range spin or charge fluctuations (at distances much larger than the computational cell) and long wavelength orders, the treatment of doping does not include explicit dopants and the associated structural relaxation and disorder, nor are the solvers and representations numerically exact (for a detailed analysis of outstanding limitations, see Sec. 4 of [135]). Consequently, there remain important differences between the results of the simulations and observations in real materials. Nonetheless, our goal is not to reproduce all aspects of cuprate ground-state physics, but rather to capture some of the observed material trends. In this regard, we find that we reproduce two well-

known systematic trends in the materials: the increase in maximum pairing order as a function of intralayer pressure; and the increase (and decrease) in maximum pairing order as a function of the number of stacked copper-oxygen layers. That these trends correctly appear indicates that the physics and numerical aspects of the calculation likely contain important and relevant ingredients to describe superconducting pairing in a quantitative manner across a range of cuprate materials.

Detailed analysis of our calculations supports some long-standing proposals for the driving force for pairing in cuprates, but also provides new insights. Superexchange, suitably defined, correlates well with maximum pairing order, and short-range spin fluctuations, mainly on the copper atoms, drive the pairing. However, the ab initio picture of the fluctuations is richer than that in simplified models, because multi-orbital effects associated with covalency are needed to facilitate the spin fluctuations. Such multi-orbital processes are key to material-specific trends.

The current work shows that a material-specific understanding of superconductivity in the cuprates is now conceivable through direct ab initio computation. Further, these computations can be systematically improved in the future. Thus our work takes a step towards a material driven understanding of the full phase diagram, the elucidation of the microscopic mechanisms underlying the phases, and the computational search for new high-temperature superconducting materials.

Chapter 3

Ab Initio Many Body Quantum Embedding and Local Correlation in Crystalline Materials using Interpolative Separable Density Fitting

This chapter is based on the following publication:

[1] **Yang, Junjie**, N. Zhang, S. Yuan, J. Yu, H.-Z. Ye, and G. Chan, "Ab Initio Many Body Quantum Embedding and Local Correlation in Crystalline Materials using Interpolative Separable Density Fitting", 10.48550/ARXIV.2601.16379 (2026), pre-published.

3.1 Introduction

Correlated wavefunction methods have attracted increasing attention in computational materials science, because they provide a pathway to controllable accuracy via systematically improvable many-body expansions [136–146]. However, despite their theoretical advantages, these approaches naively suffer from steep computational scaling with system size, which presents an obstacle to obtaining thermodynamic limit (TDL) results [12, 142, 147, 148].

Consequently, several strategies are commonly used to reduce the cost of such calculations. The first exploits the translational symmetry inherent in periodic systems, by utilizing Bloch-type single-particle orbitals labelled by the crystal momentum k. When a uniform k-point mesh of size N_k (containing the Γ point) is employed to sample the Brillouin zone, the calculation is equivalent to one from a periodic supercell containing N_k unit cell images, but with a N_k^{-1} [149] to N_k^{-2} [141] reduction in cost.

The second strategy exploits the locality and decay of correlations [33, 34, 150]. This "near-sightedness" is embodied in different quantum embedding and local correlation frameworks. While there are many variations [35, 37–44, 46–59, 61–69, 151–153], a common feature is that the system is divided into multiple fragments (or clusters), with each fragment subsequently treated independently or with a simplified level of coupling, for example, via the self-consistency of a single-particle quantity in quantum embedding methods [68], or through the simplified treatment of weak pairs in certain local correlation methods. In this work, for concreteness we will focus on density matrix embedding [70, 71] as an example of a quantum embedding method, and the local natural orbital (LNO) method [38, 69] as an example of a local correlation framework. Both have been applied with success to crystalline materials in a diverse range of applications [64–66, 69, 74–77].

The third strategy uses low-rank representations. Low-rank approximations of the Coulomb tensor have been extensively used, such as Cholesky decomposition and resolution-of-the-identity techniques [154–159], pseudospectral approaches [160–162], as well as tensor hypercontraction (THC) [163–166]. Interpolative separable density fitting (ISDF) has attracted attention as a protocol for generating THC-like factorizations in systems under periodic boundary conditions, where it has demonstrated the potential to accelerate multiple

electronic structure methods [167–179].

In this work, we describe an implementation of quantum embedding and local correlation for infinite periodic systems that combines the above reduced-scaling strategies. In particular, our methodology exploits translational symmetry through a tensor hypercontraction representation of the Coulomb interaction, implemented via a symmetry adapted ISDF [180–184] based on crystalline orbitals and utilizing the fast Fourier transform (FFTISDF). The primary algorithmic outcome is the ability to perform many-body quantum embedding and local correlation calculations in materials with only linear scaling with the number of k-points. This enables the practical extraction of thermodynamic limit results.

We organize the rest of the work as follows. Section 3.2 recalls the FFTISDF algorithm for periodic solids utilizing k-point symmetry, and then describes the efficient implementation of the various components of the density matrix embedding and local natural orbital correlation frameworks in this representation and summarizes the parameters used for the benchmark calculations. Section 3.3 provides a set of benchmark studies using coupled cluster theory solvers on representative crystalline systems, including diamond, carbon dioxide, nickel monoxide, and the infinite layer cuprate $CaCuO_2$. These calculations employ Gaussian polarized double-zeta basis sets with up to 1000 k-points to demonstrate the method's scalability, and we extract the thermodynamic limit of the coupled cluster energies for several of the systems. Finally, Section 3.4 summarizes our main findings and discusses potential directions for future work.

3.2 Theory

Our periodic calculations are performed using a crystalline Gaussian-type orbital(GTO) basis,

$$\phi_\mu^{\boldsymbol{k}}(\boldsymbol{r}) = \sum_{\boldsymbol{T}} \mathrm{e}^{\mathrm{i}\boldsymbol{k}\cdot\boldsymbol{T}}\ \tilde{\phi}_\mu(\boldsymbol{r}-\boldsymbol{T}) \tag{3.1}$$

where $\tilde{\phi}_\mu(\boldsymbol{r})$ is a normal GTO centered on an atom in the reference unit cell; $\boldsymbol{T}$ is a lattice translation vector; and $\boldsymbol{k}$ is a momentum vector sampled in the first Brillouin zone. Our implementation builds upon the Gaussian-Plane-Wave infrastructure provided by the PySCF package [185–187], where the basis functions are evaluated on a uniform grid in the unit cell at a set of points $\{\boldsymbol{r}\}$. (This infrastructure is termed FFTDF in PySCF).

Periodic k-point FFTISDF representation of integrals

The core idea of the ISDF approach is to approximate products of basis functions on the grid points $\boldsymbol{r}$ by using values from a select set of interpolating points $\boldsymbol{r}_I$ (IPs). This reduces the computational complexity of evaluating two-electron integrals while maintaining systematic improvability of the approximation. In this work, the interpolation points are selected using a pivoted Cholesky decomposition of $\phi_\mu^{\boldsymbol{k}_\mu}(\boldsymbol{r})\phi_\nu^{\boldsymbol{k}_\nu}(\boldsymbol{r})^*$ (where $\boldsymbol{r}$ is the column index) closely following the procedure outlined in Ref. [188]. Only the largest $N_{\mathrm{IP}} = c_{\mathrm{IP}} \times N_{\mathrm{AO}}$ columns are used, where the pre-defined constant c_{IP} controls the accuracy [189]. This method is suitable for systems with moderate unit cell sizes. Although alternative approaches, such as the centroidal Voronoi tessellation k-means algorithm [168], may be more efficient for large unit cells, they are not the focus of this study. The interpolation points are used to

approximate the product of basis functions on the uniform grid $\{\boldsymbol{r}\}$:

$$\begin{aligned}\rho_{\mu\nu}^{\boldsymbol{k}_\mu \boldsymbol{k}_\nu}(\boldsymbol{r}) &= \phi_\mu^{\boldsymbol{k}_\mu}(\boldsymbol{r})\ \phi_\nu^{\boldsymbol{k}_\nu}(\boldsymbol{r})^* = \phi_\mu^{\boldsymbol{k}_\mu}(\boldsymbol{r})\ \phi_\nu^{-\boldsymbol{k}_\nu}(\boldsymbol{r}) \\ &\approx \sum_I \xi_I^{\boldsymbol{q}}(\boldsymbol{r})\ X_{I\mu}^{\boldsymbol{k}_\mu}\ X_{I\nu}^{-\boldsymbol{k}_\nu}\end{aligned} \tag{3.2}$$

where in the above equation, $X_{I\mu}^{\boldsymbol{k}_\mu} = \phi_\mu^{\boldsymbol{k}_\mu}(\boldsymbol{r}_I)$ is the interpolating vector (IV); $\boldsymbol{q} = \boldsymbol{k}_\mu - \boldsymbol{k}_\nu + \boldsymbol{B}_n$ due to momentum conservation and is shifted to be within the first Brillouin zone ($\boldsymbol{B}_n$ is an integer multiple of the reciprocal lattice vectors); and $\xi_I^{\boldsymbol{q}}(\boldsymbol{r})$ is the interpolation function. The interpolation function is obtained from solving the least-squares problem corresponding to Eq. (3.2), which leads to the following linear equation,

$$\boldsymbol{\Pi}^{\boldsymbol{q}}\ \boldsymbol{\xi}^{\boldsymbol{q}} = \boldsymbol{\eta}^{\boldsymbol{q}} \tag{3.3}$$

where $\boldsymbol{\Pi}^{\boldsymbol{q}}$ is the metric tensor, defined from the product of IVs,

$$\Pi_{IJ}^{\boldsymbol{q}} = \sum_{\boldsymbol{k}} \sum_{\mu\nu} X_{I\mu}^{\boldsymbol{k}-\boldsymbol{q}}\ X_{I\nu}^{-\boldsymbol{k}}\ X_{J\mu}^{\boldsymbol{q}-\boldsymbol{k}}\ X_{J\nu}^{\boldsymbol{k}} \tag{3.4}$$

and which can be efficiently evaluated using the convolution theorem. Similarly, the right-hand side vector is evaluated as

$$\eta_I^{\boldsymbol{q}}(\boldsymbol{r}) = \sum_{\boldsymbol{k}} \sum_{\mu\nu} X_{I\mu}^{\boldsymbol{k}-\boldsymbol{q}}\ X_{I\nu}^{-\boldsymbol{k}}\ \phi_\mu^{\boldsymbol{q}-\boldsymbol{k}}(\boldsymbol{r})\ \phi_\nu^{\boldsymbol{k}}(\boldsymbol{r}) \tag{3.5}$$

The complete algorithm for both the metric tensor and right-hand side vector is outlined in Algorithm 1: when evaluating the metric tensor, $\mathbf{Y}^{\boldsymbol{k}}$ are IVs, where index f represents IPs and index μ corresponds to the AOs, while for the right-hand side vector, $\mathbf{Y}^{\boldsymbol{k}}$ represents AO values evaluated on the uniform grid, with index f now labelling the grid points $\mathbf{r}$.

Algorithm 1 Efficient evaluation of metric tensor and right-hand side vector using convolution theorem.

Input: $X^{\boldsymbol{k}}_{I\mu}$, $Y^{\boldsymbol{k}}_{f\mu}$
Output: $Z^{\boldsymbol{q}}_{If}$
for each $\boldsymbol{k}$ in the Brillouin zone **do**
    $T^{\boldsymbol{k}}_{If} = \sum_{\mu} X^{\boldsymbol{k}}_{I\mu} Y^{-\boldsymbol{k}}_{f\mu}$
end for
$T^{\boldsymbol{R}}_{If} \leftarrow \mathrm{FFT}^{-1}[T^{\boldsymbol{k}}_{If}]$ ▷ transform to the supercell space
$Z^{\boldsymbol{R}}_{If} = T^{\boldsymbol{R}}_{If} \times T^{\boldsymbol{R}}_{If}$ ▷ element-wise multiplication
$Z^{\boldsymbol{q}}_{If} \leftarrow \mathrm{FFT}[Z^{\boldsymbol{R}}_{If}]$ ▷ transform back to the k-space

After solving Eq. (3.3) for the interpolation functions, their Coulomb kernel is defined as

$$W^{\boldsymbol{q}}_{IJ} = \int \mathrm{d}\boldsymbol{r}_1 \mathrm{d}\boldsymbol{r}_2 \, \frac{\xi^{-\boldsymbol{q}}_I(\boldsymbol{r}_1)\, \xi^{\boldsymbol{q}}_J(\boldsymbol{r}_2)}{|\boldsymbol{r}_1 - \boldsymbol{r}_2|} \tag{3.6}$$

which can be efficiently computed by FFT. Since the interpolation functions are themselves not required and only the Coulomb kernel enters into subsequent calculations, we can in fact determine the Coulomb kernel directly. This can be done by first computing $\mathbf{V}^{\boldsymbol{q}}$

$$V^{\boldsymbol{q}}_{IJ} = \int \mathrm{d}\boldsymbol{r}_1 \mathrm{d}\boldsymbol{r}_2 \, \frac{\eta^{-\boldsymbol{q}}_I(\boldsymbol{r}_1)\, \eta^{\boldsymbol{q}}_J(\boldsymbol{r}_2)}{|\boldsymbol{r}_1 - \boldsymbol{r}_2|} \tag{3.7}$$

and then obtaining the Coulomb kernel from solving the least-squares linear equation,

$$\mathbf{\Pi}^{\boldsymbol{q}}\, \mathbf{W}^{\boldsymbol{q}}\, \mathbf{\Pi}^{\boldsymbol{q}} = \mathbf{V}^{\boldsymbol{q}} \tag{3.8}$$

Once the ISDF Coulomb kernel is available, the two-electron integrals in the crystalline basis can be expressed in the THC factorized form,

$$(\mu \boldsymbol{k}_\mu \nu \boldsymbol{k}_\nu | \lambda \boldsymbol{k}_\lambda \sigma \boldsymbol{k}_\sigma) = \sum_{IJ} X^{\boldsymbol{k}_\mu}_{I\mu} X^{-\boldsymbol{k}_\nu}_{I\nu} X^{\boldsymbol{k}_\lambda}_{J\lambda} X^{-\boldsymbol{k}_\sigma}_{J\sigma} W^{\boldsymbol{q}}_{IJ} \tag{3.9}$$

Implementation of quantum embedding and local correlation with FFTISDF

Starting from the two-electron integrals in the form of Eq. (3.9), the various components of quantum embedding and local correlation calculations can be accelerated.

For example, the starting point is typically a periodic Hartree-Fock calculation. The factorized Hamiltonian leads to an efficient evaluation of the exact exchange matrix [180, 181, 184] for the k-point Hartree-Fock (k-HF) theory,

$$\begin{aligned} K^{\boldsymbol{k}}_{\mu\nu} &= \frac{-1}{N_{\mathrm{k}}} \sum_{IJ} \sum_{\boldsymbol{q}} X^{\boldsymbol{k}}_{I\mu} X^{-\boldsymbol{k}}_{J\nu} W^{\boldsymbol{q}}_{IJ} \sum_{\lambda\sigma} X^{\boldsymbol{q}-\boldsymbol{k}}_{I\lambda} P^{\boldsymbol{k}-\boldsymbol{q}}_{\lambda\sigma} X^{\boldsymbol{k}-\boldsymbol{q}}_{J\sigma} \\ &= \frac{-1}{N_{\mathrm{k}}} \sum_{IJ} X^{\boldsymbol{k}}_{I\mu} X^{-\boldsymbol{k}}_{J\nu} \sum_{\boldsymbol{q}} W^{\boldsymbol{q}}_{IJ} \rho^{\boldsymbol{k}-\boldsymbol{q}}_{IJ} \end{aligned} \tag{3.10}$$

which can also be computed as a convolution.

Similarly, in local correlation frameworks it is generally necessary to do a global (i.e. on the whole system) correlation calculation at a low level of theory (e.g. second order perturbation theory or direct random phase approximation), either to determine the virtual correlation space, or to compute a global energy correction [181, 190–193]. The k-point FFTISDF formulation reduces the k-point scaling of such calculations also. In the case of k-point scaled-opposite-spin MP2 (k-SOS-MP2) and the k-point direct random phase approximation (k-dRPA) one can obtain overall linear scaling with the number of k-points [180, 181].

The k-SOS-MP2 correlation energy is defined by multiplying an empirical scaling factor $c_{\mathrm{SOS}} = 1.3$ to the opposite-spin MP2 correlation energy,

$$E^{\text{SOS-MP2}}_{\mathrm{corr}} = c_{\mathrm{SOS}}\, E_{\mathrm{OS}}, \tag{3.11}$$

For an efficient formulation, the opposite-spin contribution can be computed via the imaginary-frequency non-interacting density response function [194]

(the same expression can be derived from the Laplace-transformed energy denominator formula [165, 195]),

$$\begin{aligned} E_{\mathrm{OS}} &= \sum_{\boldsymbol{q}} \int_{-\infty}^{\infty} \frac{\mathrm{d}\omega}{2\pi N_{\mathrm{k}}} \operatorname{tr}\Big[\mathbf{P}^{\boldsymbol{q}}(i\omega)\, \mathbf{P}^{\boldsymbol{q}}(i\omega)\Big] \\ &= \sum_{\boldsymbol{q}} \int_{0}^{\infty} \frac{\mathrm{d}\tau}{N_{\mathrm{k}}} \operatorname{tr}\Big[\mathbf{P}^{\boldsymbol{q}}(\tau)\, \mathbf{P}^{\boldsymbol{q}}(-\tau)\Big] \end{aligned} \tag{3.12}$$

$\mathbf{P}^{\boldsymbol{q}}(\tau)$ can be efficiently evaluated with the convolution theorem, using a similar algorithm as in Algorithm 1,

$$P^{\boldsymbol{q}}_{IJ}(\tau) = \sum_{\boldsymbol{k}} \sum_{K} G^{\boldsymbol{k}}_{IK}(\tau)\; G^{\boldsymbol{q}-\boldsymbol{k}}_{IK}(-\tau)\; W^{\boldsymbol{q}}_{KJ} \tag{3.13}$$

where $G^{\boldsymbol{k}}_{IJ}(\tau)$ is the imaginary-time non-interacting Green's function in the interpolating point representation,

$$G^{\boldsymbol{k}}_{IJ}(\tau) = \sum_{\mu\nu} X^{\boldsymbol{k}}_{I\mu}\; X^{-\boldsymbol{k}}_{J\nu}\; G^{\boldsymbol{k}}_{\mu\nu}(\tau) \tag{3.14}$$

and in the atomic orbital basis, the Green's function is given by ($\tau > 0$),

$$\begin{aligned} G^{\boldsymbol{k}}_{\mu\nu}(+\tau) &= + \sum_{i \in \mathrm{occ}} C^{\boldsymbol{k}}_{\mu i}\; C^{\boldsymbol{k}}_{i\nu} \exp\big(-\tau \epsilon^{\boldsymbol{k}}_{i}\big) \\ G^{\boldsymbol{k}}_{\mu\nu}(-\tau) &= - \sum_{a \in \mathrm{vir}} C^{\boldsymbol{k}}_{\mu a}\; C^{\boldsymbol{k}}_{a\nu} \exp\big(+\tau \epsilon^{\boldsymbol{k}}_{a}\big) \end{aligned} \tag{3.15}$$

$C^{\boldsymbol{k}}_{\mu i}$ and $\epsilon^{\boldsymbol{k}}_{i}$ ($C^{\boldsymbol{k}}_{\mu a}$ and $\epsilon^{\boldsymbol{k}}_{a}$) are the k-point occupied (virtual) coefficients and energies obtained from a k-HF calculation, respectively.

For the k-dRPA, the correlation energy is

$$E^{\mathrm{dRPA}}_{\mathrm{corr}} = \sum_{\boldsymbol{q}} \int_{-\infty}^{\infty} \frac{\mathrm{d}\omega}{2\pi N_{\mathrm{k}}} \Big[\, \ln\det \mathbf{Q}^{\boldsymbol{q}}(\omega) + \operatorname{tr} \mathbf{P}^{\boldsymbol{q}}(\omega)\Big] \tag{3.16}$$

where $\mathbf{Q}^{\boldsymbol{q}}(\omega) = \mathbf{1} - \mathbf{P}^{\boldsymbol{q}}(\omega)$, $\mathbf{1}$ is the identity matrix of dimension $N_{\mathrm{IP}} \times N_{\mathrm{IP}}$. Eq. (3.12) is obtained as the second-order term in the Taylor expansion of the logarithm in Eq. (3.16). The integrals in Eqs. (3.12) and (3.16) can be computed by numerical quadrature. Specifically, in this work we use modified

Gauss-Legendre grids on the imaginary axis and Clenshaw-Curtis grids on the real axis.

A common component in both quantum embedding (such as density matrix embedding) and local natural orbital correlation treatments is the need to construct a fragment Hamiltonian in a subset of orbitals of the full problem. We can use the FFTISDF form of the Hamiltonian to accelerate this construction. A similar formulation was previously proposed in Ref. [181]. For a general description of the fragment Hamiltonians in density matrix embedding and local natural orbital correlation frameworks, we refer the reader to Ref. [64] and Ref. [69].

The fragments are defined in terms of a set of fragment orbitals

$$\phi_p(\boldsymbol{r}) = \frac{1}{\sqrt{N_\mathrm{k}}} \sum_{\boldsymbol{k}} \sum_{\mu} C_{\mu p}^{\boldsymbol{k}} \phi_\mu^{\boldsymbol{k}}(\boldsymbol{r}) \tag{3.17}$$

where the coefficients $C_{\mu p}^{\boldsymbol{k}}$ depend on the particulars of the embedding theory or correlation framework. For example, in density matrix embedding, ϕ_p refers to the impurity and bath orbitals, while in local natural orbital correlation, they constitute the occupied and virtual orbitals of the fragment. What is needed is the Hamiltonian expressed in the space spanned by the fragment orbitals $\{\phi_p(\boldsymbol{r})\}$. The computational bottleneck lies in evaluating the two-body part of this Hamiltonian. One way to obtain the two-body part is to transform from the k-space crystal orbital Hamiltonian to the fragment space,

$$\begin{aligned} V_{pqrs} = \frac{1}{N_\mathrm{k}^2} \sum_{\boldsymbol{k}_\mu \boldsymbol{k}_\nu} \sum_{\mu\nu} \sum_{\boldsymbol{k}_\lambda \boldsymbol{k}_\sigma} \sum_{\lambda\sigma} C_{\mu p}^{\boldsymbol{k}_\mu} C_{\nu q}^{-\boldsymbol{k}_\nu} C_{\lambda r}^{\boldsymbol{k}_\lambda} C_{\sigma s}^{-\boldsymbol{k}_\sigma} \\ \times (\mu \boldsymbol{k}_\mu \nu \boldsymbol{k}_\nu | \lambda \boldsymbol{k}_\lambda \sigma \boldsymbol{k}_\sigma) \end{aligned} \tag{3.18}$$

By employing the FFTISDF formula from Eq. (3.9), this transformation can be expressed in the more computationally efficient form:

$$V_{pqrs} = \sum_{\boldsymbol{q}} \sum_{IJ} R_{I,pq}^{\boldsymbol{q}} \, R_{J,rs}^{-\boldsymbol{q}} \, W_{IJ}^{\boldsymbol{q}} \tag{3.19}$$

where the intermediate tensor is,

$$R^{\boldsymbol{q}}_{I,pq} = \frac{1}{\sqrt{N_{\mathrm{k}}}} \sum_{\boldsymbol{k}} \sum_{\mu\nu} X^{\boldsymbol{k}}_{I\mu}\, X^{\boldsymbol{q}-\boldsymbol{k}}_{I\nu} C^{\boldsymbol{k}}_{\mu p}\, C^{\boldsymbol{q}-\boldsymbol{k}}_{\nu q} \tag{3.20}$$

The convolution theorem can be used to evaluate the intermediate tensor. The procedure is summarized in Algorithm 2. Generating the Hamiltonian with FFTISDF has a cost scaling of $\mathcal{O}(N_{\mathrm{k}} N_{\mathrm{EO}}^2 N_{\mathrm{IP}}^2 + N_{\mathrm{k}} N_{\mathrm{EO}}^4 N_{\mathrm{IP}})$, which is more efficient than the direct evaluation of V_{pqrs} by FFTDF when N_{IP} is much less than the total number of grid points.

Algorithm 2 Pseudocode for computing the two-body part of the embedding Hamiltonian.

Input: $X^{\boldsymbol{k}}_{I\mu}$, $C^{\boldsymbol{k}}_{\mu q}$
Output: $R^{\boldsymbol{q}}_{I,pq}$
for all $\boldsymbol{k}$ **do**
    $T^{\boldsymbol{k}}_{Ip} = \sum_{\mu} X^{\boldsymbol{k}}_{I\mu} C^{\boldsymbol{k}}_{\mu p}$
end for
$T^{\boldsymbol{R}}_{Ip} \leftarrow T^{\boldsymbol{k}}_{Ip}$ ▷ transform to supercell space
$R^{\boldsymbol{R}}_{I,pq} = T^{\boldsymbol{R}}_{Ip} T^{\boldsymbol{R}}_{Iq}$ ▷ outer product
$R^{\boldsymbol{k}}_{I,pq} \leftarrow R^{\boldsymbol{R}}_{I,pq}$ ▷ transform to k-space

Parallelization

The k-point FFTISDF formulation lends itself to parallelization, which we have implemented using MPI. Our approach begins by dividing the real-space grid into optimally sized chunks across available processors, which enables highly efficient parallel evaluation of the right-hand side vector following Eq. (3.5). We note that this domain decomposition significantly reduces the memory requirements per node while maintaining excellent load balancing across computational resources. The Coulomb kernel $\mathbf{W}^{\boldsymbol{q}}$ is then computed in parallel for each k-point using Eqs. (3.7) and (3.8). For the numerical integrations required in k-SOS-MP2 and k-RPA calculations, we also distribute the integration points on the real or imaginary axes.

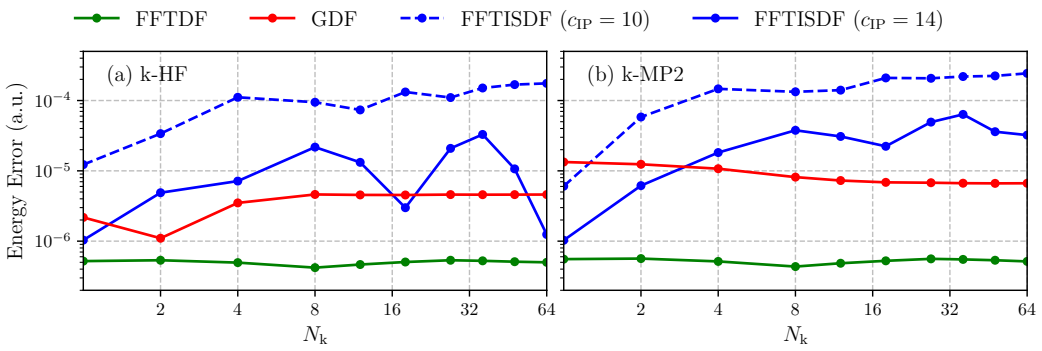

Figure 3.1: Per-atom energy errors for diamond obtained with: FFTDF ($E_{\mathrm{cut}} = 60$ a.u., green), GDF ($\beta = 2.0$, red), and FFTISDF ($E_{\mathrm{cut}} = 60$ a.u., blue). For FFTISDF, results are shown for $c_{\mathrm{IP}} = 10$ (dashed) and $c_{\mathrm{IP}} = 14$ (solid). Errors are computed with respect to a reference FFTDF calculation ($E_{\mathrm{cut}} = 160$ a.u.). Subfigures correspond to (a) k-HF and (b) k-MP2.

Computational Details

We consider four representative solids with different electronic properties and structural characteristics: diamond as an example of a wide-bandgap semiconductor, carbon dioxide (CO_2) as a representative molecular crystal with weak intermolecular interactions, nickel monoxide (NiO) as a correlated transition metal oxide exhibiting Mott insulating behavior, and the infinite-layer $CaCuO_2$ (CCO) as a prototypical cuprate superconductor material with a layered perovskite structure.

All calculations were performed on Intel Icelake 8352Y processors (32-core, 2.2 GHz) with parallelization. For all systems, we employed correlation-consistent GTH-cc-pVDZ Gaussian basis sets [78] and the Goedecker-Teter-Hutter family of pseudopotentials specifically optimized for Hartree-Fock calculations [196–198]. For Brillouin zone sampling, Γ-centered k-point meshes were utilized, and all mean-field calculations were converged to an accuracy of 10^{-6} a.u. per unit cell. To address the integrable divergence of exact exchange, we ap-

plied the leading-order exchange finite-size correction (probe-charge Ewald, `exxdiv=ewald` in PySCF) [185, 199]. For the correlated wavefunction solver, we used coupled cluster singles and doubles (CCSD) as well as with perturbative triples (CCSD(T)) as implemented in PySCF [186, 187]. The DMET calculations were conducted using the interacting bath approach with correlation-potential fitting, but without charge self-consistency (IB w/o CSC in Ref. [64]), utilizing a modified version of the LibDMET package. The LNO-based local correlation calculations were carried out through a module implemented in PySCF-forge [69], utilizing the cluster-specific bath natural orbitals (CBNO) scheme [200].

To establish optimal FFTISDF parameters, we implemented a systematic convergence procedure. Initially, reference Hartree-Fock calculations in the Gaussian-Plane-Wave framework were performed for a series of k-point meshes, progressively increasing the plane-wave cutoff energy E_{cut} until the energy per atom (for all meshes) achieved convergence within a threshold of ϵ_1. Subsequently, this converged E_{cut} value was used as the standard for both FFTDF and FFTISDF calculations. Building upon this, the FFTISDF calculations employ the established E_{cut}, whereas the interpolation point scaling factor c_{IP} was systematically adjusted to maintain accuracy relative to the FFTDF reference within a threshold of ϵ_2 for both k-HF and k-MP2. Additionally, Gaussian density fitting (GDF) was used as an alternative reference method, implemented with even-tempered auxiliary basis sets using an exponent parameter $\beta = 2.0$. Meanwhile, additional parameters specific to the DMET and LNO calculations were established following recommendations from Ref. [64] and Ref. [69].

The optimized parameters for each system are summarized in Table 3.1, with convergence thresholds set to $\epsilon_1 = 10^{-6}$ a.u. per atom and $\epsilon_2 = 10^{-4}$ a.u. per

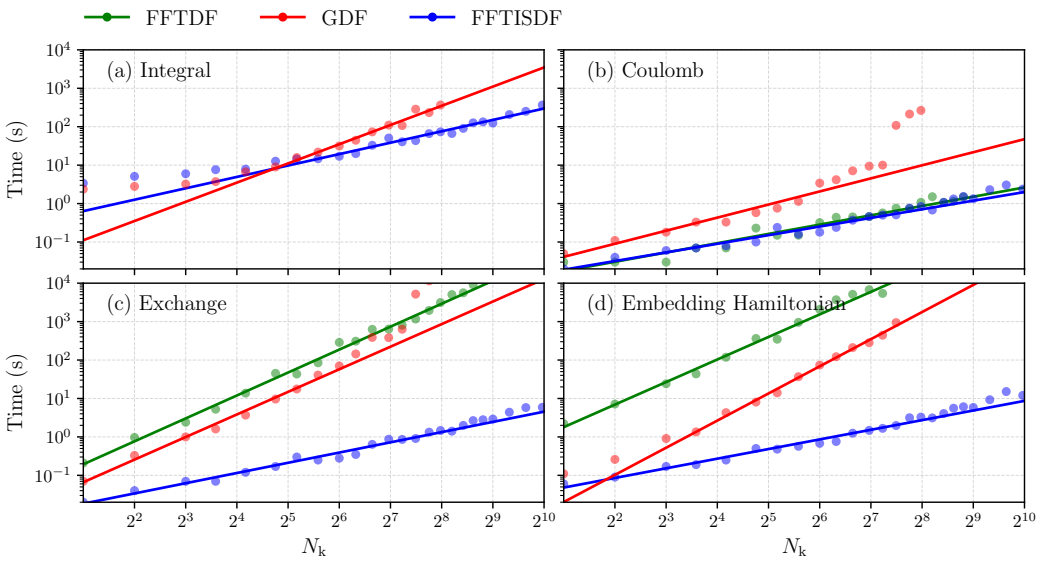

Figure 3.2: Comparison of wall-clock times for different density-fitting schemes applied to the diamond system, plotted against the number of k-points (N_k). Panels show the timing for: (a) integral evaluation, (b) Coulomb matrix construction, (c) exchange matrix construction, and (d) embedding Hamiltonian construction. Solid lines indicate fitted trends highlighting the computational scaling (linear or quadratic) of each method.

atom.

Table 3.1: Number of atoms, number of atomic orbitals and chosen computational parameters for the GTH-cc-pVDZ basis.

System	N_{atom}	N_{AO}	E_{cut} (a.u.)	c_{IP}
Diamond	2	26	60.0	14.0
CO_2	12	156	140.0	14.0
NiO (AFM cell)	4	78	180.0	25.0
CCO (2×2 cell)	16	308	180.0	25.0

Table 3.2: Convergence of ground state and correlation energies (in a.u. per atom) for diamond with respect to k-point sampling. The second column reports the k-HF energy, while columns 3–8 present correlation energies obtained from DMET (with CCSD solver), k-SOS-MP2, k-dRPA, LNO-MP2, LNO-CCSD, and LNO-CCSD(T). The LNO-based methods are extrapolated to the full correlation domain using k-SOS-MP2 as a baseline. The bottom row shows values extrapolated to TDL.

	E (a.u.)	E_{corr} (a.u.)					
N_{k}	k-HF	DMET	k-SOS-MP2	k-dRPA	LNO-MP2	LNO-CCSD	LNO-CCSD(T)
$2 \times 2 \times 2$	-5.4786	-0.0814	-0.1112	-0.1269	-0.1174	-0.1237	-0.1292
$3 \times 3 \times 3$	-5.5111	-0.0897	-0.1169	-0.1321	-0.1257	-0.1316	-0.1364
$4 \times 4 \times 4$	-5.5144	-0.0938	-0.1196	-0.1342	-0.1299	-0.1343	-0.1395
$5 \times 5 \times 5$	-5.5142	-0.0960	-0.1208	-0.1351	-0.1316	-0.1355	-0.1408
$6 \times 6 \times 6$	-5.5137	-0.0975	-0.1213	-0.1355	-0.1323	-0.1361	-0.1414
$7 \times 7 \times 7$	-5.5134	-0.0984	-0.1216	-0.1357	-0.1326	-0.1363	-0.1416
$8 \times 8 \times 8$	-5.5131	-0.0992	-0.1217	-0.1358	-0.1328	-0.1364	-0.1418
$10 \times 10 \times 10$	-5.5129	-0.1002	-0.1218	-0.1359	—	—	—
TDL	-5.5127	-0.1010	-0.1219	-0.1361	-0.1331	-0.1367	-0.1421

3.3 Results and Discussion

Diamond

We begin by assessing the accuracy and efficiency of FFTISDF using the diamond crystal as a benchmark. To ensure a rigorous comparison, we evaluated the ground-state energies (at both k-HF and k-MP2 levels) and the wall times for each computational step against established density fitting schemes (FFTDF and Gaussian Density Fitting (GDF)). This consistent setup allows for a direct evaluation of performance across all methods. To avoid Laplace-transform integration grid errors, the k-MP2 calculations with FFTISDF were obtained here from the exact MP2 expression using the FFTISDF two-electron integrals. The per-atom energy deviations are summarized in Fig. 3.1, utilizing FFTDF with $E_{\mathrm{cut}} = 160$ a.u. as the reference. For FFTDF ($E_{\mathrm{cut}} = 60$ a.u.), the error remains small ($< 10^{-6}$ a.u. per atom), confirming the cutoff's sufficiency. Similarly, GDF yields consistent errors of approximately 10^{-5} a.u. per atom, independent of the mesh size.

The FFTISDF accuracy clearly depends on both c_{IP} and the number of k-points. With $c_{\mathrm{IP}} = 10$, the error increases initially but approaches an asymptotic limit of approximately 10^{-3} a.u. for $N_{\mathrm{k}} > 8$. The accuracy is systematically improved by increasing the interpolation point scaling factor. When $c_{\mathrm{IP}} = 14$, the per-atom error is systematically reduced to below 10^{-4} a.u.. Consequently, we employ $E_{\mathrm{cut}} = 60$ a.u. and $c_{\mathrm{IP}} = 14$ (as detailed in Table 3.1) for all subsequent calculations.

Next, we evaluate the computational efficiency by analyzing the wall times required for computing integrals, Coulomb matrices, exchange matrices, and the fragment Hamiltonian. The results are plotted against the number of k-points in Fig. 3.2, with solid lines indicating the scaling behavior. As shown in Fig. 3.2(a), the integral calculation time for GDF shifts from linear to quadratic scaling as N_{k} increases. This change occurs as the computational bottleneck moves from the Cholesky decomposition of 2c2e integrals to the evaluation of 3c2e integrals. In contrast, FFTISDF maintains strict linear scaling across the entire range. While GDF is slightly faster at small N_{k} (below 2^5), FFTISDF outperforms it significantly as the system size grows. Note that FFTDF is excluded from this comparison as it avoids the computation of intermediate integrals.

For the Coulomb matrix evaluation [Fig. 3.2(b)], while all schemes scale linearly, GDF incurs a notably higher computational cost compared to FFTDF and FFTISDF. For exchange matrices [Fig. 3.2(c)], despite avoiding intermediate integral computations, FFTDF exhibits quadratic scaling and remains the most computationally expensive method. GDF also displays quadratic scaling, whereas FFTISDF is the only method that preserves linear scaling, demonstrating superior efficiency. This advantage extends to the construction of the fragment Hamiltonian [Fig. 3.2(d)]. As FFTDF and GDF scale quadratically,

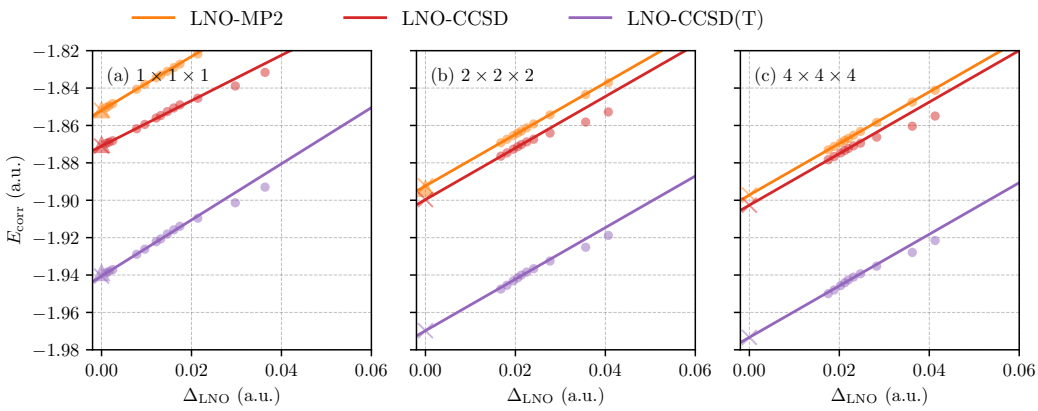

Figure 3.3: Extrapolation of CO_2 correlation energies. LNO-MP2, LNO-CCSD, and LNO-CCSD(T) correlation energies plotted against Δ_{LNO} (the difference between k-SOS-MP2 and LNO-SOS-MP2 correlation energies) for k-point meshes: (a) $1 \times 1 \times 1$ (Γ-point only), (b) $2 \times 2 \times 2$, and (c) $4 \times 4 \times 4$. Small circles represent LNO correlation energies, triangles show global k-point counterparts, crosses mark extrapolated values, and solid lines are fitted lines.

they rapidly become computationally prohibitive. In contrast, FFTISDF preserves linear scaling, offering a speedup of several orders of magnitude at large N_{k} and enabling efficient quantum embedding and local correlation calculations for up to 1000 k-points.

Beyond computational time, FFTISDF also offers superior storage efficiency to GDF, scaling as $N_k N_{\mathrm{IP}}^2 + N_k N_{\mathrm{IP}} N_{\mathrm{AO}}$, in contrast to $N_k^2 N_{\mathrm{AO}}^2 N_{\mathrm{aux}}$ for GDF. This improvement results in a significant reduction in storage requirements, from 881.09 GB to 2.11 GB in the 1000 k-point diamond case.

We next extrapolate the FFTISDF results to the thermodynamic limit. Table 3.2 presents the per-atom k-HF energies and correlation energies from DMET, k-SOS-MP2, LNO-MP2, k-dRPA, LNO-CCSD, and LNO-CCSD(T) calculated for a series of cubic k-point meshes. To reduce the computational cost of LNO calculations for large correlation domains, we used k-SOS-MP2 energies to extrapolate the LNO-CCSD and LNO-CCSD(T) energies (details

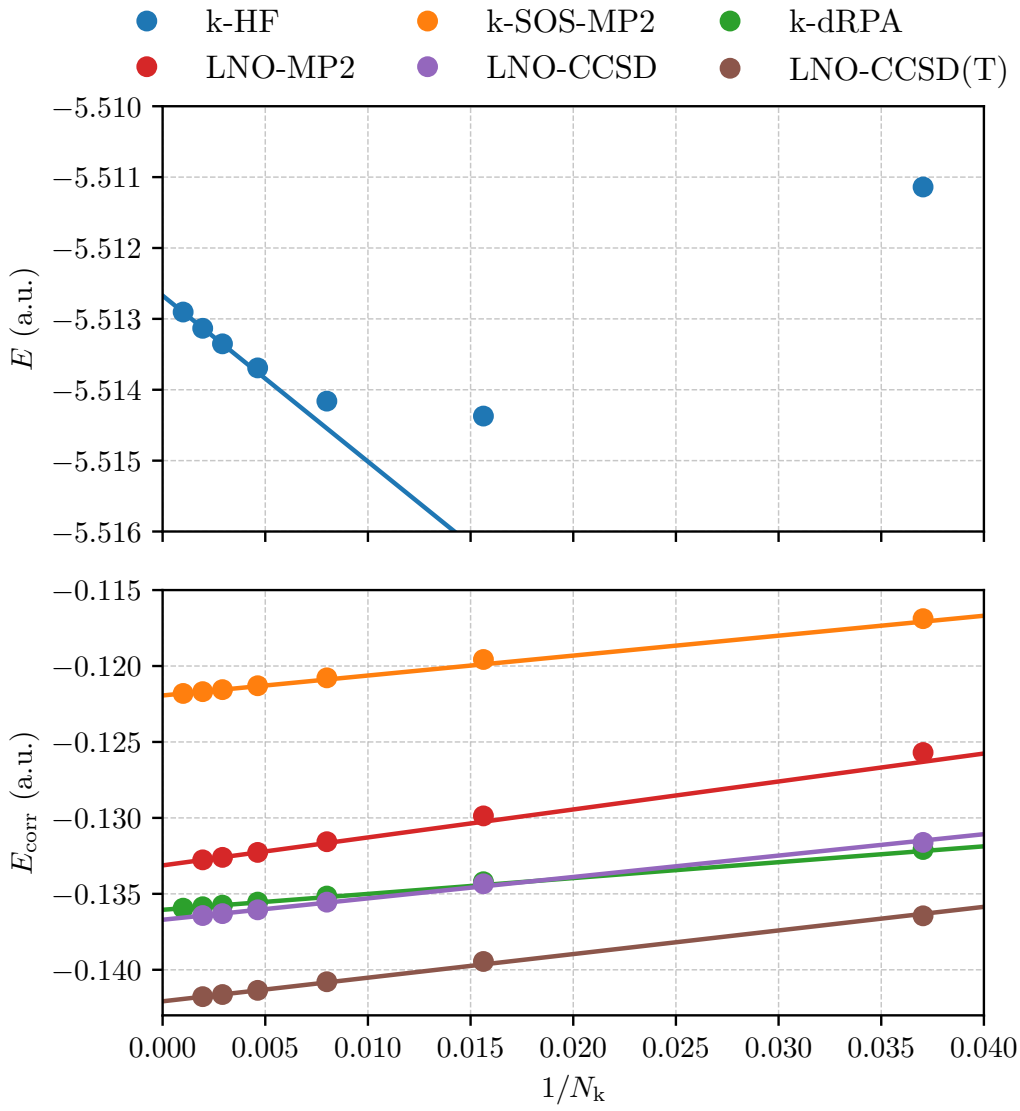

Figure 3.4: Thermodynamic limit extrapolation for diamond. Upper panel: k-HF total energy as a function of $1/N_{\mathrm{k}}$. Lower panel: correlation energies from various methods including k-SOS-MP2, LNO-MP2, k-dRPA, LNO-CCSD, and LNO-CCSD(T). Solid lines represent linear fits used for extrapolation to the thermodynamic limit ($1/N_{\mathrm{k}} \to 0$).

provided in the following subsection). The thermodynamic limit is then obtained by performing a linear fit against N_{k}^{-1} using data from the four largest k-point meshes, as the Ewald exchange divergence correction ensures $\mathcal{O}(N_{\mathrm{k}}^{-1})$ convergence behavior. The extrapolation is visualized in Fig. 3.4.

Notably, as more k-points are systematically incorporated, the k-HF energy initially decreases and then gradually increases before finally approaching the TDL value. While previously reported [201], this energy-increasing regime remains prohibitive to sample adequately using existing methods (FFTDF and GDF) due to their steep scaling. Consequently, TDL extrapolations based on such truncated data are inherently less reliable. For correlated methods, DMET substantially underestimates the correlation energy as a result of its restricted embedding space size, whereas the other correlated approaches yield more consistent values. Finally, the efficiency of FFTISDF makes it possible to extrapolate to reliable CCSD(T) energies at the thermodynamic limit for diamond.

Carbon dioxide

We select the carbon dioxide system as a representative molecular crystal, and to demonstrate the extrapolation procedure to the complete correlation domain. Initially, k-HF calculations were performed using the exchange matrix defined by Eq. (3.10). Subsequently, the k-SOS-MP2 correlation energy was evaluated using Eq. (3.11), establishing the reference point for the extrapolation.

Following this, LNO computations were performed across a range of truncation thresholds to obtain SOS-MP2, MP2, CCSD, and CCSD(T) correlation energies for each domain size. The difference between k-SOS-MP2 and LNO-SOS-MP2 correlation energies is denoted as Δ_{LNO}. The MP2, CCSD, and CCSD(T) energies from the four largest correlation domains were then linearly fitted as functions of the corresponding Δ_{LNO} values.

Finally, by extrapolating to $\Delta_{\mathrm{LNO}} = 0$ (corresponding to the complete k-SOS-

MP2 limit), the global MP2, CCSD, and CCSD(T) correlation energies were obtained. This framework enables efficient evaluation of global correlation energies without incurring the prohibitive computational costs associated with direct large-scale calculations.

To validate the accuracy of our extrapolation procedure, we analyze the relationship between the LNO-SOS-MP2 correlation energies and their LNO-MP2, LNO-CCSD, and LNO-CCSD(T) counterparts across varying correlation domain sizes. Fig. 3.3(a) illustrates the results for a $1 \times 1 \times 1$ k-point mesh (Γ-point), where the small circles denote the LNO energies and triangles represent the corresponding global k-point reference values. As expected, as the correlation domain expands, all LNO correlation energies (circles) systematically converge toward their global counterparts (triangles), confirming the correct asymptotic behavior. Based on this trend, we performed the extrapolation, with both the fitted lines and the resulting extrapolated values (crosses) displayed in the figure. The LNO-MP2 data points exhibit near-perfect linear alignment, resulting in exceptional agreement between the extrapolated value ($E_{\text{corr}}^{\text{LNO-MP2}} = -1.8519$ a.u.) and the global reference ($E_{\text{corr}}^{\text{k-MP2}} = -1.8517$ a.u.). The corresponding per-atom error is $\sim 1 \times 10^{-5}$ a.u.

The CCSD and CCSD(T) data show slight deviations from the fitted line for the small domains. This leads to minor differences between the extrapolated values ($E_{\text{corr}}^{\text{LNO-CCSD}} = -1.8710$ a.u.; $E_{\text{corr}}^{\text{LNO-CCSD(T)}} = -1.9405$ a.u.) and their global references ($E_{\text{corr}}^{\text{k-CCSD}} = -1.8703$ a.u.; $E_{\text{corr}}^{\text{k-CCSD(T)}} = -1.9398$ a.u.). Nevertheless, these errors remain remarkably small, with per-atom errors of $\sim 6 \times 10^{-5}$ a.u. in both cases.

We subsequently extended the extrapolation procedure to larger k-point meshes, specifically the $2\times2\times2$ and $4\times4\times4$ configurations, as illustrated in Fig. 3.3(b)

and (c). Although reference data is limited to k-MP2 for the $2 \times 2 \times 2$ mesh and is unavailable for other cases due to prohibitive computational costs, the overall trends remain consistent with those observed at the Γ-point. Notably, we observe a substantial gap between the LNO-SOS-MP2 energy (using the largest affordable domain) and the exact global k-SOS-MP2 reference. At the $2 \times 2 \times 2$ mesh, this deviation amounts to $\sim 1 \times 10^{-3}$ a.u. per atom ($E_{\text{corr}}^{\text{k-SOS-MP2}} = -1.7750$ a.u. and $E_{\text{corr}}^{\text{LNO-SOS-MP2}} = -1.7582$ a.u.). A similar discrepancy is found in the MP2 correlation energy ($\sim 2 \times 10^{-3}$ a.u. per atom; $E_{\text{corr}}^{\text{k-MP2}} = -1.8956$ a.u. and $E_{\text{corr}}^{\text{LNO-MP2}} = -1.8707$ a.u.). However, the extrapolation reduces the error to $\sim 1 \times 10^{-4}$ a.u. per atom. This result highlights the insufficiency of the computationally accessible truncated domains and establishes the effectiveness of our extrapolation strategy. Although global correlated benchmarks are unavailable for the larger k-point meshes, the LNO-based methods continue to exhibit excellent linearity. Consequently, we anticipate high reliability for the extrapolated values derived from these linear extrapolations.

Table 3.3: Extrapolated TDL energies for HF, MP2, CCSD, and CCSD(T) for CO_2.

Method	E_{corr} (a.u.)	E (a.u.)
HF	—	-148.0545
MP2	-1.8979	-149.9524
CCSD	-1.9030	-149.9574
CCSD(T)	-1.9748	-150.0293

Based on the validation of the LNO-extrapolation procedure, we further proceeded to obtain the total energies in the TDL by employing multiple k-point meshes. The final values are summarized in Table 3.3.

Table 3.4: Ground-state energies (in a.u.) and Heisenberg exchange constants J (in meV) for NiO and CCO in the AFM and FM states, calculated using k-HF and DMET (CCSD solver) with various k-point meshes. The thermodynamic limit (TDL) is obtained by extrapolating the k-HF energies and DMET correlation energies separately using a linear fit against N_{k}^{-1} with the three largest k-point grids. J represents the next-nearest-neighbor exchange constant J_2 for NiO and the nearest-neighbor exchange constant J_1 for CCO.

	E_{AFM} (a.u.)		E_{FM} (a.u.)		J (meV)	
N_{k}	k-HF	DMET	k-HF	DMET	k-HF	DMET
NiO						
$2 \times 2 \times 2$	-366.7825	-367.3968	-366.7794	-367.3918	-14.10	-22.88
$3 \times 3 \times 3$	-366.7687	-367.3778	-366.7669	-367.3744	-8.12	-15.75
$4 \times 4 \times 4$	-366.7622	-367.3766	-366.7605	-367.3734	-7.69	-14.75
$5 \times 5 \times 5$	-366.7593	-367.3770	-366.7576	-367.3738	-7.63	-14.09
$6 \times 6 \times 6$	-366.7580	-367.3785	-366.7563	-367.3753	-7.63	-14.43
TDL	-366.7562	-367.3787	-366.7545	-367.3756	-7.59	-14.05
CCO						
$2 \times 2 \times 1$	-1055.4085	-1056.5605	-1055.4012	-1056.5342	-50.02	-178.69
$4 \times 4 \times 2$	-1053.5604	-1054.5908	-1053.5545	-1054.5663	-40.35	-167.10
$6 \times 6 \times 4$	-1050.5774	-1051.6032	-1050.5715	-1051.5783	-40.66	-169.14
TDL	-1053.2964	-1054.3095	-1053.2907	-1054.2851	-38.97	-165.44

Nickel monoxide and cuprate

We apply the FFTISDF-DMET framework with a CCSD solver to two prototypical strongly correlated transition metal oxides: NiO and $CaCuO_2$ (CCO). Our analysis focuses on the energy difference between antiferromagnetic (AFM) and ferromagnetic (FM) orderings. Notably, the implementation of such large k-point meshes is made feasible specifically by the FFTISDF algorithm. This allows us to systematically study long-range correlation effects that are critical for accurately determining the magnetic energy gaps in the strongly correlated regime.

When NiO is cooled below its Néel temperature, it adopts an AFM phase characterized by staggered magnetization along the [111] direction, commonly known as the AFM-II phase. By mapping the energy difference between the AFM and FM states to a spin Hamiltonian, one can derive the nearest-neighbor

J_1 and next-nearest-neighbor J_2 exchange constants [202]. Since experimental and theoretical evidence indicates that J_1 is negligible in NiO [203], we neglect its contribution and focus exclusively on computing J_2, the dominant exchange interaction, from the difference in the FM and AFM energies.

Table 3.4 presents the ground-state energies obtained from k-HF and DMET calculations across various k-point meshes, using spin-polarized initial guesses. To approach the thermodynamic limit, we extrapolated the k-HF energies and DMET correlation energies separately by performing a linear fit against N_{k}^{-1} using data from the three largest k-point meshes. The extrapolation reveals distinct behaviors between the two methods. While k-HF systematically underestimates J_2, DMET yields a value of -14.05 meV, slightly underestimating the magnitude compared to the experimental range of -19.8 to -17.0 meV [204]. This improvement over k-HF demonstrates the importance of incorporating correlation effects in describing the magnetic interactions of NiO.

Turning to CCO, the defining structural feature of this cuprate compound is the two-dimensional CuO_2 square lattice plane (formally $[CuO_2]^{2-}$). While these planes are typically separated by buffer layers in various high-T_c families, we focus here on the infinite-layer calcium cuprate $CaCuO_2$. Due to the layered structure, we employ anisotropic k-point meshes with fewer points along the c-axis. The correlation effects in CCO are even more pronounced than in NiO. At the thermodynamic limit, DMET yields $J = -165.44$ meV, more than four times larger in magnitude than the k-HF value of -38.97 meV. This DMET result is in good agreement with experimental values of -142 and -158 meV obtained by fitting the spin-wave dispersion near the Γ point [205, 206].

3.4 Conclusion

We have described an implementation of interpolative separable density fitting in the Gaussian-Plane-Wave framework (FFTISDF in PySCF) and its integration with quantum embedding and local correlation frameworks. This implementation establishes a robust computational framework capable of obtaining converged ground-state energies from DMET and LNO-based MP2, CCSD, and CCSD(T) calculations for crystals with simple unit cells in the thermodynamic limit. While this efficient methodology opens new avenues for high-level correlated calculations in extended systems, several aspects of the proposed approach still warrant further improvement.

First, the current implementation requires a relatively large number of interpolation points, typically ten times the number of atomic orbitals (see Table 3.1), to reach our desired accuracy. As a result, the determination of these interpolation points becomes computationally demanding, particularly for systems with large unit cells. Developing efficient protocols for generating compact interpolation points would therefore be highly desirable.

Second, the size of the real-space grid employed in the fast Fourier transforms remains large. This is a challenge for systems containing transition metals or those with large unit cells.

Finally, in this work, LNO-based approaches employed the CBNO scheme [200] for constructing correlation domains, although this method does not exhibit an optimal convergence with respect to the domain size [69]. Exploring alternative correlating spaces is of interest. Furthermore, the developed embedding framework can be readily extended to other quantum embedding approaches, such as dynamical mean field theory [59, 67].

Chapter 4

Benchmarking the Exponential Ansatz for the Holstein Model

This chapter is based on the following publication:

[1] **Yang, Junjie**, Z.-H. Cui, A. Mahajan, H. Zhai, D. R. Reichman, and G. K.-L. Chan, "Benchmarking the exponential ansatz for the Holstein model", The Journal of Chemical Physics **161**, 104105 (2024),

4.1 Introduction

Electron-phonon interactions constitute a fundamental mechanism governing the physical properties of numerous solid-state materials [207]. Most notably, these interactions underpin the Bardeen-Cooper-Schrieffer (BCS) theory of superconductivity, wherein the electron-phonon coupling mediates an effective attraction between electrons, thereby enabling Cooper pair formation [208, 209]. Beyond superconductivity, electron-phonon interactions significantly influence charge transport in a broad class of semiconductors [210–215], organic molecular crystals and polymers [216, 217], as well as biological molecular aggregates that participate in photosynthetic energy transfer [218–220].

When the electron-phonon coupling becomes sufficiently strong, electrons become trapped by localized lattice distortions, forming quasiparticles known as

polarons [221]. Recent investigations have revealed polaron-like lattice distortions in a variety of novel materials exhibiting extraordinary properties. Prominent examples include non-metallic nickelates [222], colossal magnetoresistance manganites [223], and, most significantly, high-T_c superconducting cuprates [224–227]. These discoveries have stimulated renewed theoretical interest in understanding polaron physics from first principles.

Polaron phenomenology has been extensively investigated through lattice models and semi-empirical Hamiltonians, among which the Holstein model [228] represents the simplest yet most instructive example. The Holstein model captures both polaron formation and the crossover between the small and large polaron regimes within a unified framework. This model is particularly applicable to systems exhibiting effective screening, such as multiband metals where a narrow band enables strong coupling to phonons, transition-metal oxides, and organic metals containing molecular units that provide local phonon modes strongly interacting with electronic orbitals. Despite its apparent simplicity, analytical treatments of the Holstein model remain tractable only under restricted conditions [229]. Specifically, for the one-electron Holstein model, analytical solutions exist in the strong-coupling adiabatic limit via the Holstein transformation [228] and in the anti-adiabatic limit via the Lang-Firsov transformation [212, 230]. In contrast, no well-controlled analytical method exists for the intermediate coupling regime.

Consequently, numerical approaches have become indispensable for exploring the one-electron Holstein model across all coupling strengths. Established methods include exact diagonalization (ED) [231, 232], density matrix renormalization group (DMRG) [233], quantum Monte Carlo (QMC) [234–239], variational wavefunctions [240–244], dynamical mean-field theory (DMFT) [245, 246], density matrix embedding theory (DMET) [247, 248], perturbation the-

ories [228, 230, 249–251], and canonical transformation formalisms [252–254]. Collectively, these studies demonstrate that the sharp transition in ground state energy near the intermediate coupling regime, which corresponds to physically interesting and realistic situations, poses a significant challenge for most computational methods [251]. This observation motivates the development and systematic benchmarking of new theoretical approaches capable of accurately describing the polaronic crossover.

The present work investigates and benchmarks the exponential electron-phonon ansatz for the single-electron Holstein model. We consider two specific classes of exponential ansatz. The first is coupled cluster theory, which is widely recognized as one of the most accurate methods in computational chemistry [255–260]. Here we employ the electron-phonon coupled cluster formalism introduced by some of us in Ref. [261]. The second is the variational Lang-Firsov ansatz together with its recently developed perturbation theory, as discussed in Ref. [262], also by some authors of this work. Because the variational Lang-Firsov ansatz [230] can be interpreted as a unitary coupled cluster theory, it naturally belongs to the family of exponential ansatz wavefunctions. We systematically evaluate the numerical performance of these methods across different parameter regimes of the model, benchmarking against converged exact results obtained from density matrix renormalization group simulations [233, 263, 264]. In addition to the ground state energy, we examine multiple observables that characterize polaron formation and the transition between large and small polarons.

Coupled cluster theory has established itself as a cornerstone method for computing molecular properties with high accuracy [255–260]. Furthermore, its application has been extended to periodic systems [265–270] and to vibrational problems involving non-adiabatic effects [261, 271–280]. Recently, an

electron-phonon coupled cluster framework was proposed and evaluated for the Hubbard-Holstein model, molecules, and *ab initio* crystal settings [281]. Although this scheme achieved high accuracy in the weak to moderate electron-phonon coupling regimes, it exhibited significant errors in the strong coupling regime, particularly when delocalized reference states were employed. Unlike previous approaches, this work aims to carefully benchmark the accuracy of a series of advanced quantum many-body methods for the Holstein model, with particular emphasis on the polaronic region where existing methods encounter difficulties.

This work is organized as follows. In Section 4.2, we present the setup of the Holstein model. Subsequently, in Section 4.2, we formulate the coupled cluster methods for electron-phonon systems. The LF-HF and LF-MP methods are introduced in Section 4.2. Results for the ground state energy, kinetic energy, and electron-lattice correlation function are reported in Section 4.5, followed by concluding remarks in Section 4.6.

4.2 Theory

Holstein Model

The single-electron Holstein model defines a minimal spinless one-electron lattice model containing interactions between a single electron band and a set of local phonons. The Hamiltonian for a L-site one-dimensional Holstein model is

$$\begin{aligned} H = &- t \sum_{\langle lk \rangle} \left(a_l^\dagger a_k + a_k^\dagger a_l \right) + \omega \sum_l b_l^\dagger b_l \\ &+ g \sum_l \rho_l \left(b_l^\dagger + b_l \right) \end{aligned} \tag{4.1}$$

where $a_l^\dagger$ (a_l) creates (annihilates) an electron on site l, and $b_l^\dagger$ (b_l) creates (annihilates) a phonon of frequency ω on site l, $\rho_l = a_l^\dagger a_l$ is the electron

number operator on site l, and periodic boundary conditions are assumed. The electron-phonon coupling parameter is denoted as g, and we set the hopping parameter t to be 1 (thus all energy values will implicitly be in units of t).

The physics of the Holstein model can be understood in different limiting cases. Defining the adiabaticity parameter as ω, $\omega \ll t$ corresponds to a slow response of the lattice distortion to electron hopping. In this scenario, the Born-Oppenheimer approximation is valid and the electronic motion is consequently modified by quasi-static lattice deformations (i.e. an adiabatic potential surface). Alternatively, when $\omega \gg t$ (the anti-adiabatic limit), the lattice deformation adapts instantaneously to the electron's position. Then, only the vibrational ground state is involved in low-energy electron hopping processes.

Another axis along which to understand the physics is with respect to the electron-phonon coupling g itself. In the weak coupling regime, defined by $g/\omega \ll 1$ and $g^2/\omega \ll 2t$, the system resembles a quasi-free electron dragging a phonon cloud: this is known as a large polaron. In contrast, in the strong coupling regime, the electronic position is closely correlated with the lattice distortion it generates: this is known as a small polaron, which is referred to as self-trapped. Although some early analytical perturbation theory suggested a sharp transition between the two [250, 282], it has been established from rigorous analysis that there is a smooth crossover between the small and large polaron limits [229]. The accurate description of the self-trapping crossover represents a challenge for most computational methods [251].

The exact ground-state of the Holstein model can be expressed as

$$|\Psi_0\rangle = \sum_I C_I |\Phi_I\rangle \tag{4.2}$$

where $|\Phi_I\rangle$ is a configuration of the electron-phonon system,

$$|\Phi_I\rangle = |\sigma_1^I n_1^I\rangle \otimes |\sigma_2^I n_2^I\rangle \otimes \cdots \otimes |\sigma_L^I n_L^I\rangle \tag{4.3}$$

with σ_l^I an electronic state on site l, which can be either empty or singly occupied, and n_l^I is the phonon occupation state on site l, which is a number between 0 and N where N is the maximum local phonon number. The number of configurations in the above is $L \times (N+1)^L$, and N should be taken to infinity for converged results. The rapid growth in the number of configurations with both N and L limits the usefulness of exact diagonalization (ED) and motivates the study of approximate ansatzes. We focus on two variants of the exponential ansatz for the ground-state: the coupled cluster method and the Lang-Firsov transformation. For benchmarking purposes, we employ the density matrix renormalization group (DMRG), which provides highly accurate results for finite N, but where N must be extrapolated: this is described in Appendix 4.3.

Reference states

The coupled cluster and Lang-Firsov methods require a starting reference state. We will assume the reference state to be a product state of a single-particle electronic orbital and a site-dependent coherent state,

$$\begin{aligned} |\Phi_0\rangle &= |\Phi_0^{\mathrm{F}}\rangle \otimes |\Phi_0^{\mathrm{B}}\rangle \\ |\Phi_0^{\mathrm{F}}\rangle &= \sum_l A_l a_l^\dagger |0^{\mathrm{F}}\rangle \\ |\Phi_0^{\mathrm{B}}\rangle &= \exp\left[\sum_l \xi_l b_l^\dagger - \xi_l^* b_l\right] |0^{\mathrm{B}}\rangle \end{aligned} \tag{4.4}$$

where $|0^{\mathrm{F}}\rangle$ and $|0^{\mathrm{B}}\rangle$ are the physical vacua for electrons and phonons respectively.

In the simplest case, which we refer to as the mean-field (MF) reference state, A_l and ξ_l are chosen to minimize the energy $\langle\Phi_0|H|\Phi_0\rangle/\langle\Phi_0|\Phi_0\rangle$, with

$\xi_l = g\langle\rho_l\rangle/\omega$ and $\langle\rho_l\rangle = A_l^* A_l$. ξ_l represents the equilibrium shift of the phonon mode at site l induced by the electron density. The optimal A_l either satisfies translational invariance (delocalized) or it breaks translational invariance (localized). These two solutions, $|\Phi_0^{(\mathrm{D})}\rangle$, $|\Phi_0^{(\mathrm{L})}\rangle$ respectively, are favoured in different regimes of the Holstein model parameter space, and can be viewed as a mean-field description of the self-trapping crossover. However, it is known that the mean-field description is not accurate in this region, and an important test of the more sophisticated exponential ansatzes we explore on top of these mean-field reference states is to see how well they improve the description of the crossover.

An alternative is to reoptimize and improve $\mathbf{A}$ and $\boldsymbol{\xi}$ in the presence of the exponential ansatz parameters. We discuss this option below.

Coupled Cluster Models for Electron-phonon Systems

model	T_e	T_p	T_ep	scaling
CCS-1-S1	$t_{ai}a_a^\dagger a_i$	$t_l b_l^\dagger$	$t_{l,ai}b_l^\dagger a_a^\dagger a_i$	L^3
CCS-2-S2	$t_{ai}a_a^\dagger a_i$	$t_l b_l^\dagger + \frac{1}{2!}t_{lk}b_l^\dagger b_k^\dagger$	$t_{l,ai}b_l^\dagger a_a^\dagger a_i + \frac{1}{2!}t_{lk,ai}b_l^\dagger b_k^\dagger a_a^\dagger a_i$	L^4
LF-HF	0	0	$\lambda_l a_l^\dagger a_l (b_l^\dagger - b_l)$	L^3

Table 4.1: The exponential ansatzes employed in this study; the wavefunctions are of the form $e^{T_\mathrm{ep}}e^{T_\mathrm{e}}e^{T_\mathrm{p}}|\Phi_0\rangle$, where $|\Phi_0\rangle$ is the mean-field electron-phonon reference state. Computational scaling is described as a function of the number of sites L. Summation symbols are omitted for brevity.

The coupled cluster method for electron-phonon systems is formulated based on the exponential wavefunction ansatz [281],

$$|\Psi_\mathrm{CC}\rangle = \exp(T_\mathrm{CC})\,|\Phi_0\rangle \tag{4.5}$$

where the excitation operator T_CC consists of an electronic part, a phononic

part, and a coupling:

$$\begin{aligned} T_{\mathrm{CC}} &= T_{\mathrm{e}} + T_{\mathrm{p}} + T_{\mathrm{ep}} = \sum_{\mu} t_{\mu}\tau_{\mu} \\ \tau_{\mu} &\in \{a_a^\dagger a_i, b_l^\dagger, b_l^\dagger a_a^\dagger a_i \cdots\} \end{aligned} \tag{4.6}$$

where i, a are occupied and virtual electronic orbital indices, and l, k, m, n are used for site indices for the boson operators. The truncation of the excitation operator determines the accuracy and cost scaling of the method. Given the one-electron nature of the Holstein model, there is only a single occupied electronic orbital (i.e. a single index value for i, with the form of the orbital specified by $\mathbf{A}$ in Eq 4.4), and the electronic excitations are captured exactly using singles excitations of the form $a_a^\dagger a_i$, thus we truncate the electronic excitation to this level, referred to as singles. The order of the phonon and coupling excitations is then denoted by X-SY, where X, Y are numbers that show the excitation order. For example, CCS-1-S1 indicates single electronic excitations, single phonon excitations, and single coupled excitations, corresponding to the excitation operator $\sum_{ia} t_{ai} a_a^\dagger a_i + \sum_l t_l b_l^\dagger + \sum_{l,ai} t_{l,ai} b_l^\dagger a_a^\dagger a_i$. The formulae and the scaling of the CC models considered in this work are shown in Table 4.1. (It is helpful to recognize that the models we consider are invariant to shifts of the boson operators e.g. $b_l \to b_l + \xi_l$ and $b_l^\dagger \to b_l^\dagger + \xi_l^*$, in the sense that any such shift can be absorbed into a redefinition of the coupled cluster amplitudes).

The amplitudes are obtained by solving the projected Schrödinger equation:

$$0 = \langle \Phi_\mu | \mathrm{e}^{-T_{\mathrm{CC}}} H \mathrm{e}^{T_{\mathrm{CC}}} | \Phi_0 \rangle \quad |\Phi_\mu\rangle = \tau_\mu |\Phi_0\rangle \tag{4.7}$$

and the energy is obtained from

$$E_{\mathrm{CC}} = \langle \Phi_0 | \mathrm{e}^{-T_{\mathrm{CC}}} H \mathrm{e}^{T_{\mathrm{CC}}} | \Phi_0 \rangle = \langle \Phi_0 | H_{\mathrm{CC}}(\mathbf{t}) | \Phi_0 \rangle \tag{4.8}$$

where $H_{\mathrm{CC}}(\mathbf{t}) = \mathrm{e}^{-T_{\mathrm{CC}}} H \mathrm{e}^{T_{\mathrm{CC}}}$ is the coupled cluster effective Hamiltonian. The same equations have also been used in coupled cluster theories for cavity polaritons that have been independently developed in Refs. [283–285]. In this study, all the coupled cluster equations were formulated using the WICK package and solved using the Newton-Krylov method, which approximates the inverse Jacobian matrix using the Krylov subspace method [286, 287]. Note that as all matrix elements are evaluated using Wick's theorem, there is no need to truncate the phonon number.

Because the energy is defined from an asymmetric expectation value, the coupled cluster energy is not necessarily variational. In addition, it does not satisfy a Hellman-Feynman theorem, thus in order to obtain observables other than the energy, we instead define a coupled cluster Lagrangian [260],

$$\begin{aligned} \mathcal{L}_{\mathrm{CC}}(t_\mu, \lambda_\mu) &= E_{\mathrm{CC}} + \sum_\mu \lambda_\mu \langle \Phi_\mu | \mathrm{e}^{-T_{\mathrm{CC}}} H \mathrm{e}^{T_{\mathrm{CC}}} | \Phi_0 \rangle \\ &= \langle \Phi_0 | (1 + \Lambda_{\mathrm{CC}})\, \mathrm{e}^{-T_{\mathrm{CC}}} H \mathrm{e}^{T_{\mathrm{CC}}} | \Phi_0 \rangle \end{aligned} \tag{4.9}$$

where λ_μ are the Lagrange multipliers corresponding to the amplitude equations; $\frac{\partial \mathcal{L}_{\mathrm{CC}}}{\partial \lambda_\mu} = 0$ leads to the coupled cluster working equations in Eq. 4.7; $\frac{\partial \mathcal{L}_{\mathrm{CC}}}{\partial t_\mu} = 0$ leads to the equations for the Lagrangian multipliers. The expectation value of the observable O is then,

$$\langle O \rangle = \langle \Phi_0 | (1 + \Lambda_{\mathrm{CC}})\, \mathrm{e}^{-T_{\mathrm{CC}}} O\, \mathrm{e}^{T_{\mathrm{CC}}} | \Phi_0 \rangle \tag{4.10}$$

The mean-field optimization of the reference in Eq. 4.4 already allows for a non-trivial mean-field state (e.g. a localized mean-field state), and we start the coupled cluster equations from both the localized and delocalized mean-field solutions. We also consider a further orbital optimization to make the coupled clus1ter Lagrangian stationary, corresponding to the ansatz

$$|\Psi_{\mathrm{CC}}\rangle = \exp(T_{\mathrm{CC}}) |\Phi_0(\mathbf{A}, \boldsymbol{\xi})\rangle \tag{4.11}$$

where $\mathbf{A}, \boldsymbol{\xi}$ are the parameters in Eq. 4.4, relaxed in the presence of the coupled cluster correlations, and the T_{CC} amplitude are also updated with the orbital parameters. We refer to this mean-field reference as $|\Phi_0^{(\mathrm{CC})}\rangle$. (In practice, we relax $\mathbf{A}$ and update $\boldsymbol{\xi}$ parametrically via $\xi_l = g|A_l|^2/\omega$ as we did in the self-consistent optimization of Eq. 4.4; we find in the Lang-Firsov simulations below that there is little difference between independent optimization of $\boldsymbol{\xi}$ and using this parametric choice).

Variational Lang-Firsov Approach and Perturbation Theory

The Lang-Firsov (LF) transformation is a unitary exponential ansatz to obtain the ground state. In this study, our focus is solely on the diagonal formulation of the Lang-Firsov parameters [262],

$$|\Psi_{\mathrm{LF}}\rangle = \exp\Big(T_{\mathrm{LF}} - T_{\mathrm{LF}}^{\dagger}\Big)|\Phi_0\rangle = U_{\mathrm{LF}}|\Phi_0\rangle \tag{4.12}$$

$$T_{\mathrm{LF}} = \sum_l \lambda_l a_l^{\dagger} a_l b_l^{\dagger} \tag{4.13}$$

and the energy is

$$E_{\mathrm{LF}}(\boldsymbol{\lambda}) = \langle\Phi_0|U_{\mathrm{LF}}^{\dagger}(\boldsymbol{\lambda})\, H\, U_{\mathrm{LF}}(\boldsymbol{\lambda})|\Phi_0\rangle = \langle\Phi_0|H_{\mathrm{LF}}(\boldsymbol{\lambda})|\Phi_0\rangle \tag{4.14}$$

where $H_{\mathrm{LF}}(\boldsymbol{\lambda})$ is the Lang-Firsov Hamiltonian. In the coupled cluster classification this ansatz is a unitary coupled cluster model containing only a type of first-order T_{ep} operator, i.e. a variant of unitary CC0-0-S1, although we refer to it as LF below.

Just as with the coupled cluster ansatz, the LF energy can be computed from different choices of $|\Phi_0\rangle$, and we consider both the delocalized and localized mean-field solutions of Eq. 4.4. In addition, we also reoptimize the reference state $|\Phi_0\rangle$ in the presence of the electron-phonon correlations. This corre-

sponds to defining

$$E_{\mathrm{LF}}(\boldsymbol{\lambda}, \mathbf{A}, \boldsymbol{\xi}) = \langle \Phi_0(\mathbf{A}, \boldsymbol{\xi}) | H_{\mathrm{LF}}(\boldsymbol{\lambda}) | \Phi_0(\mathbf{A}, \boldsymbol{\xi}) \rangle \tag{4.15}$$

and using the analytic gradients obtained in Ref. [262], we minimize E_{LF} with respect to all the parameters. In Ref. [262], this fully optimized Lang-Firsov state is referred to as the Lang-Firsov Hartree-Fock (LF-HF) energy.

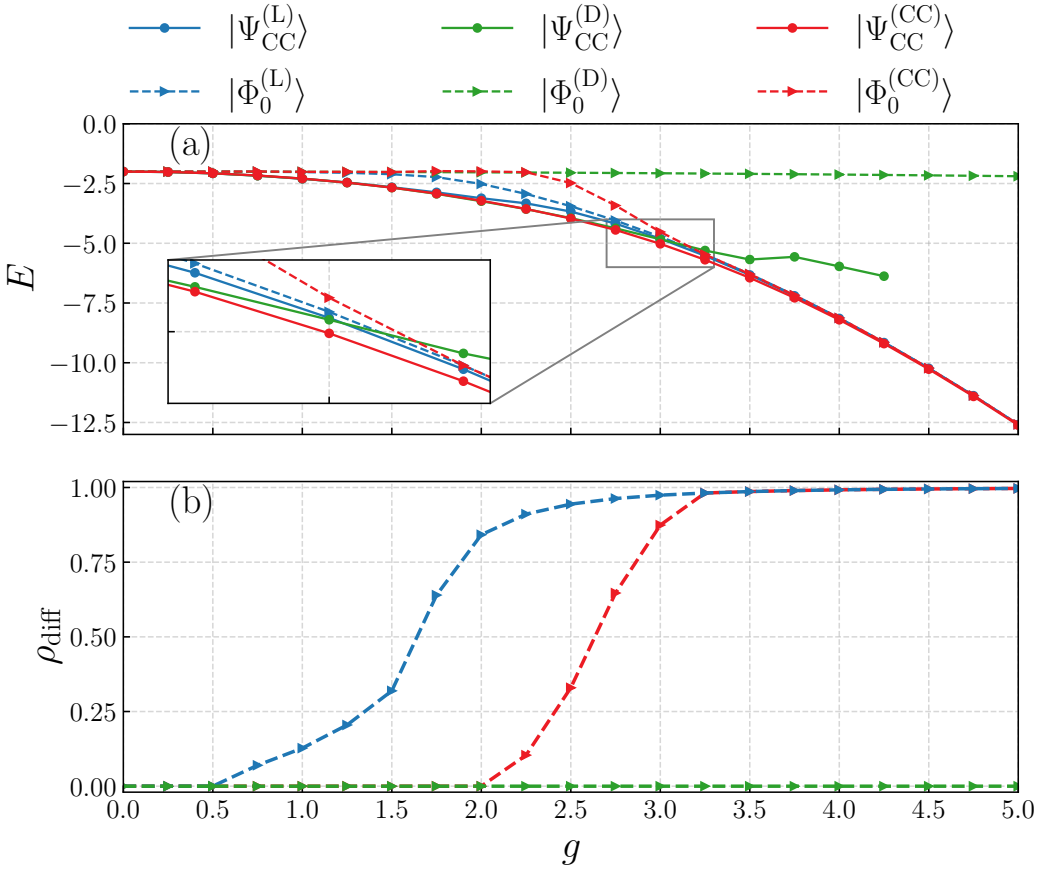

Figure 4.1: The ground-state energy of the 64-site Holstein model with $\omega = 2.0$ and $0 \leq g \leq 5.0$ based on different mean-field reference states. The dashed lines represent the energies of the reference states, and the solid lines represent the energies of the corresponding exponential ansatz. In (a), the energies of the reference states and that of CCS-2-S2 are shown, the inset shows the energies near the transition region; in (b), the density difference ($\rho_{\mathrm{max}} - \rho_{\mathrm{min}}$) of the reference states is plotted.

To incorporate additional electron-phonon correlation, we can carry out perturbation theory.

Similar to the conventional Møller-Plesset (MP) theory utilized in electronic structure theories, we define the zeroth-order Hamiltonian as

$$H_{\mathrm{LF}}^{(0)} = \bar{F} + \omega \sum_{l} \left(\xi_l^2 + b_l^\dagger b_l \right) \tag{4.16}$$

where $\bar{F}$ is the effective electronic Hamiltonian $\langle \Phi_0^{\mathrm{B}} | H^{\mathrm{LF}} | \Phi_0^{\mathrm{B}} \rangle$, where $|\Phi_0^{\mathrm{B}}\rangle$ is the phonon part of the state defined in Eq. 4.4. $|\Phi_0\rangle$ is an eigenstate of $H_{\mathrm{LF}}^{(0)}$ and the corresponding energy is $E_{\mathrm{LF}}^{(0)} = \bar{F}_{00} + \omega \sum_l \xi_l^2$.

The fluctuation potential is then

$$W = H_{\mathrm{LF}} - H_{\mathrm{LF}}^{(0)} \tag{4.17}$$

The corresponding first-order energy correction is

$$E_{\mathrm{LF}}^{(1)} = \langle \Phi_0 | W | \Phi_0 \rangle = E_{\mathrm{LF}} - \bar{F}_{00} \tag{4.18}$$

$$E_{\mathrm{LF}}^{\mathrm{MP1}} = E_{\mathrm{LF}}^{(0)} + E_{\mathrm{LF}}^{(1)} = E_{\text{LF-HF}} + \omega \sum_{l} \xi_l^2 \tag{4.19}$$

which is exactly the LF energy. We then consider the second-order energy correction,

$$E_{\mathrm{LF}}^{(2)} = -\sum_{\mu} \frac{|\langle \Phi_0 | W | \Phi_\mu \rangle|^2}{E_\mu^{(0)} - E_0^{(0)}} \tag{4.20}$$

where $|\Phi_\mu\rangle = \tau_\mu |\Phi_0\rangle$, as described in Eq. 4.6. We evaluate it in a space of electron-phonon configurations following Ref. [262], which requires a truncation of the phonon number. Here, we choose to truncate at 10 phonons per site.

4.3 Density Matrix Renormalization Group Theory

The density matrix renormalization group (DMRG) is a numerically exact method for solving the quantum many-body problem. The method is particularly accurate and efficient for one-dimensional systems [237, 288]. In early

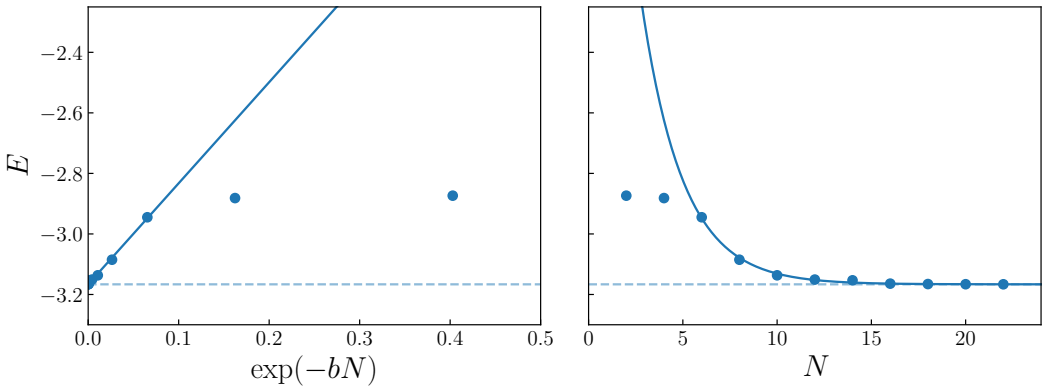

Figure 4.2: Extrapolation of the ground state energy of the 64-site Holstein model with respect to the phonon truncation for $\omega = 0.5$ and $g = 1.15$. The extrapolation is performed with the function $E(N) = E_\infty + a\exp(-bN)$.

developments, DMRG was applied to the Holstein model in Ref. [233] to calculate the ground state energy and the electron-lattice correlation function, and to calculate the dynamical properties of the Holstein model [289]. From a modern perspective, the DMRG method is based on the matrix product state (MPS) representation of the coefficients in Eq. 4.2,

$$C_I = \mathbf{A}^{\sigma_1^I} \cdot \mathbf{B}^{n_1^I} \cdot \mathbf{A}^{\sigma_2^I} \cdot \mathbf{B}^{n_2^I} \cdot \cdots \cdot \mathbf{A}^{\sigma_L^I} \cdot \mathbf{B}^{n_L^I} \tag{4.21}$$

in which $\mathbf{A}^{\sigma_l^I}$ and $\mathbf{B}^{n_l^I}$ are matrices with a maximum bond dimension D, representing the electronic (σ) and phonon (n) degrees of freedom in the site basis, respectively. The Hamiltonian is first transformed to the shifted-phonon basis of the lowest mean-field state of Eq. 4.4, corresponding to

$$\begin{aligned} & b_l^\dagger \to b_l^\dagger + \xi_l^* \quad b_l \to b_l + \xi_l \\ & H \to -t \sum_{\langle kl \rangle} a_k^\dagger a_l - 2g \sum_l \xi_l a_l^\dagger a_l + g \sum_l \rho_l \left(b_l^\dagger + b_l \right) \\ & \quad + \omega \sum_l b_l^\dagger b_l - \omega \sum_l \xi_l \left(b_l^\dagger + b_l \right) \end{aligned} \tag{4.22}$$

and this Hamiltonian is expressed as a matrix product operator (MPO) in the site basis, $H = \sum_{IJ} H_{IJ}|\Phi_I\rangle\langle\Phi_J|$ with,

$$H_{IJ} = \mathbf{W}^{\sigma_1^I \sigma_1^J} \cdot \mathbf{U}^{n_1^I n_1^J} \cdot \ldots \cdot \mathbf{W}^{\sigma_L^I \sigma_L^J} \cdot \mathbf{U}^{n_L^I n_L^J} \tag{4.23}$$

We then optimize the energy expectation value,

$$E = \frac{\langle \Psi_{\mathrm{MPS}} | H_{\mathrm{MPO}} | \Psi_{\mathrm{MPS}} \rangle}{\langle \Psi_{\mathrm{MPS}} | \Psi_{\mathrm{MPS}} \rangle} \tag{4.24}$$

and converge our calculations with respect to the bond dimension D and (shifted) phonon cutoff N. Fig. 4.2 shows the ground state energy of the 64-site Holstein model with respect to the phonon cutoff for $\omega = 0.5$ and $g = 1.15$. The energy is extrapolated to the infinite phonon cutoff limit using the function $E(N) = E_\infty + a\exp(-bN)$, where E_∞ is the extrapolated energy. The bond dimension was kept at $D = 500$ for both electron and boson sites. The electron-phonon DMRG implementation is available through the Block2 package [263, 264].

4.4 Variational Monte Carlo with Neural Quantum States

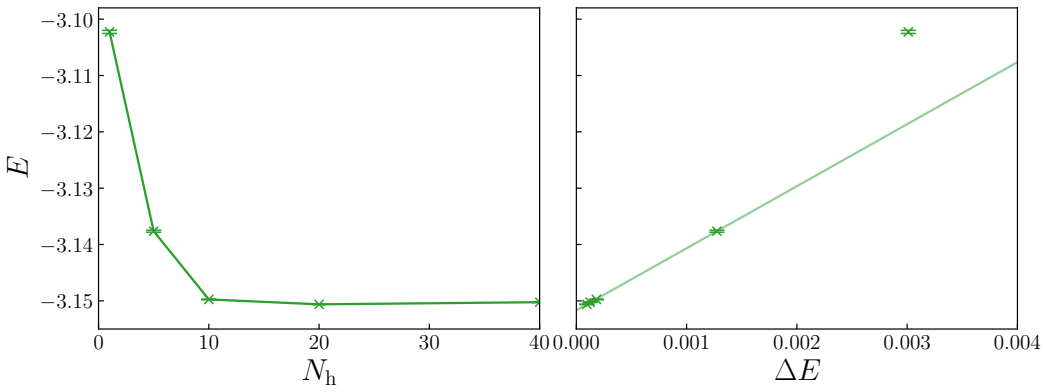

Figure 4.3: Convergence of the NN-VMC ground state energy with the number of hidden neurons and energy variance for the 64-site Holstein model with $\omega = 0.5$ and $g = 1.15$.

A second approach to obtain exact numerical data is to use neural network variational Monte Carlo (VMC) method to predict the coefficients C_I in Eq. 4.3 using a neural net. We use this approach to verify the accuracy of our DMRG benchmarks. Here, we choose to work with electron and phonon configurations in the momentum basis to enforce the exact translational invariance of the Holstein ground-state. We employ a multi-layer perception (MLP) network with three layers as the variational ansatz. It consists of an input layer given by the configuration occupation numbers, followed by a layer of hidden neurons, and a final output neuron. Increasing the number of hidden neurons allows one to systematically enhance the representation power of the state up to numerical exactness, in principle. The Monte Carlo sampling method is performed to calculate the properties of the wave function $|\Psi_{\mathrm{NN}}\rangle$. We sample walkers $|W\rangle$ from the Born distribution of the wavefunction, using continuous time sampling, which is a rejection-free sampling technique. In the VMC approach one is not required to truncate the phonon space, as there are no restrictions on the number of phonons sampled. The gradient of the energy with respect to the variational parameters is similarly sampled, and the variational parameters are optimized using the AMSGrad method, which a variant of gradient descent with momentum.

4.5 Results and Discussions

We apply the methods described in Section 4.2 to the one-dimensional Holstein model within the parameter space of $0.1 \leq \omega \leq 4.0$ and $0 \leq g \leq 5$ in units of t. We use converged DMRG results as the reference, and the convergence of this data is discussed in Appendix 4.3.

Role of the reference

We first discuss the role of the reference state for the coupled cluster method in describing the physics of the Holstein model. We consider the following choices of reference state for the coupled cluster method: (i) the lowest energy optimized mean-field state allowing for (potential) breaking of translational invariance. This reference state is denoted $|\Phi_0^{(\mathrm{L})}\rangle$ and the corresponding exponential ansatz as $|\Psi_{\mathrm{CC}}^{(\mathrm{L})}\rangle$; (ii) the delocalized reference state with $A_l = 1/\sqrt{L}$ and $\xi_l = g/L\omega$, denote as $|\Phi_0^{(\mathrm{D})}\rangle$ with the corresponding $|\Psi_{\mathrm{CC}}^{(\mathrm{D})}\rangle$; and (iii) the reference state that minimizes the coupled cluster energy, denoted as $|\Phi_0^{(\mathrm{CC})}\rangle$ with the corresponding $|\Psi_{\mathrm{CC}}^{(\mathrm{CC})}\rangle$.

We present results from the 64-site Holstein model with $\omega = 2.0$. Fig. 4.1 (a) shows the energy of the reference states (dashed lines) and the corresponding CCS-2-S2 energies (solid lines); Fig. 4.1 (b) plots the density difference $\rho_{\mathrm{diff}} = (\rho_{\mathrm{max}} - \rho_{\mathrm{min}})$ of the reference states as a descriptor of the localization of the reference states. Note that for any coupling constant g, the exact solution predicts a uniform electron density in the ground state. All reference states coincide for small values of g. However, as g increases beyond a critical g, $|\Phi_0^{(\mathrm{L})}\rangle$ and $|\Phi_0^{(\mathrm{CC})}\rangle$ start to transform into localized states with lower energies than the delocalized reference state $|\Phi_0^{(\mathrm{D})}\rangle$. It is important to note that although $|\Phi_0^{(\mathrm{D})}\rangle$ can be obtained for all g, we are unable to converge the coupled cluster amplitude equations in the strong coupling regime and thus cannot obtain $|\Psi_{\mathrm{CC}}^{(\mathrm{D})}\rangle$. The presence of electron-phonon correlation in the optimization of the reference state in $|\Phi_0^{(\mathrm{CC})}\rangle$ shifts the critical g towards a larger value. The density differences in Fig. 4.1 (b) also reflect a smaller amount of symmetry breaking in the $|\Phi_0^{(\mathrm{CC})}\rangle$ compared to $|\Phi_0^{(\mathrm{L})}\rangle$. Interestingly, near the transition ($1.0 \leq g \leq 3.5$) the lowest energy mean-field reference does not result in the

lowest energy coupled cluster energy. As shown in the zoomed-in plot, while $|\Phi_0^{(\mathrm{L})}\rangle$ corresponds to the lowest mean-field energy, the energies of both $|\Psi_{\mathrm{CC}}^{(\mathrm{D})}\rangle$ and $|\Psi_{\mathrm{CC}}^{(\mathrm{CC})}\rangle$ are lower.

The above illustrates the importance of choosing an appropriate reference when using an exponential ansatz. In the sections below, we always use the optimized reference state (iii) for the coupled cluster methods, and perform the full reoptimization of $|\Phi_0\rangle$ in the LF-HF and LF-MP2 calculations.

Energy across parameter space

We now examine the energy errors across the Holstein parameters space for Lang-Firsov and coupled cluster ansatzes. Fig. 4.4 plots the ground state energy error in the 2D parameter space of ω and g for the 64-site Holstein model, while slices through this space are shown in Fig. 4.5 for $\omega = 0.1, 0.5, 1.0$ and 2.0. All methods presented are accurate for $g = 0$ and in the strong coupling regimes, and display most variation in accuracy in the intermediate coupling regime. The dashed lines in Fig. 4.5 represent the coupling strength at the given frequency where the method exhibits its largest error. From this we can conclude that the accuracy roughly follows MF<CCS-1-S1≈LF-HF<LF-MP2<CCS-2-S2. Similar conclusions can be drawn from Fig. 4.5. These slices additionally show that the mean-field error is largest in the anti-adiabatic ($\omega = 2.0$) regime. Despite the similarity of the LF-HF and CCS-1-S1 parametrizations, LF-HF outperforms CCS-1-S1 in this regime: the unitary variational optimization of LF-HF clearly contributes to the improved behaviour in this limit. We see also that LF-MP2 has a discontinuity in the energy at intermediate decoupling, which does not appear in the coupled cluster results.

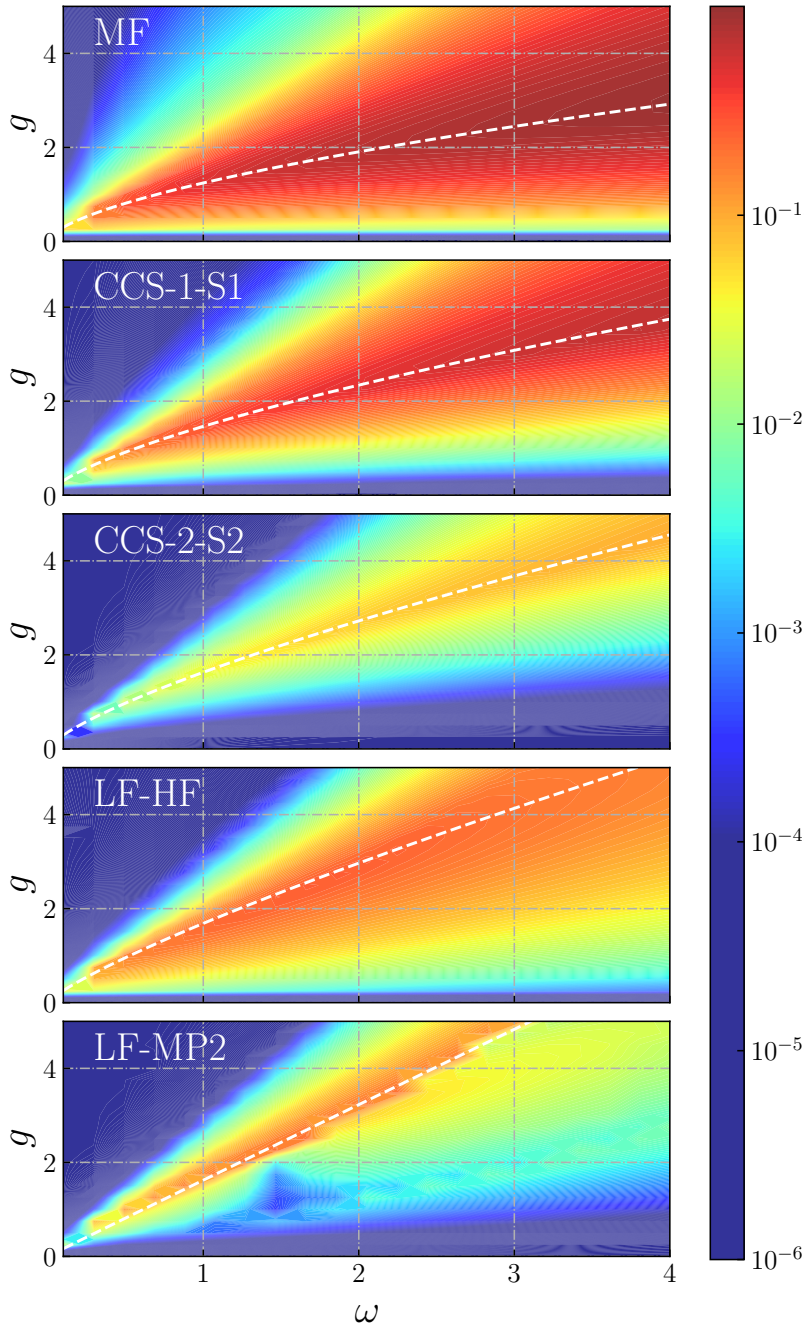

Figure 4.4: The error of the ground state energy (units of t) in the one-dimensional 64-site Holstein model using different methods for $0.1 \leq \omega \leq 4.0$ and $0 \leq g \leq 5$. The white dashed line shows the coupling strength at the given frequency where the method exhibits its largest error. MF is defined in Eq. 4.4, the exponential ansatzes are defined in Table 4.1, and LF-MP2 is defined in Sec. 4.2.

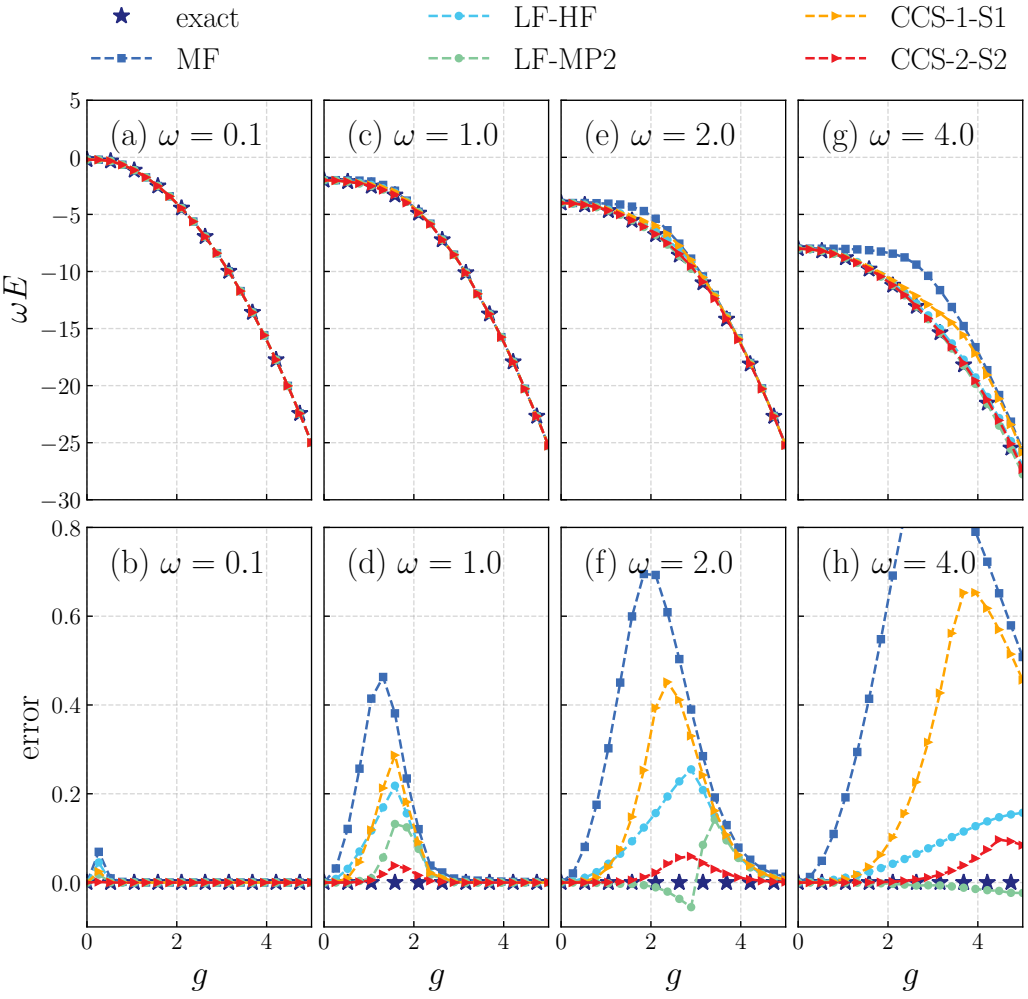

Figure 4.5: ω slices in parameter space for the scaled ground state energy (a, c, e, and g) and the error (b, d, f, and h) in the one-dimensional 64-site Holstein model. Method labels are the same as in Fig. 4.4. (a) and (b) are for $\omega = 0.1$; (c) and (d) are for $\omega = 0.5$; (e) and (f) are for $\omega = 1.0$; (g) and (h) are for $\omega = 2.0$.

Electronic Kinetic Energy

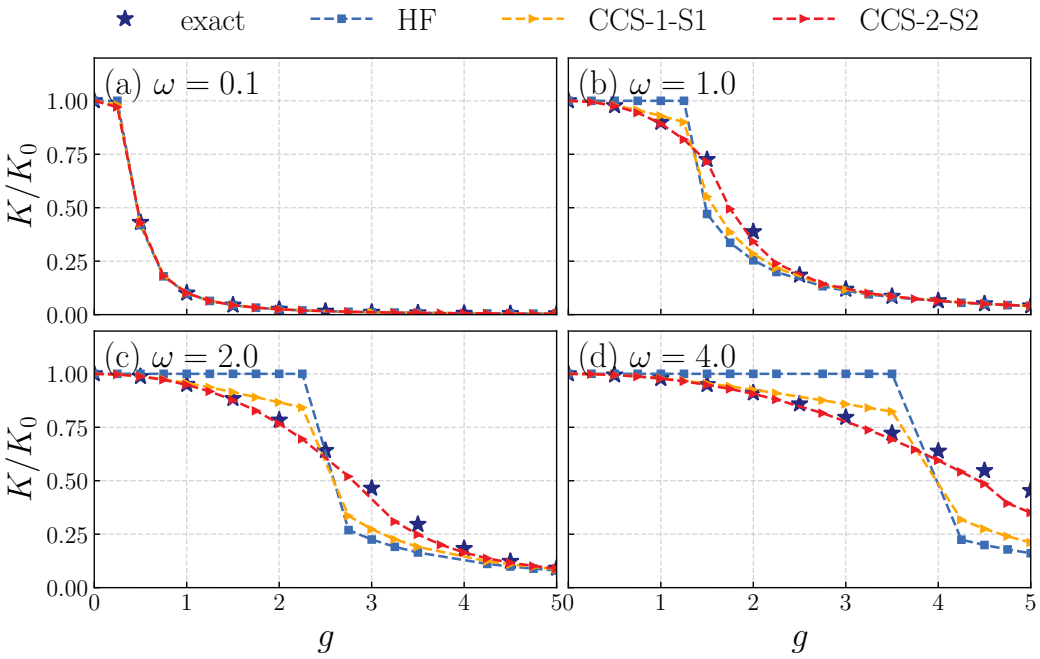

Figure 4.6: The kinetic energy (in units of K_0) of the electron in the one-dimensional 16-site Holstein model. The star symbols represent the exact solution and the dashed lines with symbols represent the approximate numerical methods. Method labels are the same as in Fig. 4.4. (a) $\omega = 0.1$; (b) $\omega = 0.5$; (c) $\omega = 1.0$; and (d) $\omega = 2.0$.

The ratio of the electron kinetic energy (K) to its kinetic energy at zero electron-phonon coupling (K_0) provides a simple way to diagnose the self-trapping transition even in an exact calculation where the ground-state density remains uniform. Fig. 4.6 plots K/K_0 as a function of the electron-phonon coupling strength g in a 16-site Holstein model for the coupled cluster methods. All the methods accurately capture both the strong and weak coupling regimes. However, as previously noted, the simple mean-field method results in a discontinuity. As additional electron-phonon coupling is included, in CCS-1-S1 and CCS-2-S2, the continuity of the transition is gradually restored. Indeed, the CCS-2-S2 result is visually indistinguishable from the exact reference.

Electron-Lattice Correlation

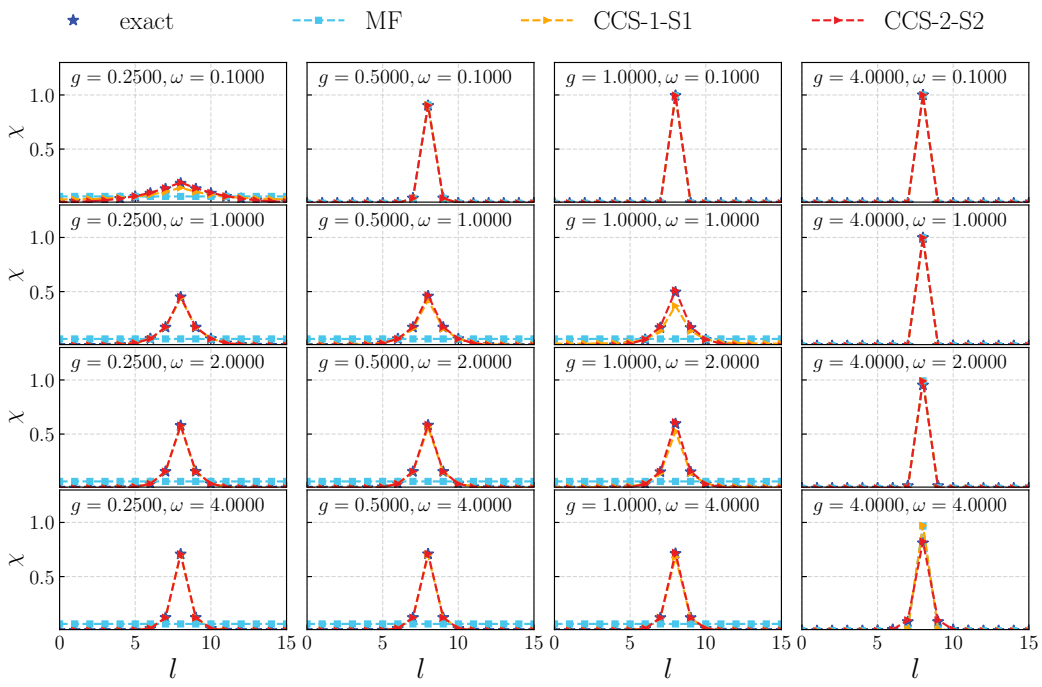

Figure 4.7: Electron-lattice correlation function χ at site 8 in the 16-site Holstein model for various values of ω and g annotated in the figure. Method labels as in Fig. 4.4.

Fig. 4.7 displays the 16-site Holstein model's normalized electron-lattice correlation function for various ω and g values for the MF and CC approximations. (We choose $k = 8$, the middle of the lattice). Note that although the MF solution localizes the electron, there is no localization in the electron-phonon correlation function as $|\Phi_0\rangle$ is a product state, i.e. $\chi_{lk} = \rho_k$. As the inclusion of electron-phonon correlation increases from MF to CCS-1-S1 and CCS-2-S2, the electron-phonon correlation function becomes more compact, even as the spatial localization of the optimized reference state decreases (see Sec. 4.5).

4.6 Conclusions

We have benchmarked the exponential ansatz across the parameter space of the Holstein model, comparing to near-exact results from DMRG. Allowing for a relaxation of the reference state that is the starting point for the exponential ansatz, we find that we can obtain a good description in the weak and strong coupling regimes, corresponding to large and small polarons. Within the systematic coupled cluster framework, increasing the electron-phonon excitation level leads to increasingly accurate results both for the energy and the correlation functions, and at the doubles level of approximation, these results are often visually indistinguishable from the exact ones. The variational Lang-Firsov transformation performs better than the lowest (i.e. singles) rung of the coupled cluster approximation hierarchy, particularly in the intermediate coupling regime.

Looking beyond models, the exponential ansatz is the starting point for a large number of applications in accurate ab initio electronic structure. The results here suggest that it is a competitive approach for polaron physics, providing a viable path forward to describe correlated electron-phonon effects at the ab initio many-body level. Another interesting direction is to examine the application of exponential wavefunctions such as the coupled cluster hierarchy to systems of many-electrons and phonons, along the lines first discussed in Ref. [261]. The incorporation of more flexible references, such as superconducting states, is of particular interest there.

Chapter 5

Conclusion

This dissertation tackles a fundamental challenge in quantum chemistry, namely achieving predictive simulations of strongly correlated crystalline materials from first principles. The work addresses three interconnected challenges, namely describing material-specific properties of strongly correlated superconductors, achieving linear scaling with k-points for large-scale periodic calculations, and establishing reliable methods for electron-phonon interactions. The scalability attained here emerges from advances on two complementary fronts. On the implementation side, GPU acceleration and MPI parallelization enhance computational throughput. On the algorithmic side, novel approximations reduce computational scaling while preserving accuracy. The following discussion concentrates primarily on the algorithmic contributions, which constitute the core methodological advances of this dissertation.

The cuprate superconductivity study presented in Chapter 2 marks a significant advance toward predictive ab initio modeling of correlated superconductors. A key methodological contribution is the demonstration that symmetry-breaking strategies within density matrix embedding theory provide an effective means of computing superconducting order parameters from first principles. The central physical finding extends beyond the observation that this

approach reproduces experimental trends in transition temperatures. More importantly, the calculations explain why simplified models fail. Specifically, multi-orbital covalency effects, absent in one-band Hubbard models, prove essential for the spin fluctuations that drive pairing. By capturing these effects directly from material structures, ab initio methods offer predictive power that model Hamiltonians cannot achieve, thereby enabling efficient screening of candidate superconducting materials. Nevertheless, several limitations temper these conclusions. The current treatment neglects phonons, does not capture long-range spin and charge fluctuations beyond the computational cell, and relies on simplified approximations for doping rather than explicit dopant atoms with structural relaxation. Addressing these limitations constitutes a clear agenda for future work and connects directly to the methodological advances described below.

The methodological developments in Chapter 3 directly enable the large-scale calculations required for the cuprate study and similar applications. This work demonstrates for the first time that tensor hypercontraction of the Coulomb interaction through FFTISDF reduces the k-point scaling from cubic to linear, thereby making thermodynamic limit extrapolations practical for correlated wavefunction methods. When integrated with density matrix embedding theory and local natural orbital methods, this framework delivers converged ground-state energies from MP2, CCSD, and CCSD(T) for crystalline materials. Current limitations include the relatively large number of interpolation points required and difficulties with large real-space grids for transition metal systems. Future development should focus on compact interpolation point protocols, adaptive grid schemes, and integration of Gaussian-type functions as resolution-of-identity bases. These efficiency gains also lay the groundwork for incorporating additional physical effects beyond the electronic structure.

Extending the scope of this dissertation beyond purely electronic structure, Chapter 4 establishes that exponential ansatz wavefunctions provide accurate and systematically improvable descriptions of electron-phonon coupling. Unlike previous approaches based on perturbation theory or variational Monte Carlo, the Holstein model benchmarks presented here reveal that coupled cluster theory and variational Lang-Firsov methods, when combined with appropriate reference state optimization, accurately capture polaron formation across weak to strong coupling regimes. This finding carries significant implications because it validates the extension of the coupled cluster hierarchy, a cornerstone of modern quantum chemistry, to electron-phonon problems. The primary limitation is that these benchmarks involve single-electron models. Consequently, extending to many-electron systems with phonons, particularly with superconducting reference states, remains an important open direction.

Looking forward, several concrete directions merit exploration. For cuprate modeling, incorporating phonons and developing methods to capture long-range fluctuations would enable more complete descriptions of the pairing mechanism. For FFTISDF, reducing the interpolation point count and handling transition metals more efficiently would broaden applicability. For electron-phonon methods, extending coupled cluster theory to many-electron systems with phonons would open pathways to ab initio studies of phonon-mediated superconductivity. More ambitiously, combining all three advances into a unified framework for correlated electron-phonon systems in the thermodynamic limit represents a long-term goal that now appears achievable.

Bibliography

[1] G. Moore, "Cramming More Components Onto Integrated Circuits", Proc. IEEE **86**, 82–85 (1998).

[2] Wm. A. Wulf and S. A. McKee, "Hitting the memory wall: Implications of the obvious", SIGARCH Comput. Archit. News **23**, 20–24 (1995).

[3] G. M. Amdahl, "Validity of the single processor approach to achieving large scale computing capabilities", in Proceedings of the April 18-20, 1967, spring joint computer conference on - AFIPS '67 (Spring) (1967), p. 483.

[4] R. M. Martin, *Electronic Structure: Basic Theory and Practical Methods*, 1st ed. (Cambridge University Press, Apr. 8, 2004).

[5] M. Born and R. Oppenheimer, "Zur Quantentheorie der Molekeln", Annalen der Physik **389**, 457–484 (1927).

[6] H. J. Monkhorst, "Chemical physics without the Born-Oppenheimer approximation: The molecular coupled-cluster method", Phys. Rev. A **36**, 1544–1561 (1987).

[7] J. Hubbard, "Electron correlations in narrow energy bands", Proceedings of the Royal Society of London. Series A. Mathematical and Physical Sciences **276**, 238–257 (1963).

[8] N. Schuch and F. Verstraete, "Computational complexity of interacting electrons and fundamental limitations of density functional theory", Nature Phys **5**, 732–735 (2009).

[9] W. J. Hehre, R. F. Stewart, and J. A. Pople, "Self-Consistent Molecular-Orbital Methods. I. Use of Gaussian Expansions of Slater-Type Atomic Orbitals", The Journal of Chemical Physics **51**, 2657–2664 (1969).

[10] M. C. Payne, M. P. Teter, D. C. Allan, T. A. Arias, and J. D. Joannopoulos, "Iterative minimization techniques for *ab initio* total-energy calculations: Molecular dynamics and conjugate gradients", Rev. Mod. Phys. **64**, 1045–1097 (1992).

[11] V. Szalay, "Discrete variable representations of differential operators", The Journal of Chemical Physics **99**, 1978–1984 (1993).

[12] R. J. Bartlett and M. Musiał, "Coupled-cluster theory in quantum chemistry", Rev. Mod. Phys. **79**, 291–352 (2007).

[13] I. Shavitt and R. J. Bartlett, *Many-Body Methods in Chemistry and Physics: MBPT and Coupled-Cluster Theory*, 1st ed. (Cambridge University Press, Aug. 6, 2009).

[14] T. Helgaker, P. Jørgensen, and J. Olsen, *Molecular Electronic-Structure Theory* (Wiley, Hoboken, 2014), 940 pp.

[15] A. D. Becke, "Density-functional thermochemistry. III. The role of exact exchange", The Journal of Chemical Physics **98**, 5648–5652 (1993).

[16] W. M. C. Foulkes, L. Mitas, R. J. Needs, and G. Rajagopal, "Quantum Monte Carlo simulations of solids", Rev. Mod. Phys. **73**, 33–83 (2001).

[17] S. Sharma, A. A. Holmes, G. Jeanmairet, A. Alavi, and C. J. Umrigar, "Semistochastic Heat-Bath Configuration Interaction Method: Selected Configuration Interaction with Semistochastic Perturbation Theory", J. Chem. Theory Comput. **13**, 1595–1604 (2017).

[18] P.-F. Loos, Y. Damour, and A. Scemama, "The performance of CIPSI on the ground state electronic energy of benzene", The Journal of Chemical Physics **153**, 176101 (2020).

[19] Chr. Møller and M. S. Plesset, "Note on an Approximation Treatment for Many-Electron Systems", Phys. Rev. **46**, 618–622 (1934).

[20] D. Cremer, "Møller–Plesset perturbation theory: From small molecule methods to methods for thousands of atoms", WIREs Comput Mol Sci **1**, 509–530 (2011).

[21] J. Olsen, P. Jørgensen, T. Helgaker, and O. Christiansen, "Divergence in Møller–Plesset theory: A simple explanation based on a two-state model", The Journal of Chemical Physics **112**, 9736–9748 (2000).

[22] R. M. Martin, L. Reining, and D. M. Ceperley, *Interacting Electrons: Theory and Computational Approaches*, 1st ed. (Cambridge University Press, May 31, 2016).

[23] F. Coester, "Bound states of a many-particle system", Nuclear Physics **7**, 421–424 (1958).

[24] J. Cizek and J. Paldus, "Coupled Cluster Approach", Phys. Scr. **21**, 251–254 (1980).

[25] R. J. Bartlett and J. F. Stanton, "Applications of Post-Hartree—Fock Methods: A Tutorial", in *Reviews in Computational Chemistry*, Vol. 5, edited by K. B. Lipkowitz and D. B. Boyd, 1st ed. (Wiley, Jan. 1994), pp. 65–169.

[26] M. B. Hastings, "An area law for one-dimensional quantum systems", J. Stat. Mech. **2007**, P08024–P08024 (2007).

[27] F. Verstraete, V. Murg, and J. Cirac, "Matrix product states, projected entangled pair states, and variational renormalization group methods for quantum spin systems", Advances in Physics **57**, 143–224 (2008).

[28] G. K.-L. Chan, "An algorithm for large scale density matrix renormalization group calculations", The Journal of Chemical Physics **120**, 3172–3178 (2004).

[29] G. K.-L. Chan, M. Kállay, and J. Gauss, "State-of-the-art density matrix renormalization group and coupled cluster theory studies of the nitrogen binding curve", The Journal of Chemical Physics **121**, 6110–6116 (2004).

[30] F. Verstraete, T. Nishino, U. Schollwöck, M. C. Bañuls, G. K. Chan, and M. E. Stoudenmire, "Density matrix renormalization group, 30 years on", Nat Rev Phys **5**, 273–276 (2023).

[31] M. J. O'Rourke, Z. Li, and G. K.-L. Chan, "Efficient representation of long-range interactions in tensor network algorithms", Phys. Rev. B **98**, 205127 (2018).

[32] F. Becca and S. Sorella, *Quantum Monte Carlo Approaches for Correlated Systems*, 1st ed. (Cambridge University Press, Nov. 30, 2017).

[33] P. Pulay, "Localizability of dynamic electron correlation", Chemical Physics Letters **100**, 151–154 (1983).

[34] W. Kohn, "Density Functional and Density Matrix Method Scaling Linearly with the Number of Atoms", Phys. Rev. Lett. **76**, 3168–3171 (1996).

[35] S. Li, J. Ma, and Y. Jiang, "Linear scaling local correlation approach for solving the coupled cluster equations of large systems", J Comput Chem **23**, 237–244 (2002).

[36] J.-L. Li, G.-M. Rignanese, and S. G. Louie, "Quasiparticle energy bands of NiO in the G W approximation", Phys. Rev. B **71**, 193102 (2005).

[37] Z. Rolik and M. Kállay, "A general-order local coupled-cluster method based on the cluster-in-molecule approach", The Journal of Chemical Physics **135**, 104111 (2011).

[38] Z. Rolik, L. Szegedy, I. Ladjánszki, B. Ladóczki, and M. Kállay, "An efficient linear-scaling CCSD(T) method based on local natural orbitals", The Journal of Chemical Physics **139**, 094105 (2013).

[39] W. Li, Z. Ni, and S. Li, "Cluster-in-molecule local correlation method for post-Hartree–Fock calculations of large systems", Molecular Physics **114**, 1447–1460 (2016).

[40] C. Hampel and H.-J. Werner, "Local treatment of electron correlation in coupled cluster theory", The Journal of Chemical Physics **104**, 6286–6297 (1996).

[41] C. Hättig, D. P. Tew, and B. Helmich, "Local explicitly correlated second- and third-order Møller–Plesset perturbation theory with pair natural orbitals", The Journal of Chemical Physics **136**, 204105 (2012).

[42] C. Riplinger and F. Neese, "An efficient and near linear scaling pair natural orbital based local coupled cluster method", The Journal of Chemical Physics **138**, 034106 (2013).

[43] M. Schwilk, Q. Ma, C. Köppl, and H.-J. Werner, "Scalable Electron Correlation Methods. 3. Efficient and Accurate Parallel Local Coupled Cluster with Pair Natural Orbitals (PNO-LCCSD)", J. Chem. Theory Comput. **13**, 3650–3675 (2017).

[44] Y. Guo, C. Riplinger, U. Becker, D. G. Liakos, Y. Minenkov, L. Cavallo, and F. Neese, "Communication: An improved linear scaling perturbative triples correction for the domain based local pair-natural orbital based singles and doubles coupled cluster method [DLPNO-CCSD(T)]", The Journal of Chemical Physics **148**, 011101 (2018).

[45] M. Ziółkowski, B. Jansík, T. Kjærgaard, and P. Jørgensen, "Linear scaling coupled cluster method with correlation energy based error control", The Journal of Chemical Physics **133**, 014107 (2010).

[46] K. Kristensen, I.-M. Høyvik, B. Jansik, P. Jørgensen, T. Kjærgaard, S. Reine, and J. Jakowski, "MP2 energy and density for large molecular systems with internal error control using the Divide-Expand-Consolidate scheme", Phys. Chem. Chem. Phys. **14**, 15706 (2012).

[47] P. Y. Ayala and G. E. Scuseria, "Linear scaling second-order Moller–Plesset theory in the atomic orbital basis for large molecular systems", The Journal of Chemical Physics **110**, 3660–3671 (1999).

[48] G. E. Scuseria and P. Y. Ayala, "Linear scaling coupled cluster and perturbation theories in the atomic orbital basis", The Journal of Chemical Physics **111**, 8330–8343 (1999).

[49] T. A. Wesolowski and A. Warshel, "Frozen density functional approach for ab initio calculations of solvated molecules", J. Phys. Chem. **97**, 8050–8053 (1993).

[50] J. D. Goodpaster, N. Ananth, F. R. Manby, and T. F. Miller, "Exact nonadditive kinetic potentials for embedded density functional theory", The Journal of Chemical Physics **133**, 084103 (2010).

[51] C. Huang, M. Pavone, and E. A. Carter, "Quantum mechanical embedding theory based on a unique embedding potential", The Journal of Chemical Physics **134**, 154110 (2011).

[52] F. Libisch, C. Huang, and E. A. Carter, "Embedded Correlated Wavefunction Schemes: Theory and Applications", Acc. Chem. Res. **47**, 2768–2775 (2014).

[53] H.-Z. Ye, H. K. Tran, and T. Van Voorhis, "Bootstrap Embedding For Large Molecular Systems", J. Chem. Theory Comput. **16**, 5035–5046 (2020).

[54] M. Nusspickel and G. H. Booth, "Systematic Improvability in Quantum Embedding for Real Materials", Phys. Rev. X **12**, 011046 (2022).

[55] A. Shee, F. M. Faulstich, K. B. Whaley, L. Lin, and M. Head-Gordon, "A static quantum embedding scheme based on coupled cluster theory", The Journal of Chemical Physics **161**, 164107 (2024).

[56] E. Rebolini, G. Baardsen, A. S. Hansen, K. R. Leikanger, and T. B. Pedersen, "Divide–Expand–Consolidate Second-Order Møller–Plesset Theory with Periodic Boundary Conditions", J. Chem. Theory Comput. **14**, 2427–2438 (2018).

[57] Y. Wang, Z. Ni, W. Li, and S. Li, "Cluster-in-Molecule Local Correlation Approach for Periodic Systems", J. Chem. Theory Comput. **15**, 2933–2943 (2019).

[58] S. J. R. Lee, M. Welborn, F. R. Manby, and T. F. Miller, "Projection-Based Wavefunction-in-DFT Embedding", Acc. Chem. Res. **52**, 1359–1368 (2019).

[59] T. Zhu, Z.-H. Cui, and G. K.-L. Chan, "Efficient Formulation of Ab Initio Quantum Embedding in Periodic Systems: Dynamical Mean-Field Theory", J. Chem. Theory Comput. **16**, 141–153 (2020).

[60] Y. Wang, I. Esterlis, T. Shi, J. I. Cirac, and E. Demler, "Zero-temperature phases of the two-dimensional Hubbard-Holstein model: A non-Gaussian exact diagonalization study", Phys. Rev. Research **2**, 043258 (2020).

[61] B. Chen and X. Xu, "XO-PBC: An Accurate and Efficient Method for Molecular Crystals", J. Chem. Theory Comput. **16**, 4271–4285 (2020).

[62] O. R. Meitei and T. Van Voorhis, "Periodic Bootstrap Embedding", J. Chem. Theory Comput. **19**, 3123–3130 (2023).

[63] W. Li, Y. Wang, Z. Ni, and S. Li, "Cluster-in-Molecule Local Correlation Method for Dispersion Interactions in Large Systems and Periodic Systems", Acc. Chem. Res. **56**, 3462–3474 (2023).

[64] Z.-H. Cui, T. Zhu, and G. K.-L. Chan, "Efficient Implementation of Ab Initio Quantum Embedding in Periodic Systems: Density Matrix Embedding Theory", J. Chem. Theory Comput. **16**, 119–129 (2020).

[65] Z.-H. Cui, H. Zhai, X. Zhang, and G. K.-L. Chan, "Systematic electronic structure in the cuprate parent state from quantum many-body simulations", Science **377**, 1192–1198 (2022).

[66] Z.-H. Cui, J. Yang, J. Tölle, H.-Z. Ye, S. Yuan, H. Zhai, G. Park, R. Kim, X. Zhang, L. Lin, T. C. Berkelbach, and G. K.-L. Chan, "Ab initio quantum many-body description of superconducting trends in the cuprates", Nat Commun **16**, 1845 (2025).

[67] D. Zgid and G. K.-L. Chan, "Dynamical mean-field theory from a quantum chemical perspective", The Journal of Chemical Physics **134**, 094115 (2011).

[68] Q. Sun and G. K.-L. Chan, "Quantum Embedding Theories", Acc. Chem. Res. **49**, 2705–2712 (2016).

[69] H.-Z. Ye and T. C. Berkelbach, "Periodic Local Coupled-Cluster Theory for Insulators and Metals", J. Chem. Theory Comput. **20**, 8948–8959 (2024).

[70] G. Knizia and G. K.-L. Chan, "Density matrix embedding: A strong-coupling quantum embedding theory", Journal of chemical theory and computation **9**, 1428–1432 (2013).

[71] S. Wouters, C. A. Jiménez-Hoyos, Q. Sun, and G. K.-L. Chan, "A Practical Guide to Density Matrix Embedding Theory in Quantum Chemistry", J. Chem. Theory Comput. **12**, 2706–2719 (2016).

[72] A. Georges, G. Kotliar, W. Krauth, and M. J. Rozenberg, "Dynamical mean-field theory of strongly correlated fermion systems and the limit of infinite dimensions", Rev. Mod. Phys. **68**, 13–125 (1996).

[73] G. Kotliar, S. Y. Savrasov, K. Haule, V. S. Oudovenko, O. Parcollet, and C. A. Marianetti, "Electronic structure calculations with dynamical mean-field theory", Rev. Mod. Phys. **78**, 865–951 (2006).

[74] S. Haldar, A. Mitra, M. R. Hermes, and L. Gagliardi, "Local Excitations of a Charged Nitrogen Vacancy in Diamond with Multireference Density Matrix Embedding Theory", J. Phys. Chem. Lett. **14**, 4273–4280 (2023).

[75] B. T. G. Lau, B. Busemeyer, and T. C. Berkelbach, "Optical Properties of Defects in Solids via Quantum Embedding with Good Active Space Orbitals", J. Phys. Chem. C **128**, 2959–2966 (2024).

[76] H. Q. Pham, M. R. Hermes, and L. Gagliardi, "Periodic Electronic Structure Calculations with the Density Matrix Embedding Theory", J. Chem. Theory Comput. **16**, 130–140 (2020).

[77] B. T. G. Lau, G. Knizia, and T. C. Berkelbach, "Regional Embedding Enables High-Level Quantum Chemistry for Surface Science", J. Phys. Chem. Lett. **12**, 1104–1109 (2021).

[78] H.-Z. Ye and T. C. Berkelbach, "Correlation-Consistent Gaussian Basis Sets for Solids Made Simple", J. Chem. Theory Comput. **18**, 1595–1606 (2022).

[79] J. Pipek and P. G. Mezey, "A fast intrinsic localization procedure applicable for *a b i n i t i o* and semiempirical linear combination of atomic orbital wave functions", The Journal of Chemical Physics **90**, 4916–4926 (1989).

[80] W. Metzner and D. Vollhardt, "Correlated Lattice Fermions in d = ∞ Dimensions", Phys. Rev. Lett. **62**, 324–327 (1989).

[81] A. Georges and G. Kotliar, "Hubbard model in infinite dimensions", Phys. Rev. B **45**, 6479–6483 (1992).

[82] Y. Lu, M. Höppner, O. Gunnarsson, and M. W. Haverkort, "Efficient real-frequency solver for dynamical mean-field theory", Phys. Rev. B **90**, 085102 (2014).

[83] R. Bulla, T. A. Costi, and T. Pruschke, "Numerical renormalization group method for quantum impurity systems", Rev. Mod. Phys. **80**, 395–450 (2008).

[84] E. Koch, G. Sangiovanni, and O. Gunnarsson, "Sum rules and bath parametrization for quantum cluster theories", Phys. Rev. B **78**, 115102 (2008).

[85] I. De Vega, U. Schollwöck, and F. A. Wolf, "How to discretize a quantum bath for real-time evolution", Phys. Rev. B **92**, 155126 (2015).

[86] A. Ekert and P. L. Knight, "Entangled quantum systems and the Schmidt decomposition", American Journal of Physics **63**, 415–423 (1995).

[87] I. Peschel, "Special Review: Entanglement in Solvable Many-Particle Models", Braz J Phys **42**, 267–291 (2012).

[88] N. Plakida, *High-temperature cuprate superconductors: experiment, theory, and applications*, Vol. 166 (Springer Science & Business Media, 2010).

[89] M. R. Norman, "The challenge of unconventional superconductivity", Science **332**, 196–200 (2011).

[90] L. Gao, Y. Xue, F. Chen, Q. Xiong, R. Meng, D. Ramirez, C. Chu, J. Eggert, and H. Mao, "Superconductivity up to 164 K in $HgBa_2Ca_{m-1}Cu_mO_{2m+2+\delta}$ (m = 1, 2, and 3) under quasihydrostatic pressures", Phys. Rev. B **50**, 4260 (1994).

[91] A. Yamamoto, N. Takeshita, C. Terakura, and Y. Tokura, "High pressure effects revisited for the cuprate superconductor family with highest critical temperature", Nat. comm. **6**, 8990 (2015).

[92] E. Antipov, A. Abakumov, and S. Putilin, "Chemistry and structure of Hg-based superconducting Cu mixed oxides", Supercond. Sci. Tech. **15**, R31 (2002).

[93] E. Dagotto, "Complexity in strongly correlated electronic systems", Science **309**, 257–262 (2005).

[94] L. N. d. Oliveira, E. Gross, and W. Kohn, "Density-functional theory for superconductors", Phys. Rev. Lett. **60**, 2430 (1988).

[95] M. Lüders, M. Marques, N. Lathiotakis, A. Floris, G. Profeta, L. Fast, A. Continenza, S. Massidda, and E. Gross, "Ab initio theory of superconductivity. I. Density functional formalism and approximate functionals", Phys. Rev. B **72**, 024545 (2005).

[96] M. Qin, T. Schäfer, S. Andergassen, P. Corboz, and E. Gull, "The Hubbard model: A computational perspective", Annu. Rev. Condens. Matter Phys. **13**, 275–302 (2022).

[97] M. T. Schmid, J.-B. Morée, Y. Yamaji, and M. Imada, "Superconductivity studied by solving ab initio low-energy effective Hamiltonians for carrier doped $CaCuO_2$, $Bi_2Sr_2CuO_6$, $Bi_2Sr_2CaCu_2O_8$, and $HgBa_2CuO_4$", arXiv preprint arXiv:2303.06672 (2023).

[98] B.-X. Zheng, C.-M. Chung, P. Corboz, G. Ehlers, M.-P. Qin, R. M. Noack, H. Shi, S. R. White, S. Zhang, and G. K.-L. Chan, "Stripe order in the underdoped region of the two-dimensional Hubbard model", Science **358**, 1155–1160 (2017).

[99] E. W. Huang, C. B. Mendl, S. Liu, S. Johnston, H.-C. Jiang, B. Moritz, and T. P. Devereaux, "Numerical evidence of fluctuating stripes in the normal state of high-T_c cuprate superconductors", Science **358**, 1161–1164 (2017).

[100] M. Qin, C.-M. Chung, H. Shi, E. Vitali, C. Hubig, U. Schollwöck, S. R. White, and S. Zhang, "Absence of superconductivity in the pure two-dimensional Hubbard model", Phys. Rev. X **10**, 031016 (2020).

[101] S. Jiang, D. J. Scalapino, and S. R. White, "Ground-state phase diagram of the t-t'-J model", Proc. Natl. Acad. Sci. **118**, e2109978118 (2021).

[102] P. Mai, N. S. Nichols, S. Karakuzu, F. Bao, A. Del Maestro, T. A. Maier, and S. Johnston, "Robust charge-density-wave correlations in the electron-doped single-band Hubbard model", Nat. Comm. **14**, 2889 (2023).

[103] P. R. C. Kent, T. Saha-Dasgupta, O. Jepsen, O. K. Andersen, A. Macridin, T. A. Maier, M. Jarrell, and T. C. Schulthess, "Combined density functional and dynamical cluster quantum Monte Carlo calculations of the three-band Hubbard model for hole-doped cuprate superconductors", Phys. Rev. B **78**, 035132 (2008).

[104] C. Weber, C. Yee, K. Haule, and G. Kotliar, "Scaling of the transition temperature of hole-doped cuprate superconductors with the charge-transfer energy", EPL **100**, 37001 (2012).

[105] N. Kowalski, S. S. Dash, P. Sémon, D. Sénéchal, and A.-M. Tremblay, "Oxygen hole content, charge-transfer gap, covalency, and cuprate superconductivity", Proc. Natl. Acad. Sci. **118**, e2106476118 (2021).

[106] X. Wang, L. De'Medici, H. Park, C. Marianetti, and A. J. Millis, "Covalency, double-counting, and the metal-insulator phase diagram in transition metal oxides", Phys. Rev. B **86**, 195136 (2012).

[107] J. Karp, A. Hampel, and A. J. Millis, "Dependence of DFT+ DMFT results on the construction of the correlated orbitals", Phys. Rev. B **103**, 195101 (2021).

[108] S. Jiang, D. J. Scalapino, and S. R. White, "A single-band model with enhanced pairing from dmrg-based downfolding of the three-band hubbard model", arXiv preprint arXiv:2303.00756 (2023).

[109] Z.-H. Cui, H. Zhai, X. Zhang, and G. K.-L. Chan, "Systematic electronic structure in the cuprate parent state from quantum many-body simulations", Science **377**, 1192 (2022),

[110] L. Nordheim, "The electron theory of metals", Ann. Phys. **9**, 607 (1931).

[111] L. Bellaiche and D. Vanderbilt, "Virtual crystal approximation revisited: application to dielectric and piezoelectric properties of perovskites", Phys. Rev. B **61**, 7877 (2000).

[112] Q. Sun, T. C. Berkelbach, N. S. Blunt, G. H. Booth, S. Guo, Z. Li, J. Liu, J. D. McClain, E. R. Sayfutyarova, S. Sharma, S. Wouters, and G. K.-L. Chan, "PySCF: the Python-based simulations of chemistry framework", WIREs Comput. Mol. Sci. **8**, e1340 (2018).

[113] Q. Sun, X. Zhang, S. Banerjee, P. Bao, M. Barbry, N. S. Blunt, N. A. Bogdanov, G. H. Booth, J. Chen, Z.-H. Cui, J. J. Eriksen, Y. Gao, S. Guo, J. Hermann, M. R. Hermes, K. Koh, P. Koval, S. Lehtola, Z. Li, J. Liu, N. Mardirossian, J. D. McClain, M. Motta, B. Mussard, H. Q. Pham, A. Pulkin, W. Purwanto, P. J. Robinson, E. Ronca, E. Sayfutyarova, M. Scheurer, H. F. Schurkus, J. E. T. Smith, C. Sun, S.-N. Sun, S. Upadhyay, L. K. Wagner, X. Wang, A. White, J. D. Whitfield, M. J. Williamson, S. Wouters, J. Yang, J. M. Yu, T. Zhu, T. C. Berkelbach, S. Sharma, A. Sokolov, and G. K.-L. Chan, "Recent developments in the PySCF program package", J. Chem. Phys. **153**, 024109 (2020),

[114] G. Kresse and J. Hafner, "Ab initio molecular dynamics for liquid metals", Phys. Rev. B **47**, 558 (1993).

[115] G. Kresse and J. Hafner, "Ab initio molecular-dynamics simulation of the liquid-metal–amorphous-semiconductor transition in germanium", Phys. Rev. B **49**, 14251 (1994).

[116] G. Kresse and J. Furthmüller, "Efficiency of ab-initio total energy calculations for metals and semiconductors using a plane-wave basis set", Comp. Mater. Sci. **6**, 15–50 (1996).

[117] G. Kresse and J. Furthmüller, "Efficient iterative schemes for *ab initio* total-energy calculations using a plane-wave basis set", Phys. Rev. B **54**, 11169 (1996).

[118] G. Kresse and D. Joubert, "From ultrasoft pseudopotentials to the projector augmented-wave method", Phys. Rev. B **59**, 1758–1775 (1999).

[119] S. Goedecker, M. Teter, and J. Hutter, "Separable dual-space gaussian pseudopotentials", Phys. Rev. B **54**, 1703–1710 (1996).

[120] C. Hartwigsen, S. Goedecker, and J. Hutter, "Relativistic separable dual-space gaussian pseudopotentials from H to Rn", Phys. Rev. B **58**, 3641–3662 (1998).

[121] P. E. Blöchl, "Projector augmented-wave method", Phys. Rev. B **50**, 17953 (1994).

[122] J. P. Perdew, M. Ernzerhof, and K. Burke, "Rationale for mixing exact exchange with density functional approximations", J. Chem. Phys. **105**, 9982 (1996).

[123] Z.-H. Cui, T. Zhu, and G. K.-L. Chan, "Efficient implementation of ab initio quantum embedding in periodic systems: density matrix embedding theory", J. Chem. Theory Comput. **16**, 119–129 (2020),

[124] libDMET: A library of density matrix embedding theory (DMET) for lattice models and realistic solids, https://github.com/gkclab/libdmet_preview .

[125] MPI4PySCF, An MPI plugin for PySCF, https://github.com/zhcui/mpi4pyscf .

[126] H. Zhai and G. K.-L. Chan, "Low communication high performance ab initio density matrix renormalization group algorithms", J. Chem. Phys. **154**, 224116 (2021).

[127] B. Lorenz and C. Chu, "High pressure effects on superconductivity", in, Frontiers in Superconducting Materials (Springer, 2005), pp. 459–497.

[128] J. S. Schilling, "High-pressure effects", Handbook of High-Temperature Superconductivity: Theory and Experiment, 427–462 (2007).

[129] Z.-H. Cui, C. Sun, U. Ray, B.-X. Zheng, Q. Sun, and G. K.-L. Chan, "Ground-state phase diagram of the three-band Hubbard model from density matrix embedding theory", Phys. Rev. Research **2**, 043259 (2020),

[130] R. Liang, D. Bonn, and W. Hardy, "Evaluation of cuo$_2$ plane hole doping in $YBa_2Cu_3O_{6+x}$ single crystals", Phys. Rev. B **73**, 180505 (2006).

[131] A. Yamamoto, W.-Z. Hu, and S. Tajima, "Thermoelectric power and resistivity of $HgBa_2CuO_{4+\delta}$ over a wide doping range", Phys. Rev. B **63**, 024504 (2000).

[132] B.-X. Zheng and G. K.-L. Chan, "Ground-state phase diagram of the square lattice Hubbard model from density matrix embedding theory", Phys. Rev. B **93**, 035126 (2016).

[133] M. Azuma, Z. Hiroi, M. Takano, Y. Bando, and Y. Takeda, "Superconductivity at 110 K in the infinite-layer compound $(Sr_{1-x}Ca_x)_{1-y}CuO_2$", Nature **356**, 775–776 (1992).

[134] P. Radaelli, J. Wagner, B. Hunter, M. Beno, G. Knapp, J. Jorgensen, and D. Hinks, "Structure, doping and superconductivity in $HgBa_2CaCu_2O_{6+\delta}$ ($T_c \leqslant 128$ K)", Physica C: Supercond. **216**, 29–35 (1993).

[135] See supplementary materials.

[136] M. Marsman, A. Grüneis, J. Paier, and G. Kresse, "Second-order Møller–Plesset perturbation theory applied to extended systems. I. Within the projector-augmented-wave formalism using a plane wave basis set", The Journal of Chemical Physics **130**, 184103 (2009).

[137] C. Müller and B. Paulus, "Wavefunction-based electron correlation methods for solids", Phys. Chem. Chem. Phys. **14**, 7605 (2012).

[138] G. H. Booth, A. Grüneis, G. Kresse, and A. Alavi, "Towards an exact description of electronic wavefunctions in real solids", Nature **493**, 365–370 (2013).

[139] J. Yang, W. Hu, D. Usvyat, D. Matthews, M. Schütz, and G. K.-L. Chan, "Ab initio determination of the crystalline benzene lattice energy to sub-kilojoule/mole accuracy", Science **345**, 640–643 (2014).

[140] A. Kubas, D. Berger, H. Oberhofer, D. Maganas, K. Reuter, and F. Neese, "Surface Adsorption Energetics Studied with "Gold Standard" Wave-Function-Based Ab Initio Methods: Small-Molecule Binding to TiO_2 (110)", J. Phys. Chem. Lett. **7**, 4207–4212 (2016).

[141] J. McClain, Q. Sun, G. K.-L. Chan, and T. C. Berkelbach, "Gaussian-Based Coupled-Cluster Theory for the Ground-State and Band Structure of Solids", J. Chem. Theory Comput. **13**, 1209–1218 (2017).

[142] T. Gruber, K. Liao, T. Tsatsoulis, F. Hummel, and A. Grüneis, "Applying the Coupled-Cluster Ansatz to Solids and Surfaces in the Thermodynamic Limit", Phys. Rev. X **8**, 021043 (2018).

[143] I. Y. Zhang and A. Grüneis, "Coupled Cluster Theory in Materials Science", Front. Mater. **6**, 123 (2019).

[144] J. Sauer, "Ab Initio Calculations for Molecule–Surface Interactions with Chemical Accuracy", Acc. Chem. Res. **52**, 3502–3510 (2019).

[145] R. Dovesi, F. Pascale, B. Civalleri, K. Doll, N. M. Harrison, I. Bush, P. D'Arco, Y. Noël, M. Rérat, P. Carbonnière, M. Causà, S. Salustro, V. Lacivita, B. Kirtman, A. M. Ferrari, F. S. Gentile, J. Baima, M. Ferrero, R. Demichelis, and M. De La Pierre, "The CRYSTAL code, 1976–2020 and beyond, a long story", The Journal of Chemical Physics **152**, 204111 (2020).

[146] B. X. Shi, A. Zen, V. Kapil, P. R. Nagy, A. Grüneis, and A. Michaelides, "Many-Body Methods for Surface Chemistry Come of Age: Achieving Consensus with Experiments", J. Am. Chem. Soc. **145**, 25372–25381 (2023).

[147] K. Raghavachari, G. W. Trucks, J. A. Pople, and M. Head-Gordon, "A fifth-order perturbation comparison of electron correlation theories", Chemical Physics Letters **157**, 479–483 (1989).

[148] T. D. Crawford and H. F. Schaefer, "An Introduction to Coupled Cluster Theory for Computational Chemists", in *Reviews in Computational Chemistry*, Vol. 14, edited by K. B. Lipkowitz and D. B. Boyd, 1st ed. (Wiley, 2000), pp. 33–136.

[149] M. Motta, S. Zhang, and G. K.-L. Chan, "Hamiltonian symmetries in auxiliary-field quantum Monte Carlo calculations for electronic structure", Physical Review B **100**, 045127 (2019).

[150] K. B. Lipkowitz and T. R. Cundari, eds., *Reviews in Computational Chemistry*, 1st ed., Vol. 23, Reviews in Computational Chemistry (Wiley, 2007).

[151] S. Li, J. Shen, W. Li, and Y. Jiang, "An efficient implementation of the "cluster-in-molecule" approach for local electron correlation calculations", The Journal of Chemical Physics **125**, 074109 (2006).

[152] Y. Wang, Z. Ni, F. Neese, W. Li, Y. Guo, and S. Li, "Cluster-in-Molecule Method Combined with the Domain-Based Local Pair Natural Orbital Approach for Electron Correlation Calculations of Periodic Systems", J. Chem. Theory Comput. **18**, 6510–6521 (2022).

[153] Z.-H. Cui, C. Sun, U. Ray, B.-X. Zheng, Q. Sun, and G. K.-L. Chan, "Ground-state phase diagram of the three-band Hubbard model from density matrix embedding theory", Phys. Rev. Research **2**, 043259 (2020).

[154] E. Baerends, D. Ellis, and P. Ros, "Self-consistent molecular Hartree—Fock—Slater calculations I. The computational procedure", Chemical Physics **2**, 41–51 (1973).

[155] J. L. Whitten, "Coulombic potential energy integrals and approximations", The Journal of Chemical Physics **58**, 4496–4501 (1973).

[156] J. A. Jafri and J. L. Whitten, "Electron repulsion integral approximations and error bounds: Molecular applications", The Journal of Chemical Physics **61**, 2116–2121 (1974).

[157] N. H. F. Beebe and J. Linderberg, "Simplifications in the generation and transformation of two-electron integrals in molecular calculations", Int J of Quantum Chemistry **12**, 683–705 (1977).

[158] I. Røeggen and E. Wisløff-Nilssen, "On the Beebe-Linderberg two-electron integral approximation", Chemical Physics Letters **132**, 154–160 (1986).

[159] X. Ren, P. Rinke, V. Blum, J. Wieferink, A. Tkatchenko, A. Sanfilippo, K. Reuter, and M. Scheffler, "Resolution-of-identity approach to Hartree–Fock, hybrid density functionals, RPA, MP2 and GW with numeric atom-centered orbital basis functions", New J. Phys. **14**, 053020 (2012).

[160] R. A. Friesner, "Solution of self-consistent field electronic structure equations by a pseudospectral method", Chemical Physics Letters **116**, 39–43 (1985).

[161] F. Neese, F. Wennmohs, A. Hansen, and U. Becker, "Efficient, approximate and parallel Hartree–Fock and hybrid DFT calculations. A 'chain-of-Spheres' algorithm for the Hartree–Fock exchange", Chemical Physics **356**, 98–109 (2009).

[162] R. Izsák and F. Neese, "An overlap fitted chain of spheres exchange method", The Journal of Chemical Physics **135**, 144105 (2011).

[163] E. G. Hohenstein, R. M. Parrish, and T. J. Martínez, "Tensor hypercontraction density fitting. I. Quartic scaling second- and third-order Møller-Plesset perturbation theory", The Journal of Chemical Physics **137**, 044103 (2012).

[164] R. M. Parrish, E. G. Hohenstein, T. J. Martínez, and C. D. Sherrill, "Tensor hypercontraction. II. Least-squares renormalization", The Journal of Chemical Physics **137**, 224106 (2012).

[165] C. Song and T. J. Martínez, "Atomic orbital-based SOS-MP2 with tensor hypercontraction. I. GPU-based tensor construction and exploiting sparsity", The Journal of Chemical Physics **144**, 174111 (2016).

[166] D. A. Matthews, "A critical analysis of least-squares tensor hypercontraction applied to MP3", The Journal of Chemical Physics **154**, 134102 (2021).

[167] W. Hu, L. Lin, and C. Yang, "Interpolative Separable Density Fitting Decomposition for Accelerating Hybrid Density Functional Calculations with Applications to Defects in Silicon", J. Chem. Theory Comput. **13**, 5420–5431 (2017).

[168] K. Dong, W. Hu, and L. Lin, "Interpolative Separable Density Fitting through Centroidal Voronoi Tessellation with Applications to Hybrid Functional Electronic Structure Calculations", J. Chem. Theory Comput. **14**, 1311–1320 (2018).

[169] X. Qin, J. Liu, W. Hu, and J. Yang, "Interpolative Separable Density Fitting Decomposition for Accelerating Hartree–Fock Exchange Calculations within Numerical Atomic Orbitals", J. Phys. Chem. A **124**, 5664–5674 (2020).

[170] X. Qin, J. Li, W. Hu, and J. Yang, "Machine Learning K-Means Clustering Algorithm for Interpolative Separable Density Fitting to Accelerate Hybrid Functional Calculations with Numerical Atomic Orbitals", J. Phys. Chem. A **124**, 10066–10074 (2020).

[171] S. Sharma, A. F. White, and G. Beylkin, "Fast Exchange with Gaussian Basis Set Using Robust Pseudospectral Method", J. Chem. Theory Comput. **18**, 7306–7320 (2022).

[172] K. E. Smyser, A. White, and S. Sharma, "Use of Multigrids to Reduce the Cost of Performing Interpolative Separable Density Fitting", J. Phys. Chem. A **128**, 7451–7461 (2024).

[173] Z. Zhang, X. Yin, W. Hu, and J. Yang, "Machine Learning K-Means Clustering of Interpolative Separable Density Fitting Algorithm for Accurate and Efficient Cubic-Scaling Exact Exchange Plus Random Phase Approximation within Plane Waves", J. Chem. Theory Comput. **20**, 1944–1961 (2024).

[174] J. Lu and K. Thicke, "Cubic scaling algorithms for RPA correlation using interpolative separable density fitting", Journal of Computational Physics **351**, 187–202 (2017).

[175] I. Duchemin and X. Blase, "Separable resolution-of-the-identity with all-electron Gaussian bases: Application to cubic-scaling RPA", The Journal of Chemical Physics **150**, 174120 (2019).

[176] W. Gao and J. R. Chelikowsky, "Accelerating Time-Dependent Density Functional Theory and GW Calculations for Molecules and Nanoclusters with Symmetry Adapted Interpolative Separable Density Fitting", J. Chem. Theory Comput. **16**, 2216–2223 (2020).

[177] H. Ma, L. Wang, L. Wan, J. Li, X. Qin, J. Liu, W. Hu, L. Lin, C. Yang, and J. Yang, "Realizing Effective Cubic-Scaling Coulomb Hole Plus Screened Exchange Approximation in Periodic Systems via Interpolative Separable Density Fitting with a Plane-Wave Basis Set", J. Phys. Chem. A **125**, 7545–7557 (2021).

[178] I. Duchemin and X. Blase, "Cubic-Scaling All-Electron *GW* Calculations with a Separable Density-Fitting Space–Time Approach", J. Chem. Theory Comput. **17**, 2383–2393 (2021).

[179] F. D. Malone, S. Zhang, and M. A. Morales, "Overcoming the Memory Bottleneck in Auxiliary Field Quantum Monte Carlo Simulations with Interpolative Separable Density Fitting", J. Chem. Theory Comput. **15**, 256–264 (2019).

[180] C.-N. Yeh and M. A. Morales, "Low-Scaling Algorithm for the Random Phase Approximation Using Tensor Hypercontraction with k-Point Sampling", J. Chem. Theory Comput. **19**, 6197–6207 (2023).

[181] C.-N. Yeh and M. A. Morales, "Low-Scaling Algorithms for GW and Constrained Random Phase Approximation Using Symmetry-Adapted Interpolative Separable Density Fitting", J. Chem. Theory Comput. **20**, 3184–3198 (2024).

[182] K. Wu, X. Qin, W. Hu, and J. Yang, "Low-Rank Approximations Accelerated Plane-Wave Hybrid Functional Calculations with k-Point Sampling", J. Chem. Theory Comput. **18**, 206–218 (2022).

[183] X. Qin, W. Hu, and J. Yang, "Interpolative Separable Density Fitting for Accelerating Two-Electron Integrals: A Theoretical Perspective", J. Chem. Theory Comput. **19**, 679–693 (2023).

[184] A. Rettig, J. Lee, and M. Head-Gordon, "Even Faster Exact Exchange for Solids via Tensor Hypercontraction", J. Chem. Theory Comput. **19**, 5773–5784 (2023).

[185] Q. Sun, T. C. Berkelbach, J. D. McClain, and G. K.-L. Chan, "Gaussian and plane-wave mixed density fitting for periodic systems", The Journal of Chemical Physics **147**, 164119 (2017).

[186] Q. Sun, T. C. Berkelbach, N. S. Blunt, G. H. Booth, S. Guo, Z. Li, J. Liu, J. D. McClain, E. R. Sayfutyarova, S. Sharma, S. Wouters, and G. K.-L. Chan, "P Y SCF: The Python-based simulations of chemistry framework", WIREs Comput Mol Sci **8**, e1340 (2018).

[187] Q. Sun, X. Zhang, S. Banerjee, P. Bao, M. Barbry, N. S. Blunt, N. A. Bogdanov, G. H. Booth, J. Chen, Z.-H. Cui, J. J. Eriksen, Y. Gao, S. Guo, J. Hermann, M. R. Hermes, K. Koh, P. Koval, S. Lehtola, Z. Li, J. Liu, N. Mardirossian, J. D. McClain, M. Motta, B. Mussard, H. Q. Pham, A. Pulkin, W. Purwanto, P. J. Robinson, E. Ronca, E. R. Sayfutyarova, M. Scheurer, H. F. Schurkus, J. E. T. Smith, C. Sun, S.-N. Sun, S. Upadhyay, L. K. Wagner, X. Wang, A. White, J. D. Whitfield, M. J. Williamson, S. Wouters, J. Yang, J. M. Yu, T. Zhu, T. C. Berkelbach, S. Sharma, A. Y. Sokolov, and G. K.-L. Chan, "Recent developments in the P Y SCF program package", The Journal of Chemical Physics **153**, 024109 (2020).

[188] D. A. Matthews, "Improved Grid Optimization and Fitting in Least Squares Tensor Hypercontraction", J. Chem. Theory Comput. **16**, 1382–1385 (2020).

[189] J. Lee, L. Lin, and M. Head-Gordon, "Systematically Improvable Tensor Hypercontraction: Interpolative Separable Density-Fitting for Molecules Applied to Exact Exchange, Second- and Third-Order Møller–Plesset Perturbation Theory", J. Chem. Theory Comput. **16**, 243–263 (2020).

[190] F. Aryasetiawan, M. Imada, A. Georges, G. Kotliar, S. Biermann, and A. I. Lichtenstein, "Frequency-dependent local interactions and low-energy effective models from electronic structure calculations", Phys. Rev. B **70**, 195104 (2004).

[191] Y. Chang, E. G. C. P. Van Loon, B. Eskridge, B. Busemeyer, M. A. Morales, C. E. Dreyer, A. J. Millis, S. Zhang, T. O. Wehling, L. K. Wagner, and M. Rösner, "Downfolding from ab initio to interacting model Hamiltonians: Comprehensive analysis and benchmarking of the DFT+cRPA approach", npj Comput Mater **10**, 129 (2024).

[192] C. J. C. Scott and G. H. Booth, "Rigorous Screened Interactions for Realistic Correlated Electron Systems", Phys. Rev. Lett. **132**, 076401 (2024).

[193] R. Song, X. Gong, A. Bakry, and H.-Z. Ye, *Random phase approximation-based local natural orbital coupled cluster theory*, arXiv, Dec. 2025.

[194] A. Dixit, J. G. Ángyán, and D. Rocca, "Improving the accuracy of ground-state correlation energies within a plane-wave basis set: The electron-hole exchange kernel", The Journal of Chemical Physics **145**, 104105 (2016).

[195] I. Haritan, X. Wang, and T. Goldzak, "An Efficient Scaled Opposite-Spin MP2 Method for Periodic Systems", J. Chem. Theory Comput. **21**, 6823–6833 (2025).

[196] S. Goedecker, M. Teter, and J. Hutter, "Separable dual-space Gaussian pseudopotentials", Phys. Rev. B **54**, 1703–1710 (1996).

[197] C. Hartwigsen, S. Goedecker, and J. Hutter, "Relativistic separable dual-space Gaussian pseudopotentials from H to Rn", Phys. Rev. B **58**, 3641–3662 (1998).

[198] J. Hutter, *GTH: GTH pseudopotentials for PBE, SCAN, PBE0, and Hartree-Fock*, GitHub, 2024.

[199] R. Sundararaman and T. A. Arias, "Regularization of the Coulomb singularity in exact exchange by Wigner-Seitz truncated interactions: Towards chemical accuracy in nontrivial systems", Phys. Rev. B **87**, 165122 (2013).

[200] M. Nusspickel, B. Ibrahim, and G. H. Booth, "Effective Reconstruction of Expectation Values from Ab Initio Quantum Embedding", J. Chem. Theory Comput. **19**, 2769–2791 (2023).

[201] T. Goldzak, X. Wang, H.-Z. Ye, and T. C. Berkelbach, "Accurate thermochemistry of covalent and ionic solids from spin-component-scaled MP2", The Journal of Chemical Physics **157**, 174112 (2022).

[202] L. MacEnulty and D. D. O'Regan, "Optimization strategies developed on NiO for Heisenberg exchange coupling calculations using projector augmented wave based first-principles DFT+U+J", Phys. Rev. B **108**, 245137 (2023).

[203] T. N. Casselman and F. Keffer, "Right-Angled Superexchange", Phys. Rev. Lett. **4**, 498–500 (1960).

[204] I. De P. R. Moreira, F. Illas, and R. L. Martin, "Effect of Fock exchange on the electronic structure and magnetic coupling in NiO", Phys. Rev. B **65**, 155102 (2002).

[205] D. Kan, A. Yamanaka, T. Terashima, and M. Takano, "Preparation and optical properties of single-crystalline CaCuO2 thin films with infinite layer structure", Physica C: Superconductivity **412–414**, 298–302 (2004).

[206] Y. Y. Peng, G. Dellea, M. Minola, M. Conni, A. Amorese, D. Di Castro, G. M. De Luca, K. Kummer, M. Salluzzo, X. Sun, X. J. Zhou, G. Balestrino, M. Le Tacon, B. Keimer, L. Braicovich, N. B. Brookes, and G. Ghiringhelli, "Influence of apical oxygen on the extent of in-plane exchange interaction in cuprate superconductors", Nature Phys **13**, 1201–1206 (2017).

[207] G. Wellein and H. Fehske, "Self-trapping problem of electrons or excitons in one dimension", Phys. Rev. B **58**, 6208–6218 (1998).

[208] N. N. Bogoljubov, V. V. Tolmachov, and D. V. Širkov, "A New Method in the Theory of Superconductivity", Fortschr. Phys. **6**, 605–682 (1958).

[209] J.-P. Blaizot and G. Ripka, *Quantum theory of finite systems* (MIT Press, Cambridge, Mass, 1986).

[210] P. Nagels, M. Denayer, and J. Devreese, "Electrical properties of single crystals of uranium dioxide", Solid State Communications **1**, 35–40 (1963).

[211] C. Crevecoeur and H. De Wit, "Electrical conductivity of Li doped MnO", Journal of Physics and Chemistry of Solids **31**, 783–791 (1970).

[212] G. D. Mahan, *Many-Particle Physics* (Springer US, Boston, MA, 2000).

[213] D. Emin, "Small polarons", Phys. Today **35**, 34–40 (1982).

[214] C. Franchini, M. Reticcioli, M. Setvin, and U. Diebold, "Polarons in materials", Nat Rev Mater **6**, 560–586 (2021).

[215] L. R. V. Buizza and L. M. Herz, "Polarons and Charge Localization in Metal-Halide Semiconductors for Photovoltaic and Light-Emitting Devices", Advanced Materials **33**, 2007057 (2021).

[216] V. Coropceanu, J. Cornil, D. A. Da Silva Filho, Y. Olivier, R. Silbey, and J.-L. Brédas, "Charge Transport in Organic Semiconductors", Chem. Rev. **107**, 926–952 (2007).

[217] M. Mladenović and N. Vukmirović, "Charge Carrier Localization and Transport in Organic Semiconductors: Insights from Atomistic Multiscale Simulations", Adv Funct Materials **25**, 1915–1932 (2015).

[218] M. Schröter, S. Ivanov, J. Schulze, S. Polyutov, Y. Yan, T. Pullerits, and O. Kühn, "Exciton–vibrational coupling in the dynamics and spectroscopy of Frenkel excitons in molecular aggregates", Physics Reports **567**, 1–78 (2015).

[219] V. May and O. Kühn, *Charge and Energy Transfer Dynamics in Molecular Systems*, 1st ed. (Wiley, Feb. 2011).

[220] S. J. Jang and B. Mennucci, "Delocalized excitons in natural light-harvesting complexes", Rev. Mod. Phys. **90**, 035003 (2018).

[221] L. Landau, "Electron Motion in Crystal Lattices", Phys. Z. Sowjet. **3**, 664 (1933).

[222] C. H. Chen, S.-W. Cheong, and A. S. Cooper, "Charge modulations in $La_{2-x}Sr_xNiO_{4+y}$: ordering of polarons", Phys. Rev. Lett. **71**, 2461–2464 (1993).

[223] A. J. Millis, P. B. Littlewood, and B. I. Shraiman, "Double exchange alone does not explain the resistivity of $La_{1-x}Sr_xMn\ O_3$", Phys. Rev. Lett. **74**, 5144–5147 (1995).

[224] J. P. Falck, A. Levy, M. A. Kastner, and R. J. Birgeneau, "Optical excitation of polaronic impurities in La_2CuO_{4+y}", Phys. Rev. B **48**, 4043–4046 (1993).

[225] M. Grilli and C. Castellani, "Electron-phonon interactions in the presence of strong correlations", Phys. Rev. B **50**, 16880–16898 (1994).

[226] Y. H. Kim, C. M. Foster, A. J. Heeger, S. Cox, and G. Stucky, "Photoinduced self-localized structural distortions in $YBa_2Cu_3O_{7-\delta}$", Phys. Rev. B **38**, 6478–6482 (1988).

[227] V. Z. Kresin and S. A. Wolf, "Electron-lattice interaction and its impact on high-T_c superconductivity", Rev. Mod. Phys. **81**, 481–501 (2009).

[228] T. Holstein, "Studies of polaron motion", Annals of Physics **8**, 325–342 (1959).

[229] B. Gerlach and H. Löwen, "Analytical properties of polaron systems or: Do polaronic phase transitions exist or not?", Rev. Mod. Phys. **63**, 63–90 (1991).

[230] I. G. Lang and Y. A. Firsov, "Kinetic Theory of Semiconductors with Low Mobility", Sov. J. Exp. Theor. Phys. **16**, 1301 (1963).

[231] C. Zhang, E. Jeckelmann, and S. R. White, "Density Matrix Approach to Local Hilbert Space Reduction", Phys. Rev. Lett. **80**, 2661–2664 (1998).

[232] E. Dagotto, "Correlated electrons in high-temperature superconductors", Rev. Mod. Phys. **66**, 763–840 (1994).

[233] E. Jeckelmann and S. R. White, "Density-matrix renormalization-group study of the polaron problem in the Holstein model", Phys. Rev. B **57**, 6376–6385 (1998).

[234] H. De Raedt and A. Lagendijk, "Numerical calculation of path integrals: The small-polaron model", Phys. Rev. B **27**, 6097–6109 (1983).

[235] J. E. Hirsch, R. L. Sugar, D. J. Scalapino, and R. Blankenbecler, "Monte Carlo simulations of one-dimensional fermion systems", Phys. Rev. B **26**, 5033–5055 (1982).

[236] J. E. Hirsch and E. Fradkin, "Phase diagram of one-dimensional electron-phonon systems. II. The molecular-crystal model", Phys. Rev. B **27**, 4302–4316 (1983).

[237] S. R. White, D. J. Scalapino, R. L. Sugar, E. Y. Loh, J. E. Gubernatis, and R. T. Scalettar, "Numerical study of the two-dimensional Hubbard model", Phys. Rev. B **40**, 506–516 (1989).

[238] P. E. Kornilovitch and E. R. Pike, "Polaron effective mass from Monte Carlo simulations", Phys. Rev. B **55**, R8634–R8637 (1997).

[239] R. M. Noack and D. J. Scalapino, "Green's-function self-energies in the two-dimensional Holstein model", Phys. Rev. B **47**, 305–308 (1993).

[240] A. La Magna and R. Pucci, "Variational study of the discrete Holstein model", Phys. Rev. B **53**, 8449–8456 (1996).

[241] D. W. Brown, K. Lindenberg, and Y. Zhao, "Variational energy band theory for polarons: Mapping polaron structure with the global-local method", J. Chem. Phys. **107**, 3179–3195 (1997).

[242] A. H. Romero, D. W. Brown, and K. Lindenberg, "Self-trapping line of the Holstein molecular crystal model in one dimension", Phys. Rev. B **60**, 4618–4623 (1999).

[243] A. H. Romero, D. W. Brown, and K. Lindenberg, "Polaron effective mass, band distortion, and self-trapping in the Holstein molecular-crystal model", Phys. Rev. B **59**, 13728–13740 (1999).

[244] Y. Wang, I. Esterlis, T. Shi, J. I. Cirac, and E. Demler, "Zero-temperature phases of the two-dimensional Hubbard-Holstein model: A non-Gaussian exact diagonalization study", Phys. Rev. Research **2**, 043258 (2020).

[245] S. Ciuchi, F. De Pasquale, S. Fratini, and D. Feinberg, "Dynamical mean-field theory of the small polaron", Phys. Rev. B **56**, 4494–4512 (1997).

[246] A. J. Millis, B. I. Shraiman, and R. Mueller, "Dynamic jahn-teller effect and colossal magnetoresistance in $La_{1-x}Sr_xMn\ O_3$", Phys. Rev. Lett. **77**, 175–178 (1996).

[247] B. Sandhoefer and G. K.-L. Chan, "Density matrix embedding theory for interacting electron-phonon systems", Phys. Rev. B **94**, 085115 (2016).

[248] T. E. Reinhard, U. Mordovina, C. Hubig, J. S. Kretchmer, U. Schollwöck, H. Appel, M. A. Sentef, and A. Rubio, "Density-Matrix Embedding Theory Study of the One-Dimensional Hubbard–Holstein Model", J. Chem. Theory Comput. **15**, 2221–2232 (2019).

[249] A. A. Gogolin, "The Spectrum of an Intermediate Polaron and Its Bound States with Phonons at Strong Coupling", phys. stat. sol. (b) **109**, 95–108 (1982).

[250] F. Marsiglio, "Pairing in the Holstein model in the dilute limit", Physica C: Superconductivity **244**, 21–34 (1995).

[251] W. Stephan, "Single-polaron band structure of the Holstein model", Phys. Rev. B **54**, 8981–8984 (1996).

[252] W. H. Sio, C. Verdi, S. Poncé, and F. Giustino, "Polarons from First Principles, without Supercells", Phys. Rev. Lett. **122**, 246403 (2019).

[253] N.-E. Lee, H.-Y. Chen, J.-J. Zhou, and M. Bernardi, "Facile *ab initio* approach for self-localized polarons from canonical transformations", Phys. Rev. Materials **5**, 063805 (2021).

[254] Y. Luo, B. K. Chang, and M. Bernardi, "Comparison of the canonical transformation and energy functional formalisms for *ab initio* calculations of self-localized polarons", Phys. Rev. B **105**, 155132 (2022).

[255] F. Coester, "Bound states of a many-particle system", Nucl. Phys. **7**, 421–424 (1958).

[256] J. Čížek, "On the correlation problem in atomic and molecular systems. Calculation of wavefunction components in Ursell-Type expansion using Quantum-Field theoretical methods", J. Chem. Phys. **45**, 4256–4266 (1966).

[257] J. Paldus and J. Čížek, "Time-independent diagrammatic aproach to perturbation theory of fermion systems.", Adv. Quantum Chem. **9**, 105–195 (1975).

[258] J. Čížek and J. Paldus, "Coupled cluster approach", Phys. Scr. **21**, 251 (1980).

[259] R. J. Bartlett and M. Musiał, "Coupled-cluster theory in quantum chemistry", Rev. Mod. Phys. **79**, 291–352 (2007).

[260] I. Shavitt and R. J. Bartlett, *Many-body methods in chemistry and physics: MBPT and coupled-cluster theory* (Cambridge University Press, New York, 2009).

[261] Y. Gao, Q. Sun, J. M. Yu, M. Motta, J. McClain, A. F. White, A. J. Minnich, and G. K. L. Chan, "Electronic structure of bulk manganese oxide and nickel oxide from coupled cluster theory", Phys. Rev. B **101**, 1–9 (2020).

[262] Z.-H. Cui, A. Mandal, and D. R. Reichman, "Variational Lang–Firsov Approach Plus Møller–Plesset Perturbation Theory with Applications to Ab Initio Polariton Chemistry", J. Chem. Theory Comput. **20**, 1143–1156 (2024).

[263] H. Zhai and G. K.-L. Chan, "Low communication high performance *ab initio* density matrix renormalization group algorithms", J. Chem. Phys. **154**, 224116 (2021).

[264] H. Zhai, H. R. Larsson, S. Lee, Z.-H. Cui, T. Zhu, C. Sun, L. Peng, R. Peng, K. Liao, J. Tölle, J. Yang, S. Li, and G. K.-L. Chan, "Block2: A comprehensive open source framework to develop and apply state-of-the-art DMRG algorithms in electronic structure and beyond", The Journal of Chemical Physics **159**, 234801 (2023).

[265] S. Hirata, I. Grabowski, M. Tobita, and R. J. Bartlett, "Highly accurate treatment of electron correlation in polymers: Coupled-cluster and many-body perturbation theories", Chem. Phys. Lett. **345**, 475–480 (2001).

[266] S. Hirata, R. Podeszwa, M. Tobita, and R. J. Bartlett, "Coupled-cluster singles and doubles for extended systems", J. Chem. Phys. **120**, 2581–2592 (2004).

[267] A. Grüneis, G. H. Booth, M. Marsman, J. Spencer, A. Alavi, and G. Kresse, "Natural orbitals for wave function based correlated calculations using a plane wave basis set", J. Chem. Theory Comput. **7**, 2780–2785 (2011).

[268] J. McClain, Q. Sun, G. K. L. Chan, and T. C. Berkelbach, "Gaussian-based coupled-cluster theory for the ground-state and band structure of solids", J. Chem. Theory Comput. **13**, 1209–1218 (2017).

[269] M. Motta, D. M. Ceperley, G. K. L. Chan, J. A. Gomez, E. Gull, S. Guo, C. A. Jiménez-Hoyos, T. N. Lan, J. Li, F. Ma, A. J. Millis, N. V. Prokof'ev, U. Ray, G. E. Scuseria, S. Sorella, E. M. Stoudenmire, Q. Sun, I. S. Tupitsyn, S. R. White, D. Zgid, and S. Zhang, "Towards the solution of the many-electron problem in real materials: Equation of state of the hydrogen chain with state-of-the-art many-body methods", Phys. Rev. X **7**, 1–28 (2017).

[270] T. Gruber, K. Liao, T. Tsatsoulis, F. Hummel, and A. Grüneis, "Applying the coupled-cluster ansatz to solids and surfaces in the thermodynamic limit", Phys. Rev. X **8**, 21043 (2018).

[271] M. D. Prasad, "Time-dependent coupled cluster method: A new approach to the calculation of molecular absorption spectra", J. Chem. Phys. **88**, 7005–7010 (1988).

[272] V. Nagalakshmi, V. Lakshminarayana, G. Sumithra, and M. Durga Prasad, "Coupled cluster description of anharmonic molecular vibrations. Application to O3 and SO2", Chem. Phys. Lett. **217**, 279–282 (1994).

[273] G. Madhavi Sastry and M. Durga Prasad, "The time-dependent coupled cluster approach to molecular photodissociation dynamics", Chem. Phys. Lett. **228**, 213–218 (1994).

[274] G. S. Latha and M. D. Prasad, "Time-dependent coupled cluster approach to multimode vibronic dynamics", J. Chem. Phys. **105**, 2972–2977 (1996).

[275] M. Durga Prasad, "Time dependent coupled cluster approach to Resonance Raman excitationprofiles from general anharmonic surfaces", Int. J. Mol. Sci. **3**, 447–458 (2002).

[276] S. Banik, S. Pal, and M. D. Prasad, "Calculation of vibrational energy of molecule using coupled cluster linear response theory in bosonic representation: Convergence studies", J. Chem. Phys. **129**, 10.1063/1.2982502 (2008).

[277] S. Banik, S. Pal, and M. D. Prasad, "Calculation of dipole transition matrix elements and expectation values by vibrational coupled cluster method", J. Chem. Theory Comput. **6**, 3198–3204 (2010).

[278] O. Christiansen, "A second quantization formulation of multimode dynamics", J. Chem. Phys. **120**, 2140–2148 (2004).

[279] P. Seidler and O. Christiansen, "Vibrational excitation energies from vibrational coupled cluster response theory", J. Chem. Phys. **126**, 10.1063/1.2734970 (2007).

[280] P. Seidler and O. Christiansen, "Automatic derivation and evaluation of vibrational coupled cluster theory equations", J. Chem. Phys. **131**, 10.1063/1.3272796 (2009).

[281] A. F. White, Y. Gao, A. J. Minnich, and G. K.-L. Chan, "A coupled cluster framework for electrons and phonons", J. Chem. Phys. **153**, 224112 (2020).

[282] A. S. Alexandrov, V. V. Kabanov, and D. K. Ray, "From electron to small polaron: An exact cluster solution", Phys. Rev. B **49**, 9915–9923 (1994).

[283] U. Mordovina, C. Bungey, H. Appel, P. J. Knowles, A. Rubio, and F. R. Manby, "Polaritonic coupled-cluster theory", Phys. Rev. Res. **2**, 1–8 (2020).

[284] T. S. Haugland, E. Ronca, E. F. Kjønstad, A. Rubio, and H. Koch, "Coupled Cluster Theory for Molecular Polaritons: Changing Ground and Excited States", Phys. Rev. X **10**, 041043 (2020).

[285] X. Li and Y. Zhang, *First-principles molecular quantum electrodynamics theory at all coupling strengths*, Nov. 2023.

[286] C. Yang, J. Brabec, L. Veis, D. B. Williams-Young, and K. Kowalski, "Solving Coupled Cluster Equations by the Newton Krylov Method", Front. Chem. **8**, 590184 (2020).

[287] D. Knoll and D. Keyes, "Jacobian-free Newton–Krylov methods: a survey of approaches and applications", Journal of Computational Physics **193**, 357–397 (2004).

[288] S. R. White, "Density-matrix algorithms for quantum renormalization groups", Phys. Rev. B **48**, 10345–10356 (1993).

[289] C. Zhang, E. Jeckelmann, and S. R. White, "Dynamical properties of the one-dimensional Holstein model", Phys. Rev. B **60**, 14092–14104 (1999).